

Abstract 2

Chapter 1: Introduction - PTEN and phosphoinositides 5

1.1 Phosphoinositides in the plasma membrane; more than a “solvent” for proteins. 5

1.2 PIPs, PTEN, and Disease 13

1.3 The Structure of PTEN 17

Chapter 2: Ensemble Kinetics 22

2.1 Methodology 24

Recombinant PTEN Expression and Purification. 24

Stopped-Flow Techniques 27

KinTeK Global Fit Analysis 30

2.2 Ensemble Kinetics of PTEN binding to Lipid Membranes 32

Kinetic analysis of PTEN association using the total lipid concentration (Figure 13) 38

Kinetic analysis of PTEN association using only the concentration of the anionic lipid species (Figure 14) 40

Kinetic analysis of PTEN association using a charge normalized lipid concentration (Figure 15) 42

Kinetic analysis of PTEN association using the “target” lipid concentration (Figure 16) 43

Kinetic analysis of PTEN dissociation from mixed vesicles 47

Equilibrium analysis of PTEN binding to mixed lipid vesicles 50

2.3 Global Analysis. 55

2.4 Discussion of Ensemble Kinetics 59

Chapter 3: Single Molecule Study of PTEN lipid interaction 65

3.1 Methodology 66

Supported Lipid Bilayers. 66

Sfp phosphopantetheinyl transferase method. 67

Fiji and Mathematica Data Analysis 69

Dwell Time Filtering and Analysis 74

3.2 Diffusion of PTEN on SLB 75

3.3 Dwell Times 84

3.4 Discussion of Single-Molecule Results 92

4.1 Methodology 100

Constructing the Microfluidic Platform 100

Developing a Supported Lipid Bilayer in the Microfluidic Platform 101

Establishing a PI(4,5)P₂ Gradient 103

Direct Deposition Method 104

Imaging the Gradients 105

4.2 Insertion of aqueous PI(4,5)P₂ in SLB 106

4.3 Generation of a PI(4,5)P₂ gradient in a DOPC SLB. 107

4.4 Effects of a Gradient of Ligand on Homogenous Bilayer 113

4.5 Conclusions and Outlook with the microfluidic platform 124

5.0 Future Directions 127

5.1 Kinetics Experiments 127

5.2 Microfluidics 129

List of Figures 131

List of Tables 136

Appendix 137

Bibliography 154

Abstract

Phosphoinositides are critical second messengers, and often their aberrant metabolism and membrane localization plays a role in the development of diseases such as cancer. The dynamic metabolism and localization between phosphatidylinositol-(4,5)-bisphosphate (PI(4,5)P₂) and phosphatidylinositol-(3,4,5)-trisphosphate (PI(3,4,5)P₃) in the PI3K-AKT pathway, is in part, regulated by the protein known as phosphatase and tensin homolog deleted on chromosome ten (PTEN). PTEN is one of the most frequently mutated genes in cancer, and its location on the plasma membrane (PM) is often found to be polarized in cells. *Despite the importance of PTEN in health, the effects of the PM lipids on its localization and thus, its functional mechanism still need to be fully elucidated.* The obstacles to fully understanding how the *localization of lipids affects PTEN's membrane interactions* include (a) not all lipid species have probes to follow their location in cells, (b) lipids cannot be knocked-in and -out in cellular systems, which is especially true for phosphoinositides, (c) each lipid species that participates in the PTEN-membrane interactions cannot be independently titrated in the cell, which is essential for defining the mechanism of PTEN-membrane interactions. Using model systems, these obstacles can be overcome, thus developing a more nuanced biophysical understanding of the system. **We hypothesize that PTEN uses its multiple lipid binding domains to interact synergistically with a distinct ensemble of lipids in membranes, which efficiently localizes the protein near its substrate. PTEN localization in cellular systems depends on this spatiotemporal control of the phosphoinositides and their associated lipid partners.**

Project 1. Ensemble Kinetics: We determined the rate constants of PTEN binding to multicomponent model membranes, which allowed us to elucidate the roles of individual lipids in this interaction. Fluorescence stopped-flow spectrophotometry was used to determine the rates of the interaction, and the KinTeK global fit software was used to interpret it. We determined the roles of phosphatidylserine, phosphatidylinositol, and PI(4,5)P₂ in PTEN-membrane interactions and identified the interactions that drive PTEN to the membrane. Also, we determined whether domain formation observed for specific lipid compositions affected the rates of PTEN binding.

Project 2. Single Molecule Studies: We determined how PTEN domains interact with model membranes of various compositions. Single-molecule TIRF microscopy was used to determine diffusion constants and dwell times of these constructs that were then compared to the wild-type (wt) protein. The outcome was that PTEN domains work together to interact with the membrane, resulting in a synergistic binding with the surface.

Project 3. A novel model system to study phosphoinositide gradients: We developed a model system that generates gradients of phosphoinositides or the proteins that regulate them. Taking advantage of the lamellar flow of microfluidic platforms, we can generate a supported lipid bilayer with a lipid gradient or affect a homogenous lipid bilayer with a gradient of a dissolved chemical species above the lipid bilayer and follow the development of the bilayer system using TIRF microscopy. The outcome of this project was the development of a novel model system that can recapitulate PM polarization seen in cells, allowing investigation of the effects of lateral gradients in protein-membrane systems.

The proposed project will result in a nuanced biophysical understanding of the mechanism of PTEN interacting with complex lipid surfaces and provide greater insight on how peripheral proteins interact with the PM. This will provide the broader community with additional insight on how processes like cellular polarization and its dysregulation affect enzyme action and disease progression.

Chapter 1: Introduction - PTEN and phosphoinositides

1.1 Phosphoinositides in the plasma membrane; more than a “solvent” for proteins.

The Singer-Nicolson fluid mosaic model of biological membranes has an astonishing 6000 citations and has enjoyed over 45 years as the preeminent model for these cellular structures (Figure 1)¹. This model has lipids organized as a double layer where the nonpolar acyl tails form a greasy core, and the polar heads interact with the aqueous environments within and outside the cell. These lipids form a bilayer structure that proteins can associate with. Membrane-associated proteins fall into two broad groups, integral (transmembrane) and peripheral (surface-residing) proteins. Singer and Nicolson describe the membrane as fluid, where both the lipid and the proteins are mobile in the plane of the membrane, vertically asymmetric (the chemical components and composition differ from the cytosolic side to extracellular side) as well as crowded,

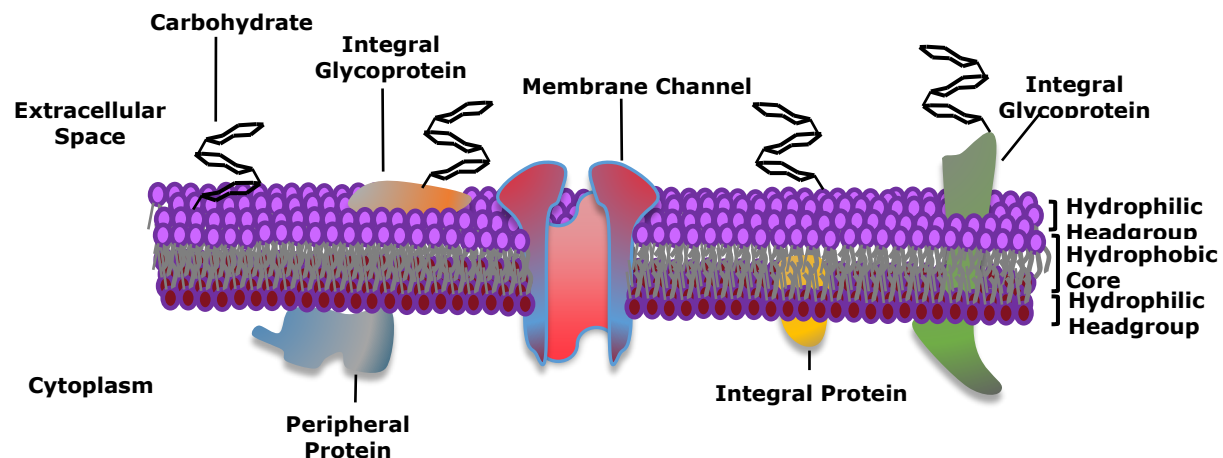


Figure 1. The classic fluid mosaic model of the plasma membrane developed by Singer and Nicolson. This bilayer has several key features making it a stable and dynamic cellular structure. First, is the amphipathic nature of the main chemical constituents, the lipids. These biomolecules organize proteins by solvating hydrophobic regions of transmembrane segments as well as providing a dense, diverse chemical surface for cytosolic proteins to organize and interact with. The lipid bilayer is fluid, crowded and asymmetric in respect to the chemistry between the extracellular and cytosolic compartments of the cell. Though this model is the mainstay of membranes, modern investigations have discovered an even

(proteins make up half the mass)^{1, 2}. This microscopic model of biomembranes has proven to be invaluable to the field of biochemistry over the decades. However, it has been shown time and again that the lipids are more than just a solvent for proteins, and evidence of this starts with the immense diversity of these molecular species.

The increasing sophistication and, consequently, resolution of instrumentation has uncovered a molecular diversity in the lipidome that rivals the proteome. Lipid MAPS, the internationally recognized, public, biologically relevant, lipid structural database, has reported 20,664 species as of 12/27/17, and a little over that amount again for computationally derived lipids³. From a different perspective, eukaryotic cells dedicate approximately 5% of their genome to lipid metabolism^{4, 5}. Following “structure supersedes function” hypothesis, the natural question is why do cellular systems sacrifice so much energy and chemical resources to maintain this enormous lipid diversity? There are three major classes of membrane lipids in eukaryotes. These are the sterols/ isoprenoids, sphingolipids, and glycerolphospholipids.

Figure 2 highlights the potential chemical functionality of the glycerolphospholipids^{5, 6}. Chemical modifications of these molecules can occur at two major sites, (1) the acyl chain tails vary in both the length and saturation of the hydrocarbon chain and (2) the headgroup. By altering the headgroup chemistry, the cell derives the abundant inner leaflet phospholipids; phosphatidylethanolamine (PE), phosphatidylcholine (PC), phosphatidylserine (PS), cardiolipin (CL) and phosphatidylinositol (PI). These lipid headgroups have chemical and physical properties that affect lipid-lipid and lipid-protein

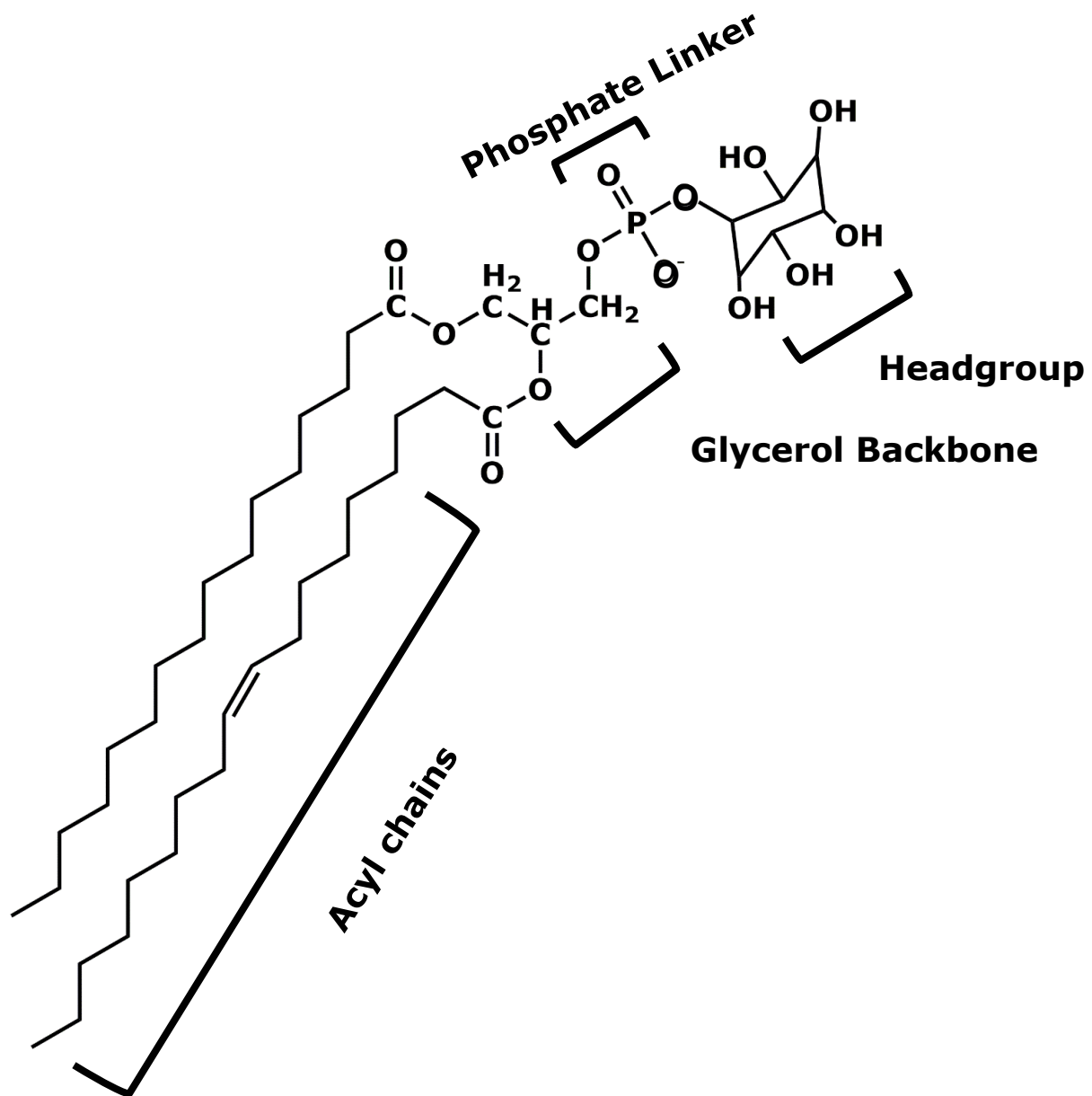


Figure 2. The chemical variability of phospholipids is due to the rich functionality of the molecule. The modification can occur at the head group and by varying the fatty acid chain length or saturation. The permutations of these chemical building blocks could generate tens of thousands of lipids species, naturally occurring eukaryotic membranes contain about 1000 unique lipids.

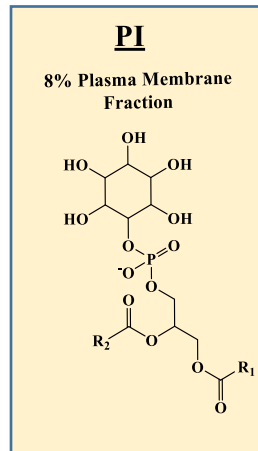
interactions. For example, anionic phospholipids like PS, PI (figure 2), PG and CL have a net negative charge (-1) at pH 7. PE and PS have reactive amines which can participate in hydrogen bonding, and PC, PI, and CL headgroups are bulky, affecting lipid packing⁶. PI is of particular interest to this study because it is the precursor to a specialized class of signaling glycerolphospholipids known as the phosphoinositides (PIPs).

The precursor to all PIPs is PI (Figure 2). Reversible phosphorylation can occur at the hydroxyls of the PI inositol headgroup at the third, fourth, and/or fifth inositol ring positions, yielding seven different naturally occurring PIP species. These are PI(3)P, PI(4)P, PI(5)P, PI(3,4)P₂, PI(4,5)P₂, PI(3,5)P₂, PI(3,4,5)P₃ (Figure 3)⁷. Depending on the membrane compartment, (endoplasmic reticulum, plasma membrane, *etc.*), there are a group of dedicated kinases and phosphatases that control the phosphorylation status of these lipids. These enzymes tightly control the type and concentration of the PIPs in the different membrane compartments, developing a “barcode” that differentiates one membrane from another⁴.

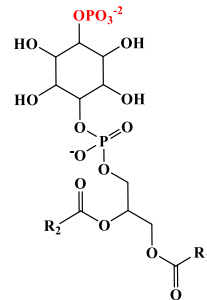
In contrast to the headgroup diversity, the PIPs acyl chains are predominately stearoyl at the first (sn-1) and arachidonoyl at the second (sn-2) position^{7, 8}. The arachidonoyl chain has four cis configured double bonds which disrupt tight lipid packing. As a result, these lipids localize in liquid disordered (fluid) regions of bilayers⁷. This preference for fluid membrane regions does not mean that PIPs cannot accumulate into enriched *fluid* domains. In this context, a lipid domain is a region in the membrane that exhibits a boundary with the surrounding membrane and is characterized by a distinct composition and physical properties. PIP clustering (formation of PIP-enriched domains), is driven by interactions within their headgroup region and influences interactions at the

Figure 3. There are seven members of the phosphoinositide family.

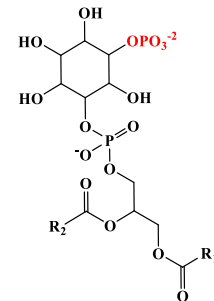
They are derived from the precursor phosphatidylinositol (PI) by a series of dedicated kinases and phosphatases. The PIP members are PI(3)P, PI(4)P, PI(5)P, PI(3,4)P₂, PI(4,5)P₂, PI(3,5)P₂, and PI(3,4,5)P₃. In the plasma membrane PI(4,5)P₂ and PI(4)P are the most common representing 2% and 1% of the lipid pool respectively. PI(3,4,5)P₃ is obtained by the phosphorylation of PI(4,5)P₂ by the kinase PI3K. PI(3,4,5)P₃ is a potent second messenger, yet is measured at less than 1% of the total phosphoinositide PM pool.



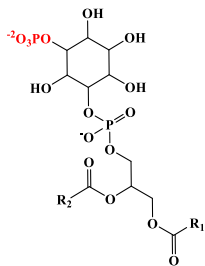
PI(4)P



PI(5)P

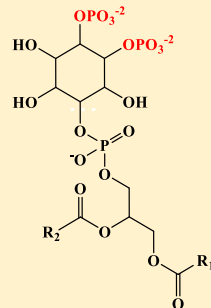


PI(3)P

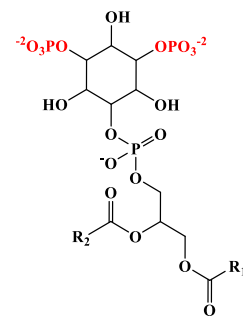


PI(4,5)P₂

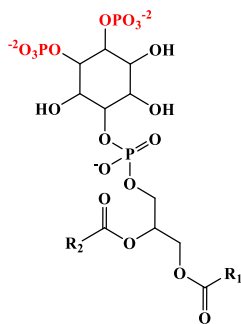
2% Plasma Membrane Fraction



PI(3,5)P₂

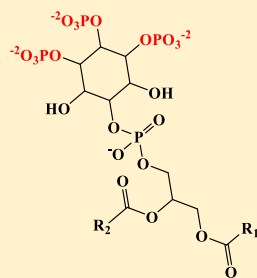


PI(3,4)P₂



PI(3,4,5)P₃

>1% PI(4,5)P₂



membrane interface by providing regions of a high electrostatic negative potential that attract peripheral proteins to the membrane⁷. For example, *in vitro*, clusters can be seen with mixed domains of PI and PI(4,5)P₂ in giant unilamellar PI/PI(4,5)P₂/PC vesicles⁹. PI and PI(4,5)P₂ cooperatively form mixed domains that potentially regulate the spatial organization of signaling events. Taking into account the PI cellular distribution and the rapid phosphorylation of PI to form PIPs, it is enticing to think that these mixtures may be enriched with peripheral proteins that have dual specificity for anionic lipids and PIPs⁷. This would form a signaling platform that is dynamic due to the fluidity of the lipid constituents but also solves the scarcity paradox of PIPs by enriching them in domains.

The scarcity paradox of PIPs recognizes that these lipids are extremely rare but incredibly potent for protein function. The percent composition of the precursor, PI, in the plasma membrane varies from 10-20%, depending on the cell type and tissue, but PIPs in total make up less than 1% of the total cellular lipid pool. PI(4,5)P₂ and PI(4)P are the most abundant PIPs, enriched in the PM and Golgi respectively (~0.2-1%)⁷. This means there is approximately 5000-20,000 PI(4,5)P₂/μm² in the plasma membrane's cytosolic leaflet⁷. The other PIPs exist at approximately 0.2-0.3% for PI(3)P, and 0.02-0.05% for PI(3,4,5)P₃, even at activated levels (Figure 4)^{7, 10}. The tight spatiotemporal control is not surprising considering the functions that the PIPs influence, such as membrane trafficking, cytoskeleton dynamics, endocytic/exocytic machinery and chemotaxis^{7, 11}. Interestingly, despite these low concentrations of PIPs, the number of proteins with domains specific for the individual PIP species is large in magnitude and vast in type. This dichotomy between low PIP levels, and high abundance of PIP-binding proteins is at the center of the "scarcity paradox." Table 1 lists just a few of the most well-known domains

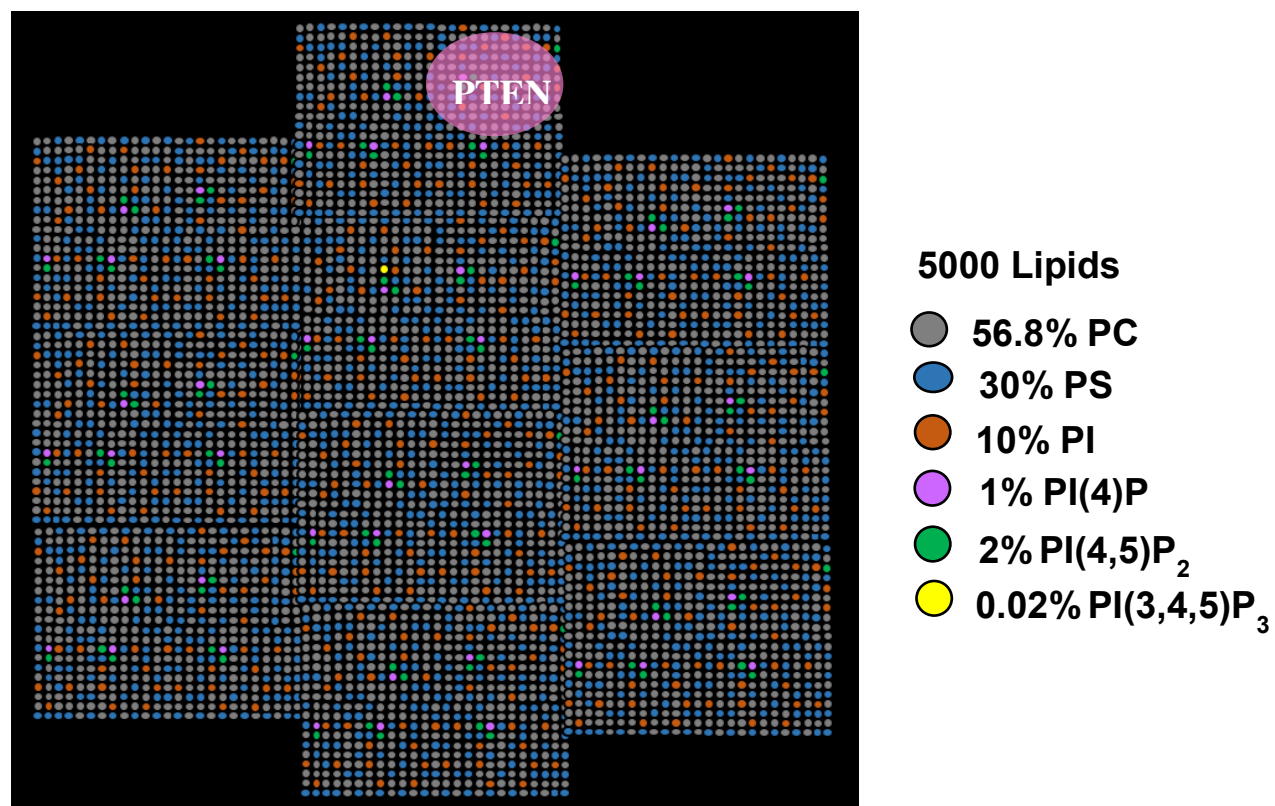


Figure 4. The rarity of the phosphoinositides belies their importance. The most abundant phosphoinositide is PI(4,5)P₂ at 2%, of the lipid pool, and PI(3,4,5)P₃ is about 1% of the PI(4,5)P₂ population. Yet, there are many types of proteins that interact specifically and nonspecifically with the phosphoinositides making them a high demand substrate. If the lipids are randomly distributed as in the figure above and the protein footprint covers 100 to 150 lipids it would need to sort through 5000 lipids to find one PI(3,4,5)P₃.

that have interactions with these lipids¹². This thesis is concerned with PI(4,5)P₂ and PI(3,4,5)P₃, and one of the proteins that is critical in regulating them, which is PTEN (phosphatase and tensin homolog deleted on chromosome 10).

DOMAIN	HUMAN PROTEINS CONTAINING THE MOTIF
PH	259
C2	118
C1	53
PX	30
FYVE	28
GRAM	58
BAR	10
ENTH/ANTH	9

Table 1. The number of proteins containing these domains was gathered by using the SMART database. The number here is comparable to those in Lemmon *et al.*^{7,8}. These domains were identified by architecture analysis in the Genomic mode. Genomic SMART only shows the proteomes of completely sequenced genomes and has a greatly reduced redundancy as seen with Normal SMART. ANTH, AP180 N-terminal homology; BAR, Bin, amphiphysin and Rvs; C1, conserved region-1; C2, conserved region-2; ENTH, epsin N-terminal homology; FYVE, Fab1, YOTB, Vac1, EEA1; GRAM, glucosyltransferases, Rab-like GTPase activators and myotubularins; PH, pleckstrin homology; PX, Phox homology.

1.2 PIPs, PTEN, and Disease

In advanced cancers, there is commonly a loss of heterozygosity (LOH) on the long arm of chromosome 10^{13, 14}. This has been reported at a frequency of 70% with glioblastomas, 60% advanced prostate cancers and 50% primary invasive breast cancers. PTEN is located at 10q23 which is a site that frequently experiences this LOH¹³⁻¹⁵. The types of mutations and deletions identified in this gene in multiple tumor types include insertions, missense mutations, nonsense, and frameshifts. Parsons *et al.* reported in a seminal paper that PTEN mutations occurred at a rate of 63% (5/8) in glioblastomas, 100% (4/4) prostate cancers and 10% (2/20) in breast cancers propelling the protein to the front of cancer research¹⁴⁻¹⁶. PTEN mutations are also found in endometrial tumors (34%-45%)¹⁷⁻¹⁹, bladder tumors (14%)²⁰, kidney¹⁵, and glioblastoma multiform (GBM) (20%-24%)^{19, 21, 22} (Table 2: COSMIC database)^{13, 17, 23}.

Not surprisingly PTEN germline mutations are associated with chronic tumor growth and are associated with diseases such as Cowden disease, Lhermitte Duclos disease, and Bannayan-Riley-Ruvalcaba syndrome^{7, 11, 13, 15, 24-27}. Today, germline mutations of PTEN have an umbrella term, *PTEN* Hamartoma Tumor Syndrome (PHTS). It encompasses the range of symptoms identified with PTEN mutation carriers and provides broader diagnostic criteria²⁷. Research in mouse models and *in vitro* further established the function of PTEN, and how the mutated protein leads to the progression of tumorigenesis²⁸.

PTEN was identified as a dual specificity phosphatase (DSP) when the iconic H-C-X-A-G-X-X-R-(S/T)-G sequence of that family was discovered^{14, 29}. The catalytic activity of PTEN is unique among the DSP. Its target is the 3-phosphate on the lipid PI(3,4,5)P₃

TISSUE	%POINT MUTATIONS	TOTAL SAMPLES
BILIARY TRACT	2.81	533
BREAST	3.72	5146
CENTRAL NERVOUS SYSTEM	12.4	6418
CERVIX	3.85	1092
ENDOMETRIUM	37.88	3332
EYE	3.22	311
GENITAL TRACT	2.58	194
HAEMATOPOETIC AND LYMPHOID	2.46	9807
KIDNEY	3.05	2493
LARGE INTESTINE	5.06	6169
LIVER	1.91	2570
LUNG	2.46	6293
OESOPHAGUS	1.63	1592
OVARY	3.25	2212
PANCREAS	1.16	2503
PROSTATE	6.39	2661
SALIVARY GLAND	4.46	448
SKIN	8.12	2637
SMALL INTESTINE	3.45	58
STOMACH	3.25	2029
THYROID	2.23	1747
URINARY TRACT	2.07	1016
VULVA	8.33	144

Table 2.0 COSMIC database results of PTEN point mutations for different tumor tissues. Date accessed 1/19/2018 <http://cancer.sanger.ac.uk/cosmic/gene/analysis?In=PTEN>.

as reported by Dixon *et. al*³⁰. While PTEN has some protein phosphatase activity that it exerts in the nucleus³¹, it potently targets PI(3,4,5)P₃ in the PM. When comparing the k_m between inorganic Ins(1,3,4,5)P₄ to p-nitrophenyl phosphate, there is 250-fold difference favoring the inositol derivative. Also, when comparing the specificity for the phosphoinositide targets, PTEN overwhelmingly favors PI(3,4,5)P₃. PTEN turns over this lipid 80% faster than either PI(3)P or PI(3,4)P₂³⁰. PTEN's phosphatase activity makes it an antagonist to the PI3K-Akt cell survival pathway (Figure 5)²².

PTEN's regulatory role in the PI3K-Akt pathway puts it at the center of cancer development and progression. At the beginning of the PI3K-Akt signaling pathway are the enzymes PI3K and AKT. The kinase PI3K phosphorylates PI(4,5)P₂ to produce PI(3,4,5)P₃. PI(3,4,5)P₃ influences cell survival and proliferation by inducing phosphorylation and activation of Akt kinase^{11, 32}, which signals the cell for growth, proliferation, extracellular matrix interactions, and motility. Non-functioning PTEN leads to constitutively activated Akt^{11, 30, 32}. Activated Akt is a potent cell survival that leads to tumor progression³³.

In mice, PTEN null mutations result in death by day 9.5 of development²⁸. In fibroblasts, derived from these mice, there was a dramatic loss of sensitivity to apoptotic stimuli (UV irradiation, heat shock, osmotic stress, tumor necrosis factor α (TNF- α)) where large populations of cells survived these stressors. While low levels or inactive PTEN inhibits apoptotic pathways, high levels of PTEN can lead to premature cell death. PTEN belongs to a class of "gatekeeper" tumor suppressor genes which is shared with the likes of p53, Rb and APC. These genes are vital in regulating normal cell growth, and any mutation directly contributes to neoplastic cellular growth^{13, 32}.

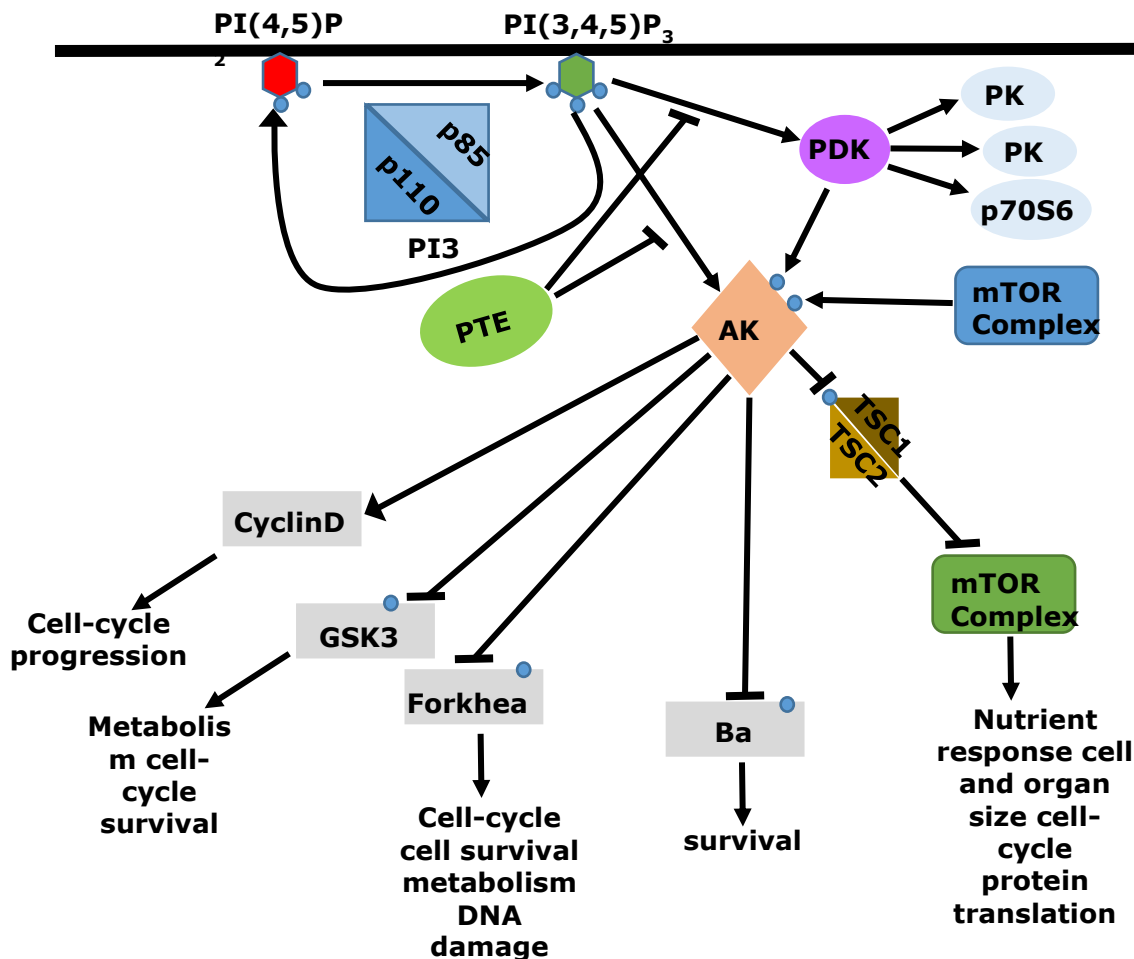


Figure 5. PI3K-Akt signaling pathway and PTEN's regulatory role in humans. Class 1a PI3K is responsible for phosphorylating $PI(4,5)P_2$ to produce $PI(3,4,5)P_3$. The kinases AKT and PDK1 can then co-localize to the membrane by binding directly to $PI(3,4,5)P_3$. PDK1 phosphorylates and activates AKT. After AKT is further phosphorylated by mTOR, it can activate and deactivate many different downstream protein targets which result in cell growth, proliferation, cell cycle progression, chemotaxis, and tumorigenesis. PTEN downregulates this pathway by dephosphorylating $PI(3,4,5)P_3$ back to $PI(4,5)P_2$. Figure adapted from Carnero, A. et al³³.

1.3 The Structure of PTEN

It was first hypothesized that PTEN could drive itself to the membrane based on its crystal structure (Figure 6) ³⁴. The signature sequence of PTEN is (H-C-K-A-G-K-G-R) 123-130aa, which is also known as the P-loop and is colored cyan in Figure 6 ^{11, 34}. PTEN has the highly conserved residues (green) required for protein phosphatase activity but also has two unique Lys residues (red)^{11, 34}. PTEN's phosphatase domain is both wider and deeper than exemplary phosphotyrosine domains. It is thought that the machinery was originally for protein phosphatase activity but has since diverged to be preferential for PI(3,4,5)P₃ ^{11, 34}. This motif is also conserved in yeast homologs of PTEN³⁴.

Overall there is weak predictive information linking the type of mutation to tumor type, but usually, there are mutations found in the phosphatase domain^{21, 26, 27, 35}. This domain (PD, purple in Figure 6) of PTEN has a central five stranded β -sheet that packs with two α helices on one side and four on the other. In the catalytic domain, residues C124 (yellow in Figure 6) and R130 (orange in Figure 6) are critical for function. The specificity of the pocket is from the interactions of K128, H93, and K125 (green, blue, and purple respectively in Figure 6). Mutation studies have shown that the K128M and H93A mutants reduce phosphatase activity towards PI(3,4,5)P₃ specifically while retaining activity towards proteins and the other 3-phosphorylated PIP derivatives. These results suggest that K128 and H93 interact with the D5 phosphate of PI(3,4,5)P₃¹⁹. The importance of this interaction is shown by the conservation of H93 in PTEN orthologs. In contrast to this, the

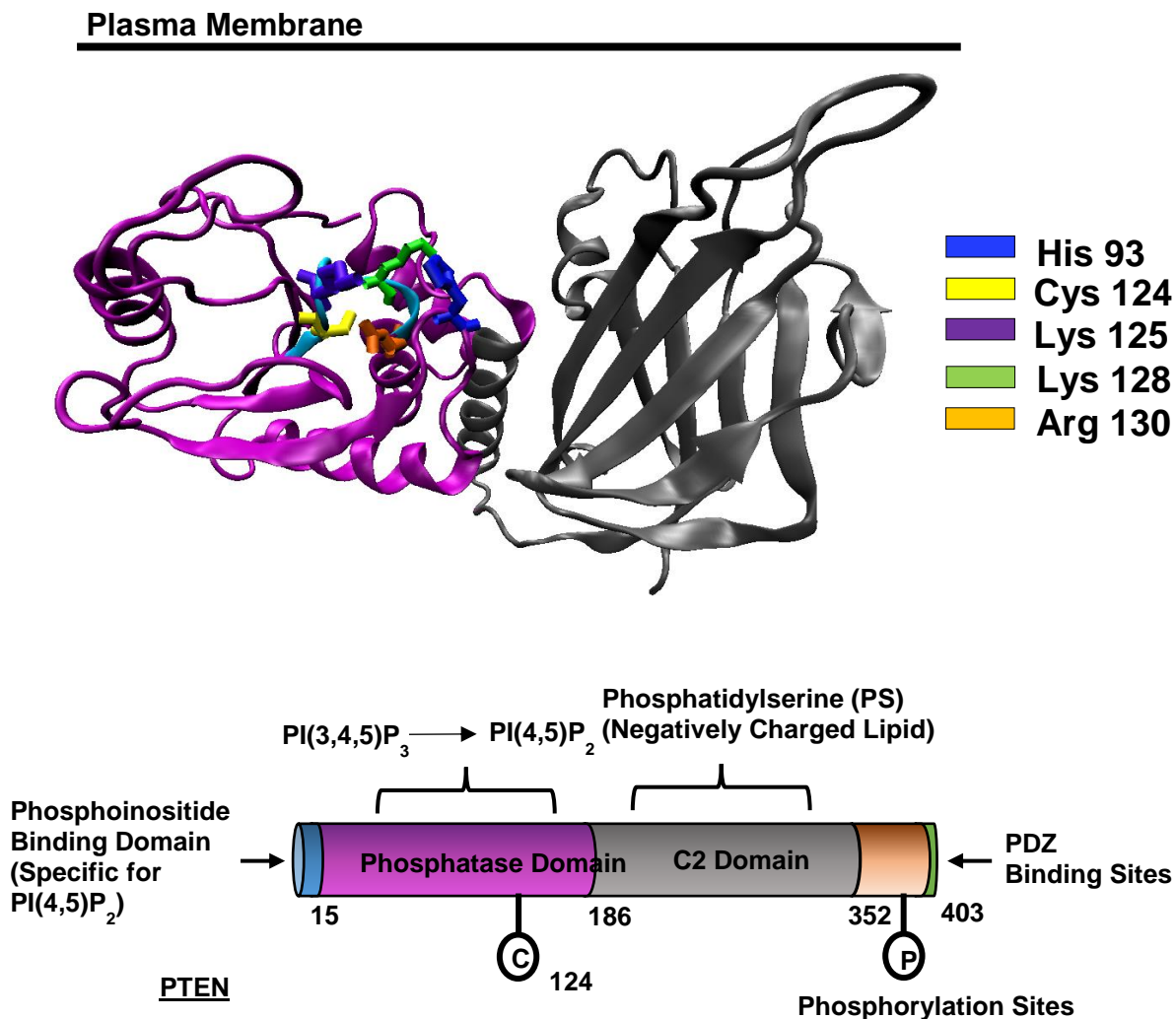


Figure 6. The structure of PTEN. (A) The partial crystal structure of PTEN lacks the N-terminal PBD domain, internal loops, and the C-terminal tail. What is represented in the crystal structure is the PD domain in purple with the catalytic P-loop highlighted in cyan. The explicit amino acids are important for selectivity and catalytic function. The C2 domain is represented in grey. It lacks the CBR3 loop which is implicated in membrane binding. (B) Is the domain map of PTEN where the size of the domains are to scale relative to the number of amino acids within each.

K125M mutation reduces the lipid phosphatase activity to all D3 containing phosphoinositides, indicating loss of PTEN function. *In vitro* experiments showed a 75% reduction in turnover and cells expressing any of these mutations proliferated extensively^{19, 34}

PTEN also contains a C2 domain (grey in Figure 6)^{8, 34}. C2 domains are the second most abundant lipid binding domains following the PH domains (Table 1)⁷. The C2 domain aids in the targeting of PTEN to the bilayer-water interface by Ca²⁺-independent binding to anionic lipids³⁶. The C2 domain structure is mostly beta sheet, and it stabilizes the PD domain through several interdomain contacts. In cancer, this highly conserved interface region between the two domains contains many mutations, leading to structural instability of the protein³⁴. The C2 domain has a conserved eight-stranded antiparallel β -sandwich structure connected with surface loops and two short α -helices between the strands^{7, 34}. The PTEN C2 domain primary amino acid sequence is not well conserved when compared to other C2 domains, but shares its sequence with Auxilin and Tensin³⁴. It was only identified as a C2 domain after the crystal structure was elucidated³⁴.

Unlike the C2 domains that bind to anionic lipids in a Ca²⁺-dependent manner, PTEN's C2 domain has only one of the three CBR loops, CBR3; which is not solved for in the crystal structure. It is hypothesized that the +5 charged loop, with two hydrophobic amino acids at its end is a significant player in the interaction with anionic phospholipids³⁴. Mutation of the putative membrane-binding residues results in inhibition of PTEN's biological activity¹⁹. C2 domains have been shown to bind PIP₂ along with the other anionic lipids⁷. PTEN's C2 domain is similar to that of PLC δ 1, PKC δ , and cPLA2^{11, 34}. The

C2 domain is followed by two PEST motifs and a PDZ consensus sequence; which not included in the crystal structure ¹¹.

Physiologically, C-terminal truncation results in rapid degradation and specifically the loss of the PEST sequence results in lower PTEN levels. Nevertheless, PTEN with deletion of this C-terminal sequence is still functional in cells. Mutations in this region are found in Cowden syndrome and can occur at Thr321, Arg323, and Arg335. As for the PDZ site, it is tempting to postulate this domain aids in PTEN targeting to protein complexes at the membrane. PDZ proteins have been shown to direct multiprotein complexes, usually at the membrane/cytoskeletal interfaces¹³. There is a requirement of the PDZ motif for the morphological changes seen in PDGF-induced membrane ruffling, but it is not a requirement for tumor suppression¹⁹. While the loss of the C-terminal tail has seemingly little consequence for PI(3,4,5)P₃ activity, emerging evidence suggests a role for PTEN C-terminus in the nucleus that is PI3K/Akt independent³¹.

Full PTEN membrane activation requires that the short N-terminal amino acid sequence binds to PI(4,5)P₂; unfortunately, this segment was not resolved in the crystal structure. This interaction with PI(4,5)P₂ enhances binding and results in allosteric activation of the phosphatase domain^{8, 36-38}. This sequence has been dubbed the phosphoinositide binding domain (PBD), and it affects the asymmetric distribution of PTEN in chemotaxing cells. Without the PBD, PTEN polarization is lost in these systems¹¹. The sequence is conserved in mammalian, frog, worm, and fission yeast orthologs and is considered a putative consensus PI(4,5)P₂ binding motif. Its sequence is Lys/Arg-X₄-Lys/Arg-X-Lys/Arg-Lys/Arg and has been found in a series of actin regulatory proteins such as villin, gelsolin, cortactin, cortexillin and other proteins as well,

MARCKS^{19, 39-43}. PTEN's structure is designed to interact with multiple lipids in the PM. The project goals are to understand how these different lipids and their lateral organization affect PTEN's membrane association and hence its function.

Chapter 2: Ensemble Kinetics

Figure 7 shows the model that is to be tested in this thesis and presented in the next two chapters. PTEN is mainly a cytosolic protein. Its substrate PI(3,4,5)P₃, resides in the inner leaflet of the plasma membrane and is rare (Figure 4). To hydrolyze the lipid, the protein must translocate from the cytosol to the membrane and then find the phosphoinositide in a complex medium (Figure 7)^{8, 11, 44}.

The first step of PTEN translocation to the membrane is dephosphorylation at S385, S380, T383, and T382. The phosphorylated state causes the C-terminal tail to fold back on its membrane binding surface, forcing PTEN to remain in the cytosol^{8, 44}. The dephosphorylated PTEN can interact with negatively charged lipids in the PM. **We hypothesize that PTEN's multiple lipid binding domains synergistically interact with lipid membranes and efficiently localize it proximal to its substrate. Depending on the spatiotemporal control of the phosphoinositides and their associated lipid partners, this is a mechanism that could lead to the polarization of PTEN in cellular systems.**

In the first project, the rate constants governing the PTEN-membrane interaction are determined by mixing multicomponent model membranes with the enzyme and following membrane association over time. Fluorescence stopped-flow spectrophotometry will be used to investigate this reaction, and KinTeK global fit software will be used to process the time dependent fluorescence intensity data. This study will differentiate the roles of monovalent lipids like PS and PI from PI(4,5)P₂ in PTEN membrane interactions, and consequently determine the step by step mechanism of the

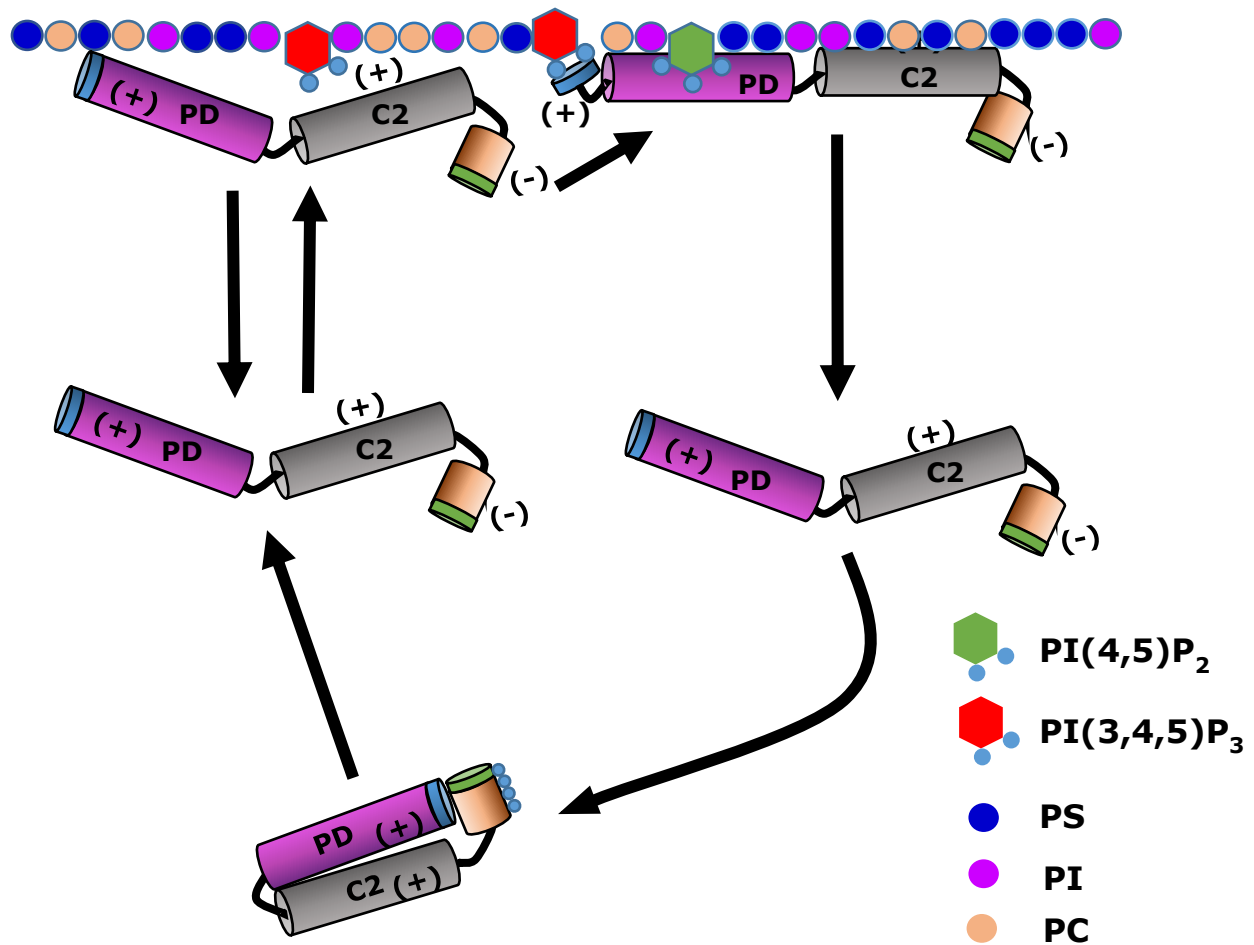


Figure 7. The hypothesis model of PTEN interacting with complex model membranes. Dephosphorylated PTEN can interact with negatively charged membranes. The binding is synergistic where multiple domains PBD, PD and C2 domain, bind to different lipids correctly targeting it to plasma membrane-like environments. We also want to explore a sub-hypothesis where mixed lipid systems known to cluster PI(4,5)P₂ will form an even more optimal environment for PTEN binding and solve the rarity paradox highlighted in figure 4.

reaction. This work is also designed to explore whether lipid domain formation affects PTEN binding.

PTEN/lipid bilayer interactions have classically been explored with the lipids PS and PI(4,5)P₂. Thermodynamic results suggest a synergistic interaction of PTEN with these two lipids, but the detailed mechanism of this interaction remains elusive. Kinetic experiments can probe the mechanism, and determine whether other anionic lipids can participate in the lipid bilayer/PTEN interaction. We explored an additional PTEN lipid

binding partner, PI. PI is the precursor to all PIPs, has been found to cluster with PI(4,5)P₂⁹, and like PS carries a (-1) charge. In this chapter, we will explore if this lateral organization of PI/ PI(4,5)P₂ mixing impacts PTEN's association⁹. If the domains of PI(4,5)P₂ indeed affect the rate of PTEN membrane binding, it indicates a level of lipid organization and influence on biology not appreciated by the classic Singer Nicolson model.

2.1 Methodology

Recombinant PTEN Expression and Purification.

Recombinant PTEN proteins (both native with cleavable N-terminal 6HIS tag [47.2 kD, PI 5.94, Extinction coefficient 42020 M⁻¹ cm⁻¹ after removing 6HIS tag] and PTEN-ybbr-6HIS [MW 49.4kD, PI 6.49]) were expressed in *Escherichia coli* BL21-(DE3) cells (New England Biolabs (NEB), Ipswich, New England) as per the instructions from NEB. The starter culture was then inoculated (starting OD 0.06) in Terrific Broth at 37 °C until the OD reached 0.6-0.8. The culture was shifted to 18 °C, and protein expression was induced with 0.05 mM isopropanyl β-D-thiogalactodide (IPTG). After 20-22 hrs., the culture was harvested.

The cell pellet (15-20g) was resuspended in 50 mL of lysis buffer (20mM HEPES, 500M NaCl, 5mM Imidazole, 10mM β-mercaptoethanol (B-ME), 0.5U/mL DNAase, 0.75% TritonX100, 5mM phenylmethylsulfonyl fluoride, 10mM benzamide HCl, pH 7.5). The lysis suspension was homogenized by passing 30 mL portions through the French Press three times or until the sample was uniform in viscosity and texture. The samples were then spun at 18,000 rpm in a Beckmann centrifuge at 4 °C for 30 min. The supernatant was collected and transferred to the ultracentrifuge and spun for an hour at 45,000 rpm at 4

°C. The clarified supernatant was collected and kept ice cold until passage and purification on the FPLC. HIS₆ proteins were separated from the crude supernatant by passing over 2x 1mL HiTrap IMAC FF column (GE).

The purified protein was taken and pooled for the final dialysis into the working buffer (20 mM HEPES pH 7.4, 150 mM NaCl, 2mM EDTA, 1mM TECP). After dialysis, the concentration was determined using a Nanodrop UV-vis spectrophotometer (Thermo Fisher Scientific Waltham, MA). The PTEN concentration was determined using the Nanodrop A280 method as outlined by ThermoFisher as well as by carrying out a Bradford assay. In addition to this, the protein quality was also checked using dynamic light scattering (DLS) to ensure that no aggregation occurred during the purification.

Lipid Vesicles

To make unilamellar lipid vesicles, the appropriate amount of lipid stock solutions are dispensed into an amber vial. The solvent is evaporated with a gentle stream of N₂ while the sample is heated to ~30°C. The vial with the lipid film is then placed in the vacuum oven overnight at ~50°C. Drying the lipid mixture above the T_m of the highest melting temperature ensures that the lipids remain well mixed during the drying process. The lipid film is re-suspended in loading buffer and vortexed for 60s. This is repeated three times with four minutes of rest in between. The multilamellar vesicles are then extruded (Avanti Extrusion Kit) through a 100nm polycarbonate membrane (Avanti, Alabaster, Al) for a total of 31 passes. The size distribution of the resulting unilamellar lipid vesicles is checked by DLS. Using this method, unilamellar vesicles with a narrow size distribution and an average hydrodynamic diameter of ~125±10nm are obtained. These vesicle suspensions are kept no longer than 24 hours⁸.

To ensure the quality of the lipid vesicles, only small chloroform stocks of lipids are kept and only for a short duration. Most importantly, anionic lipids, particularly phosphoinositides are susceptible to hydrolysis of the headgroup at the phosphodiester bond. These lipids are not kept any longer than a month in an organic solvent, and when they are used after two weeks dissolved in chloroform, the stock solutions are checked for lipid degradation by TLC.

The solvent mixtures to conduct the TLC analysis used for dansylPE, POPC, POPS, LiverPI are both 2:1 chloroform: methanol and 1:1 chloroform: methanol. When the head group is lost during degradation, you will see streaking and loss of separation on the plates. PI(4,5)P₂ is tested against 65:25:4 chloroform:methanol: conc. ammonium hydroxide and 1:1 chloroform:methanol. When the PI(4,5)P₂ is high quality, it migrates slightly above the starting line in the first mixture and fails to migrate in the second. When degraded, the sample fails to migrate in the first mixture and appears as a streak in the second. For additional information on TLC and solvent mixtures visit the Avanti Polar Lipids website for full technical details (www.avantilipids.com).

Highly accurate lipid concentrations are needed for the kinetic experiments. Lipid concentrations in the stock solutions are determined by phosphate assay analysis^{45, 46}. In brief, samples of the lipid stock solution are measured to approximate 0.05 μmol total phosphate. This is compared with the phosphorus standard (0.65mM, Sigma, St. Louis, MO) with a concentration range from 0 μM – 114 μM. The solvent is removed with a gentle stream of N₂. The lipid film is then subjected to 8.9N sulfuric acid and allowed to react at 215 °C for 25 min. Then 30% hydrogen peroxide is added to the sample vials and heated for an additional 30 min. The samples were allowed to cool, and deionized water was

added. To begin the colorimetric assay, a 2.5% w/v ammonium molybdate (VI) tetrahydrate solution is added, and the samples are vortexed, then a 10% w/v ascorbic acid solution is added, and the samples are vortexed. The color is allowed to develop for 30 mins, and the samples are added to a 96-well plate, and the absorption intensity is recorded at 600 nm.

Stopped-Flow Techniques

The SX20 stopped-flow spectrophotometer (Applied Photophysics, Leatherhead, Surrey, UK) determines the rate constants that govern reaction kinetics by measuring the temporal evolution of a fluorescence signal as a result of a chemical reaction or interaction. It is designed with a flow circuit comprised of two Hamilton drive syringes whose plungers are set against a pneumatic drive ram. For each injection, the drive ram pushes the reagents from the two syringes where they meet in a T-mixer. The T-mixer under pressure is highly efficient at mixing reagents thoroughly and quickly. The above-described process results in a dead time of only 2 ms, allowing us to investigate rapid biochemical interactions. The reagents move through and are combined in the flow circuit, they enter the optical cell (20 μ L, pathlengths 10mm X 2mm) where data collection begins.

Data collection follows the emission change over time and builds the reaction curves of the experiment. In our work, an emission intensity signal is collected once every 12.5 μ s. When 800 signals are gathered, they are averaged to a single intensity value, which is plotted against time. This is repeated for a total of 1000 points collected over 3s to generate the raw data curve. In addition to these settings, for optimal data collection, the option for *pressure hold* is also selected. This tells the instrument not to release the drive ram pressure until after the data has been collected. This option is necessary to

eliminate an artifact at 0.15 ms due to the mechanical release of the drive ram. There are three other important ways to control the signal-to-noise ratio and ensure optimal data quality:

- (1) The voltage applied to the photomultiplier tubes used to collect the emission signal can be altered. When the PMT has a higher voltage, the electronic response is more sensitive to the emission signal. There is a point of diminishing returns though because noise will begin to increase as well. The voltage must be set to the optimal value for the experiments being conducted. This value is determined by a couple of test runs.

For our work, we conducted two reactions at the edges of the titration range that was used in the association experiments. These were 1 μ M PTEN with 15 μ M lipid and 1 μ M PTEN with 300 μ M lipid (surface concentration). Please note that the lipid concentrations are those for the outer leaflet of the vesicle only (“surface concentration”) since the protein cannot access the inner leaflet lipids of the vesicle. The composition of the lipid vesicles was 30% POPS/ 68% POPC/ 2% DansylPE; this reaction is less robust compared to other vesicle compositions. Using these reactions as a standard, we can set the voltage at a value necessary to see a change in PTEN binding but will not go off scale for the more robust interactions. This value was 350V for dansyl emission change while keeping the light source and filters the same.

- (2) The light source also affects the signal-to-noise ratio. Our SX20 system is outfitted with a 280nm LED excitation source. The power supply allows us to change the output of the LED by adjusting the current from 2 mA – 20 mA.

Higher currents result in higher signals. The downside of high currents is photodamage and bleaching of the fluorophores. With our chemistry, this degradation was significant after 3 s of data collection at the highest LED current. With optimization 10 mA is the highest current within the time range of interest to ensure no bleaching effects.

- (3) Finally, the third option is to adjust the concentration of the reactants. In our experiments, our reactants are an enzyme (PTEN) and lipid vesicles. The source of the signal in these components are fluorescent molecules. In PTEN the fluorophore is intrinsic. PTEN has two tryptophans, W111, and W247. W111 is distal to the membrane binding surface and thus is unlikely to participate in the FRET transfer with the dansyl-labeled lipid. This is in contrast to W247 which is proximal to the membrane interface. This intrinsic fluorophore has an absorbance maximum that occurs at 280 nm, and its emission maximum ranges from 320 nm to 350 nm depending on the environment. In contrast to the tryptophan found in PTEN, the fluorophore DansylPE needs to be added to the vesicles making it an extrinsic fluorophore. For all the stopped-flow experiments, the composition of the vesicles always contained 2% DansylPE. The absorption maximum is 336 nm which is in the middle of the PTEN emission range. This is a key aspect in choosing a good FRET acceptor. The emission maximum of dansyl is 515 nm⁸.

The fluorescence signal is proportional to the concentration of the fluorophore as described by the Beer-Lambert law. We use a protein concentration of 1 μM . This provides a high enough signal while not being wasteful of the enzyme. For the vesicles,

we settled on 2% dansylPE of the mole composition of the total lipids composing the vesicle. This mole fraction is the minor component compared to all other lipid species in the vesicle, yet it was found that any less causes an unacceptable signal-to-noise for the lowest titration points in the experiment.

With our optimized settings for data collection, we run an experiment with our protein concentration at $1\mu\text{M}$ and measure the rate of the reaction with a series of vesicle concentrations for each lipid composition. This titration range is $10\mu\text{M}$ - $250\mu\text{M}$ (surface lipid). We found that above $300\mu\text{M}$ lipid concentration light scattering of the lipid vesicles interfered with data collection while below $25\mu\text{M}$, data for the weaker PTEN/vesicle interactions was too noisy to be analyzed with confidence. Therefore, $25\mu\text{M}$ is the lowest concentration used to define the rates that govern the PTEN/lipid reaction.

KinTek Global Fit Analysis

KinTek is a software developed to solve complex reaction phenomena observed by stopped-flow analysis. Traditionally, reaction kinetics are solved by derivatizing mathematical equations used to describe the reaction curve. However, the mathematics becomes non-trivial for complicated multi-step reversible reactions. To avoid this, analytical solutions can be derived by making simplifying assumptions and setting up reactions so that the substrate is in great excess of the enzyme. The result is that during the reaction most of the substrate is not participating, meaning the initial substrate concentration remains unchanged resulting in a pseudo first order reaction condition. Unfortunately, there are many times that a reaction needs to be done at approximate concentrations, resulting in a scenario where the simplifying assumptions are invalid. In addition to this, the tradition analytical method relies on a summation of exponential

functions, where each phase is matched to a rate constant. There are multiple examples where vital information is lost. One example is an enzyme known as ESPS, which shows a biphasic exponential response, where actually there are a total of six steps, not just two⁴⁷.

An approach to this difficult data analysis is to use a global fit software, KinTek, where the data set can be fit directly to a hypothesized kinetic model. This particular software allows formulation of the model with text. The software then defines the derivation and solves the reaction kinetics by numerical integrations determined by the values defined by the starting concentrations of the reactants, the signal output to define the data, (in our case the dansyl emission increase due to FRET) and the time course over which the reaction occurs.

A downside is that this type of data analysis can lead to an overly complex model. To address this, the software is designed to allow multiple experiments to be fit with the same model. Also, if a rate constant is explicitly known or the relationship between two rate constants (for example, a known equilibrium constant) are known, these can be held or linked, thereby constraining the results.

This global fit program utilizes multiple methods to determine the constraint and the accuracy of the results. For example, the standard error is calculated based on nonlinear regression fits. Unfortunately this method fails to reveal to what extent the fitted parameters are under constrained when the model is overly complex. Nonlinear regression is based on the well-established equations for linear regression by proposing that the best fit is defined by the parameter set resulting in the minimum sum squared error. In fact, this method tends to push the parameters to values where they no longer

affect the curves. To avoid these pitfalls, KinTek allows you to graphically inspect the constraints of the parameters to better understand the relationships between them and test the constraint of the found values.

2.2 Ensemble Kinetics of PTEN binding to Lipid Membranes

The emission intensity of dansylPE increases over time as PTEN binds to the lipid vesicles due to Förster resonance energy transfer (FRET). FRET is a phenomenon where one fluorescent molecule *donates* its excited energy to an *accepting* molecule. FRET is a radiation-less transfer, which occurs through resonance. The *accepting* molecule can either be capable of fluorescence or not. It is this distinction why Förster resonance energy transfer (FRET) or resonance energy transfer (RET) is the correct nomenclature rather than the incorrectly used fluorescence resonance energy transfer. In the case of this work, we have chosen an acceptor capable of fluorescence. It is a useful tool to study interactions since this transfer only occurs at very short distances and the two molecules must meet specific physical characteristics. There are three major physical parameters that determine if the FRET transfer occurs and if it does, the efficiency. These parameters are spectral overlap between the donor and the acceptor, dipole alignment and the distance between the two molecules. The FRET transfer efficiency as related to distance as shown in equation 1⁴⁸,

$$E = \frac{1}{1 + \left(\frac{r}{R_0}\right)^6}, \quad \text{Eq 1.}$$

where (r) is the distance between the donor and the acceptor, and (R_0) is the Förster distance. The Förster distance is the distance between the FRET pairs where there is 50% transfer efficiency. In the case of this system, PTEN carries the donor (tryptophan

247, W247) and the vesicle has the acceptor (dansylPE, 2% mol fraction). The Förster distance for this pair is 21-24Å. Since transfer efficiency drops off rapidly with increasing distance (equation 1), FRET works as a switch in our experiments. In other words, there is only transfer if the protein interacts with the surface of the membrane.

Figure 8 shows an example of stopped-flow data using the two detector system. With this setup, we could technically follow the change of emission for both fluorophores as a function of time. As expected, there is a decrease in the emission of W247 and an increase of the emission of the dansyl-PE. Of the two fluorescence intensity curves, the dansyl-PE emission has a far superior signal-to-noise ratio. Also, the W247 curve shows a significant downward slope which never comes to equilibrium, even over a period of hours. For these reasons, all further data analysis was done on the acceptor emission response to PTEN binding.

In all these data, there is a slight linear slope seen at longer times that consistently has a value equal to 0.001 ± 0.0005 for the dansyl-PE emission curves. It is negative for the dissociation experiment and positive for the association experiment. This could be due to the complicated nature of vesicle light scattering and slow aggregation overtime (a documented feature of anionic lipid-containing vesicles)⁴⁹. Another thought was that while the protein and membrane interaction can reach equilibrium quickly (PTEN moving from the aqueous environment to the membrane) there may be a slow rearrangement of the lipids that affects the dansylPE environment. The lateral movement of lipids is about 100 times slower in the membrane compared to a particle in aqueous solution. It is also known that PTEN does cause rearrangement of its binding lipids when it interacts with the surface⁹. These two phenomena, vesicle fusion and slow lateral lipid movement,

make the long time scale kinetic information complicated, its nature (exact origin) is ill defined and is beyond the goal of these experiments. What is important to note is that the simple addition of a linear slope fits the data and consistently results in the same value independent of the type of vesicle composition.

FRET only occurs when PTEN binds to anionic lipids or PI(4,5)P₂. Figure 9 shows data comparing PTEN interacting with vesicles at the same concentration but with varying lipid compositions. The PC only vesicles show no dansyl-PE emission; only when vesicles contain at least one type of anionic lipid or phosphoinositide is there a change in signal. Most studies in the literature solely report kinetic data for proteins interacting with vesicles

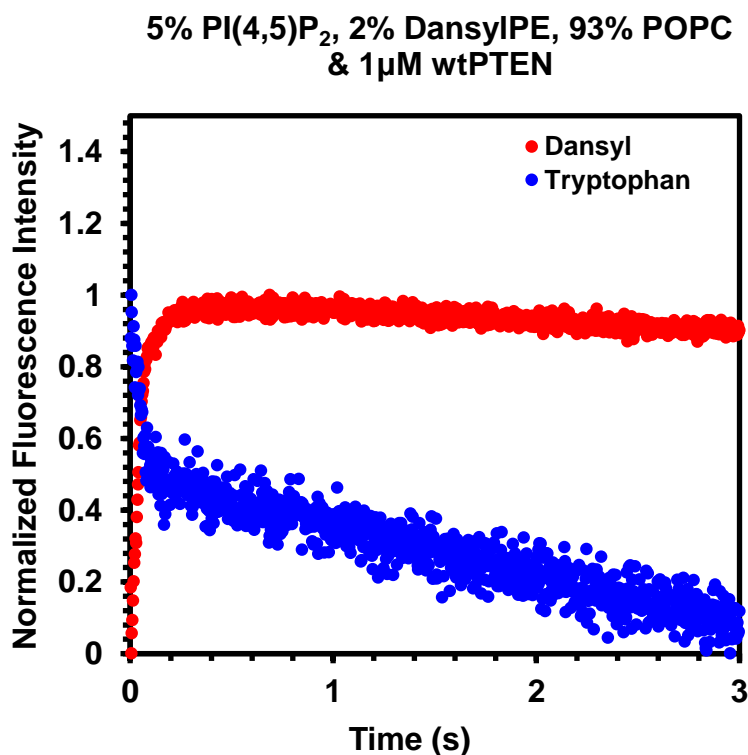


Figure 8. FRET transfer between PTEN W247 and dansyl-PE when PTEN binds to a vesicle composed of 5% PI(4,5)P₂, 2% DansylPE, 93% PC. The dansyl emission intensity increases as the tryptophan (W) emission intensity decreases through time. For the kinetic experiments, we choose to follow the dansyl emission intensity change because, in comparison to the W emission, the data had a superior signal to noise ratio.

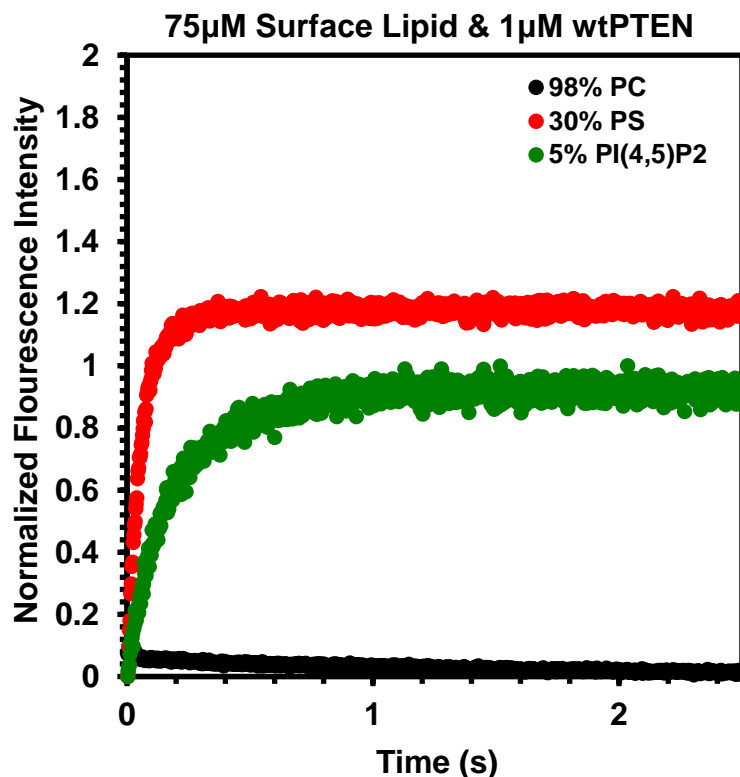


Figure 9. Comparison of PTEN binding to vesicles with different mixed lipid compositions. Each curve represents a different 75 μM lipid composition mixed with 1 μM PTEN; the compositions are 98% POPC, 2%DansylPE (black); 30%POPS, 2%DansylPE, 68%POPC (red); 5%PI(4,5)P₂, 2% DansylPE, 93%POPC (green). As can be seen, PTEN will only bind when there are lipid binding partners in the vesicle as can be seen from the occurrence of FRET

with simple lipid compositions. Since our goal is to determine the rate constants governing PTEN interactions with various lipids, our study needs to be extended beyond this general approach. To our knowledge, this type of kinetic work with multicomponent lipid vesicles and nuanced pre-steady state kinetics has not been thoroughly described in the literature. To take care in interpreting our data and to avoid over-interpretation, we will use two methods of data analysis. First, we use an analytical method where the experiment is set up under pseudo-first order conditions. Second, we use the global fit software, KinTek, a more sophisticated analysis, which should produce more accurate rate constants. With these two techniques, we hope to determine the effects of lipid composition on the mechanism of PTEN binding as well as provide a standard for the field for analyzing kinetic data for proteins binding to complex lipid systems.

Titration of vesicles into PTEN results in a range of rates dependent on reactant concentration (Figure 10). Each of these curves fits to the function in equation 2⁵⁰⁻⁵².

$$Rate = A * (1 - e^{-k_{obs} * t}) + m * t + C, \quad Eq2.$$

where (A) is the amplitude, (k_{obs}) is the observable rate, and (m) is the correction factor and (t) is time. The k_{obs} is dependent on the lipid concentration; this informs us that this is at least a second-order reaction. The relationship of k_{obs} to the true rates constants governing the reaction is shown in equation 3⁵⁰⁻⁵².

$$k_{obs} = k_{on} * [Lipid] + k_{off}, \quad Eq.3$$

(k_{on}) is the association rate constant of the reaction, ([Lipid]) is the lipid concentration and (k_{off}) is the dissociation rate constant. To discriminate between the values of k_{on} and k_{off} with the analytical method, k_{obs} is plotted as a function of lipid concentration (Figure 11)

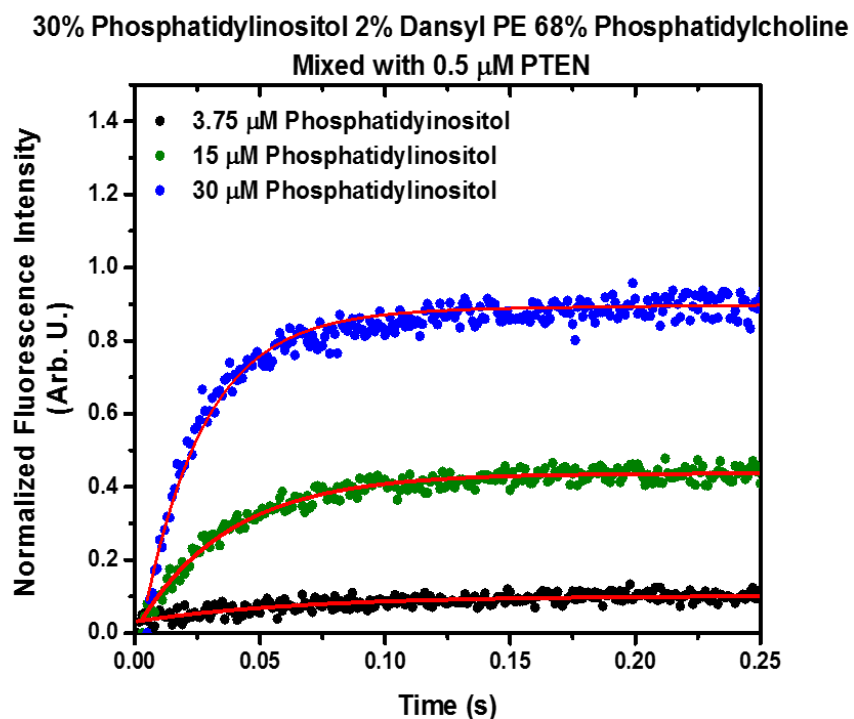


Figure 10. Stopped-flow dansyl-PE fluorescence intensity curves upon PTEN binding to mixed PI/PC vesicles. The experiment is carried out under pseudo-first order conditions where the lipids are in excess. Each curve represents a different lipid concentration of the mixed vesicle composed of 30%PI, 2%DansylPE 68%PC mixed with 0.5 μ M PTEN. The concentration series spans 15uM-250uM surface concentration (the concentration in the inset are normalized to the mole fraction of PI). The titration for each vesicle composition was repeated at least three times. The slope was determined from the exponential fit shown in equation 2. This slope is the k_{obs} .

and fit to equation 3. The shape of this titration curve can inform us whether the reaction is rate limiting or not. Figure 11 illustrates this; if the curve is linear (blue), that indicates a nonrate-limiting process. If the data is nonlinear it indicates a rate-limiting step was captured in the experiment. For the simple binding in our case, all the data show strong linear trends. An example of the fit is shown in Figure 12 with PTEN mixed with 30% PI, 2% DansylPE, 68% PC.

The k_{on} is dependent on the concentration of vesicles. For the kinetic analysis of protein binding to multicomponent lipid vesicles, a general problem is which concentration to use for the lipid concentration. There are four principal ways to account for the lipid concentration in equation 3. (1) We could use the total surface lipid concentration (zwitterionic plus anionic lipid concentrations), (2) we could consider only the combined concentration of all anionic lipid species (excluding zwitterionic lipids), (3) we could normalize the anionic lipid concentration to the total charge (PI and PS are (-1), PI(4,5)P₂

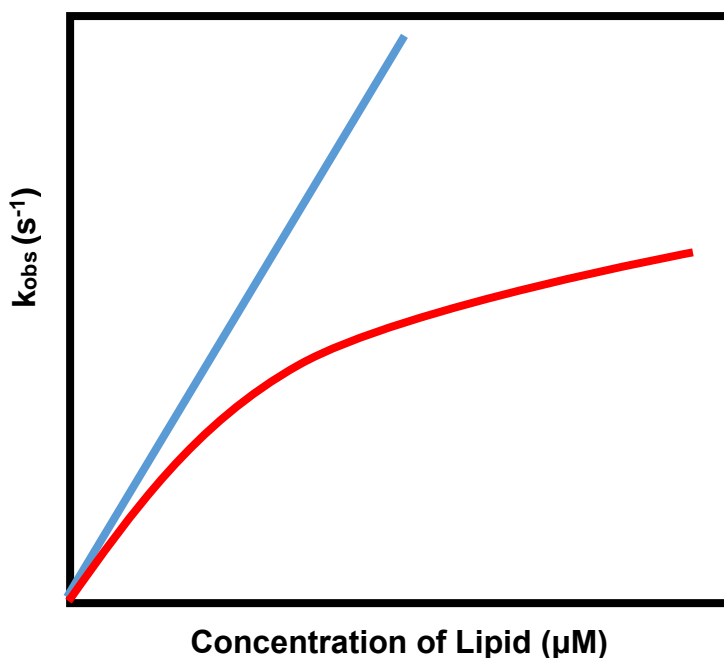


Figure 11. General graph showing the difference between a rate limited, two-step reaction (red), and a one-step reaction (blue). This is determined by plotting k_{obs} from a titration experiment as shown in Figure 10 against the concentration of lipid.

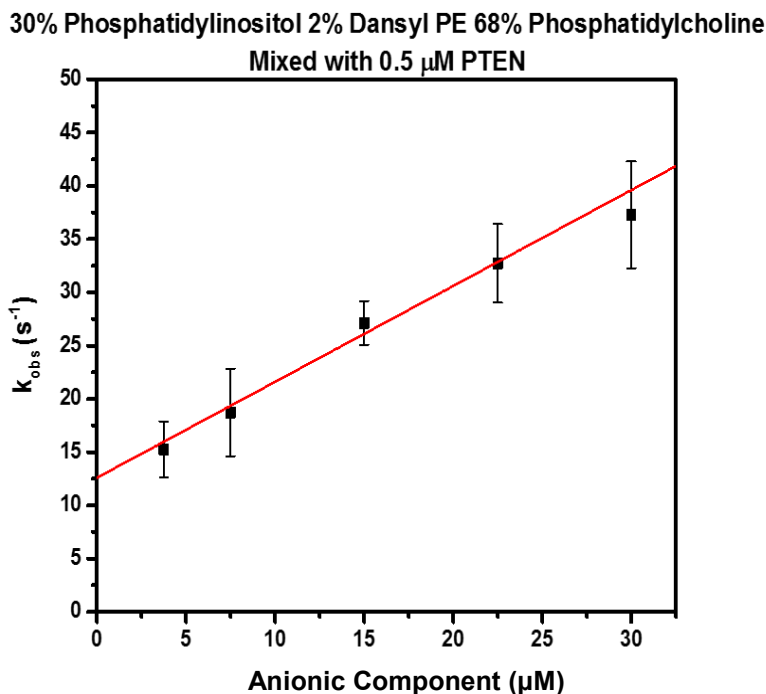


Figure 12. Rate constant k_{obs} as a function of lipid concentration, (anionic component), of vesicles composed of 30%PI 2%DansylPE, 68%PC. The data are fit to equation 3 where k_{on} and k_{off} are derived. Each of these graphs are an average of at least three different titrations.

is (-4)), or (4) we could only take into account the major anionic lipid that participates in PTEN binding, i.e., target lipid concentration. Each approach has its pitfalls but also provides valuable information about the system. We used a holistic method and choose to analyze the data with all four concentration approaches.

Kinetic analysis of PTEN association using the total lipid concentration (Figure 13)

The PTEN on-rates using the total lipid concentration for the analysis are given in Figure 13. There is little difference between the association rates in the majority of compositions explored. We will first compare the lipid vesicle systems with only one anionic lipid species present in the lipid mixture. For the single negatively charged lipids PS and PI, we find essentially the same on rates independent of their surface concentration. For 98% PS or 98% PI the k_{on} is 0.22-0.26 ($\mu\text{M}^{-1}\text{s}^{-1}$). The physiologically

more relevant cases, 30% PS and 30% PI, have similar k_{on} -values. Unlike these two systems, 5% PI(4,5)P₂ shows a slower on-rate (0.18 ($\mu\text{M}^{-1}\text{s}^{-1}$)). While the on-rate for this system is lower than the other single anionic lipid systems (though technically the error bars overlap), the total anionic lipid concentration in the PI(4,5)P₂ containing vesicle is significantly lower. The comparison of the binary anionic lipid systems reveals some differences between the PS and PI-containing vesicles. Comparing 30% PI/ 5% PI(4,5)P₂ to 30% PS/ 5% PI(4,5)P₂, we find that the PI system has a slower on-rate of 0.12 ($\mu\text{M}^{-1}\text{s}^{-1}$) compared to the PS system at 0.2 ($\mu\text{M}^{-1}\text{s}^{-1}$). This trend is repeated in the 10% PI/ 1% PI(4,5)P₂ vs. 10% PS/ 1% PI(4,5)P₂ case but overall the on-rate values are lower (0.08 ($\mu\text{M}^{-1}\text{s}^{-1}$) for PI/ PI(4,5)P and 0.12 ($\mu\text{M}^{-1}\text{s}^{-1}$) for PS/ PI(4,5)P₂. PTEN binding to PS only vesicles in comparison to PI only vesicles shows little difference in the on-rates, but when these anionic lipids are mixed with PI(4,5)P₂, a slower association rate is observed for the

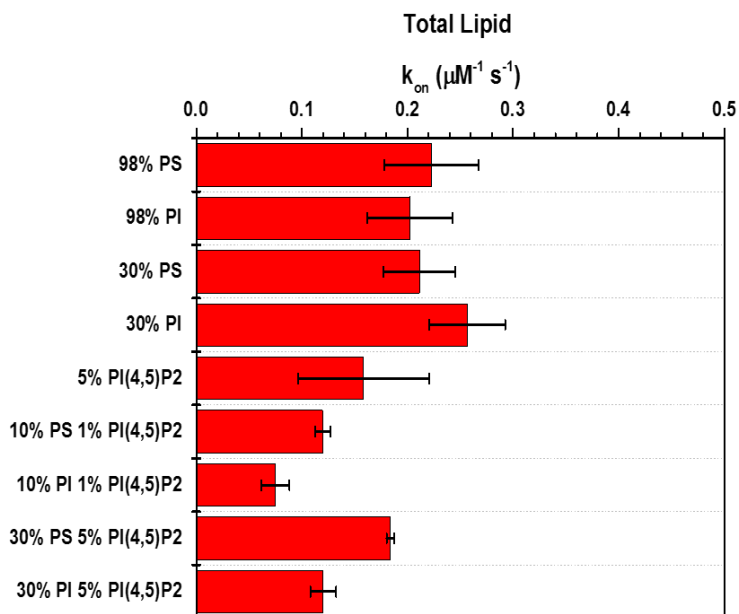


Figure 13. Comparison of k_{on} rates derived from the analytical method using total surface lipid concentration in the analysis of PTEN binding to mixed lipid systems. 98% PS, 98% PI, 30% PS, and 30% PI have an average k_{on} rate of 0.2 $\mu\text{M}^{-1}\text{s}^{-1}$. 5% PI(4,5)P₂ is slower with a rate of 0.15 $\mu\text{M}^{-1}\text{s}^{-1}$. The multicomponent vesicles have a slower rate compared to the PS and PI single component models. Also, the multicomponent models favors a faster rate with PS containing vesicles compared to PI; 10% PS/ 1% PI(4,5)P₂ rate is 0.12 $\mu\text{M}^{-1}\text{s}^{-1}$; 10% PI/ 1% PI(4,5)P₂ rate is 0.08 $\mu\text{M}^{-1}\text{s}^{-1}$; 30% PS/ 5% PI(4,5)P₂ rate is 0.18 $\mu\text{M}^{-1}\text{s}^{-1}$; 30% PI/ 5% PI(4,5)P₂ rate is 0.12 $\mu\text{M}^{-1}\text{s}^{-1}$.

PI/PI(4,5)P₂ vesicles in comparison to the mixed vesicles containing PS. Another observation is that the binding kinetics of PTEN to vesicles with 30% PS or 98% PS is similar, suggesting a limiting effect of the overall surface charge (number of charged lipids) and the rate of PTEN binding. A surprising result is the observation that PTEN association with binary anionic lipid vesicles is slower than for vesicles with a single anionic lipid (see 30% PI vs. 30%PI/ 5%PI(4,5)P₂). We believe this is due to differences in the lateral lipid distribution (domain formation) of the systems resulting in crowding effects of surface-bound PTEN.

Kinetic analysis of PTEN association using only the concentration of the anionic lipid species (Figure 14)

One has to be careful when interpreting the data obtained through a kinetic analysis based upon the concentration of only the anionic lipid component because lower concentrations skew the result towards faster k_{on} rates. This is exemplified when comparing the k_{on} rates for 98% anionic lipid (PS or PI) to 30% anionic lipid (PS or PI). While we found the k_{on} values to be the same when the total lipid concentrations are used, we found when we normalize the concentration to the mole fraction of anionic lipid the rates for 30% anionic lipid are faster than for 98% anionic lipid. The primary reason is that the unit of the rate constant is $\mu\text{M}^{-1}\text{s}^{-1}$, i.e., a lower concentration will lead to a higher rate constant. Nevertheless, some valuable information can be extracted from such an analysis. Using this approach, PI(4,5)P₂ emerges as a very potent PTEN binding partner (see Figure 14) since its k_{on} in the presence of PI(4,5)P₂ is by far the fastest. For the other vesicle systems with only one anionic species, 30% anionic lipid (PS or PI) shows a faster association when compared to 98% anionic lipid (PS or PI), but again the chemical identity

of the monoanionic lipid does not seem to matter. 10% PS/ 1% PI(4,5)P₂ shows an association on par with 30% monoanionic vesicles, whereas 10% PI/ 1% PI(4,5)P₂ exhibits a slower PTEN association rate than the corresponding 30% PI vesicles. Finally 30% PS/ 5% PI(4,5)P₂ and 30% PI/ 5% PI(4,5)P₂ show the second slowest association, underscoring the observation we made in the previous section that the binary lipid systems exhibit slower association rates presumably due to an altered lipid distribution. The take home message of this analysis is that PI(4,5)P₂ is a more potent PTEN binding partner compared to the single charged anionic lipids. These data furthermore support the previous observation that there is an upper limit to increasing surface charge as highlighted by the reduced association rates for 98% anionic lipid.

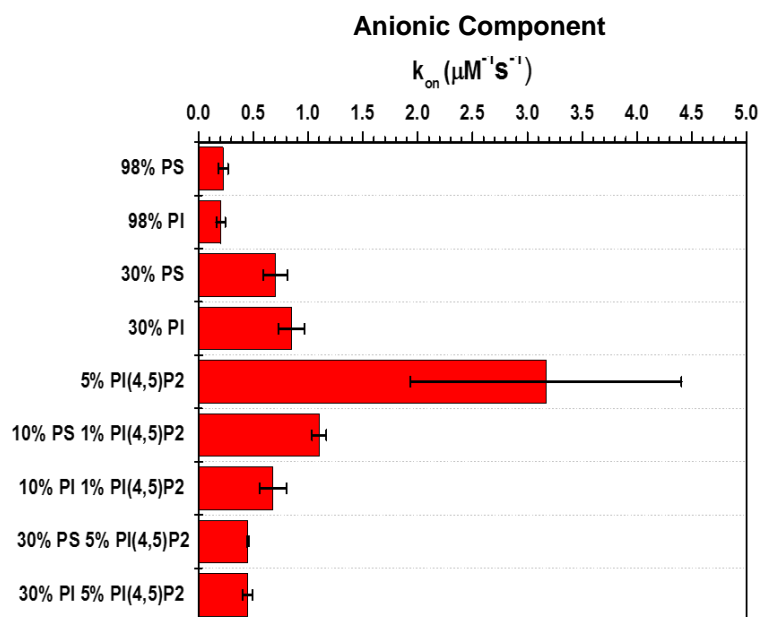


Figure 14. Comparison of the anionic component k_{on} derived from the analytical method of PTEN binding to lipids. 5% PI(4,5)P₂ shows the fastest rate at $3.2 \mu\text{M}^{-1} \text{s}^{-1}$. 98% PS and 98% PI rate is $0.2 \mu\text{M}^{-1} \text{s}^{-1}$, but 30% PS and 30% PI are more potent and have an average k_{on} of $0.54 \mu\text{M}^{-1} \text{s}^{-1}$. The multicomponent vesicles are more comparable to the 30% single models. The multicomponent models still favors a faster rate with PS containing vesicles compared to PI; 10% PS/ 1% PI(4,5)P₂ rate is $1.2 \mu\text{M}^{-1} \text{s}^{-1}$; 10% PI/ 1% PI(4,5)P₂ rate is $0.54 \mu\text{M}^{-1} \text{s}^{-1}$; 30% PS/ 5% PI(4,5)P₂ and 30% PI/ 5% PI(4,5)P₂ rate is $0.5 \mu\text{M}^{-1} \text{s}^{-1}$.

Kinetic analysis of PTEN association using a charge normalized lipid concentration

(Figure 15)

When the data is analyzed by normalizing the anionic lipid concentration with the charge of the respective lipid, we account for PI(4,5)P₂ exhibiting a significantly higher charge (and hence electrostatic potential) than the other anionic lipids (PS and PI). To calculate the mol% of these vesicles 10% PS/ 1% PI(4,5)P₂ would account for 14% of the total lipid with PS having (-1) valence and PI(4,5)P₂ with (-4) valence. Looking at the single anionic lipid vesicles, we see that 30% PS, 30% PI and 5% PI(4,5)P₂ (20% valence charge) all have the same association rate. 98% PS or 98% PI still shows a reduced rate in comparison to the other systems despite the increased surface potential. This supports the hypothesis that there is an upper limit to the effect of the surface charge on PTEN

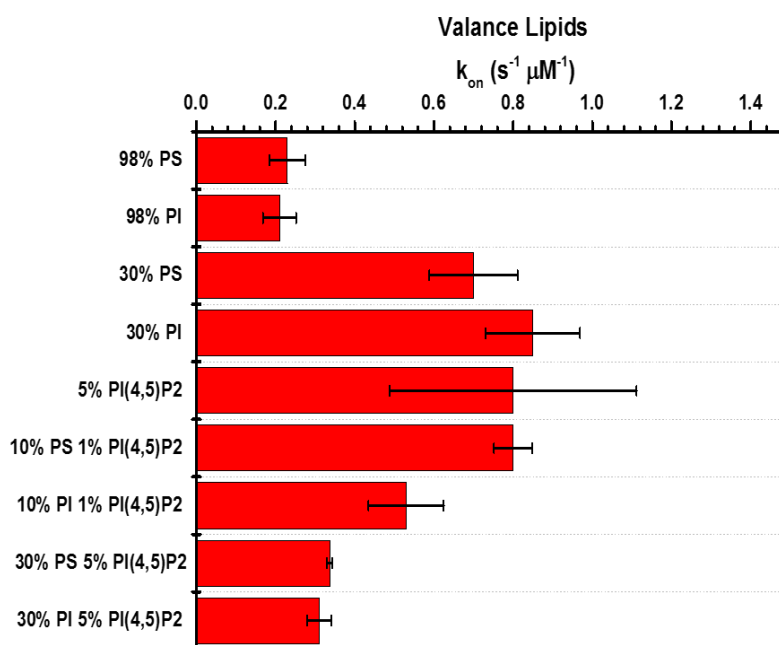


Figure 15. Comparison of the charged normalized k_{on} derived from the analytical method of PTEN binding to lipids. 5% PI(4,5)P₂ (20% valence charge), 30% PS, and 30% PI have the same k_{on} of $0.78 \mu M^{-1} s^{-1}$. The multicomponent models still favor a faster rate with PS containing vesicles compared to PI. The lower potential system, 14%, as compared to the 50% system has a faster k_{on} ; 10% PS/ 1% PI(4,5)P₂ rate is $0.78 \mu M^{-1} s^{-1}$; 10% PI/ 1% PI(4,5)P₂ rate is $0.5 \mu M^{-1} s^{-1}$; 30% PS/ 5% PI(4,5)P₂ and 30% PI/ 5% PI(4,5)P₂ rate is $0.3 \mu M^{-1} s^{-1}$.

binding. When comparing multicomponent vesicles, there are significant differences between 10% PS/ 1% PI(4,5)P₂ and 10%PI/ 1% PI(4,5)P₂ with the PS/ PI(4,5)P₂ vesicle having a faster PTEN association. This trend continues with 30% PS/ 5% PI(4,5)P₂ and 30% PI/ 5% PI(4,5)P₂ though it is not as dramatic and not at a statistically significant level. Again, we highlight that at a 50% surface valence composition the association is reduced.

Kinetic analysis of PTEN association using the “target” lipid concentration (Figure 16)

The final way to analyze these data is to explore the rate constants using “target” lipid concentration for the kinetic analysis. The target lipid is defined as the lipid that makes the strongest interaction with PTEN when in mixed systems. For the vesicle systems with only one anionic lipid, the target lipid is that anionic lipid. For vesicles with two anionic lipids, it is PI(4,5)P₂. The reasoning is PI(4,5)P₂ interacts with PTEN specifically via hydrogen-bond formation, which should be stronger than pure electrostatic interactions. The chemistry matters in this type of interaction, meaning that the other bisphosphate-phosphoinositides PI(3,4)P₂ and PI(3,5)P₂ cannot replace PI(4,5)P₂. This is in contrast to the non-specific electrostatic interactions seen with PS or PI. Here, either lipid is just as good as the other when they are in single anionic component vesicles.

Focusing first on the lipid vesicles with a single anionic lipid, the fastest association is seen with 5% PI(4,5)P₂ followed by 30% anionic lipid and then 98% anionic lipid. Obviously, this is the same result we obtained in Figure 14 where we accounted only for the anionic lipid species. The 10% PS/ 1% PI(4,5)P₂ vesicle system shows the fastest PTEN association rate followed by 10% PI/ 1% PI(4,5)P₂ then 30% PS/ 5% PI(4,5)P₂ and finally 30% PI/ 5% PI(4,5)P₂. These data magnify the difference between the PS and PI

lipids in the multicomponent anionic lipid vesicles. In these mixed lipid systems, the PS-containing vesicles showed a faster PTEN association rate than the vesicles with PI.

Looking at the graphs holistically we can come to some conclusions about PTEN association with mixed lipid vesicles. When we account for the total available lipid PC/PS/PI(4,5)P₂ like we did in the first analysis; we are essentially testing the effects of vesicle type on PTEN association. If the association of PTEN was only affected by the total surface potential, we would expect the bars to trend with increasing charge. While we see this slightly between 5% PI(4,5)P₂ and the 30% anionic lipid, PTEN binding appears to saturate at higher anionic lipid concentrations. The data that are shown in Figure 13 illustrate that PTEN lipid binding kinetics is not simply proportional to the surface

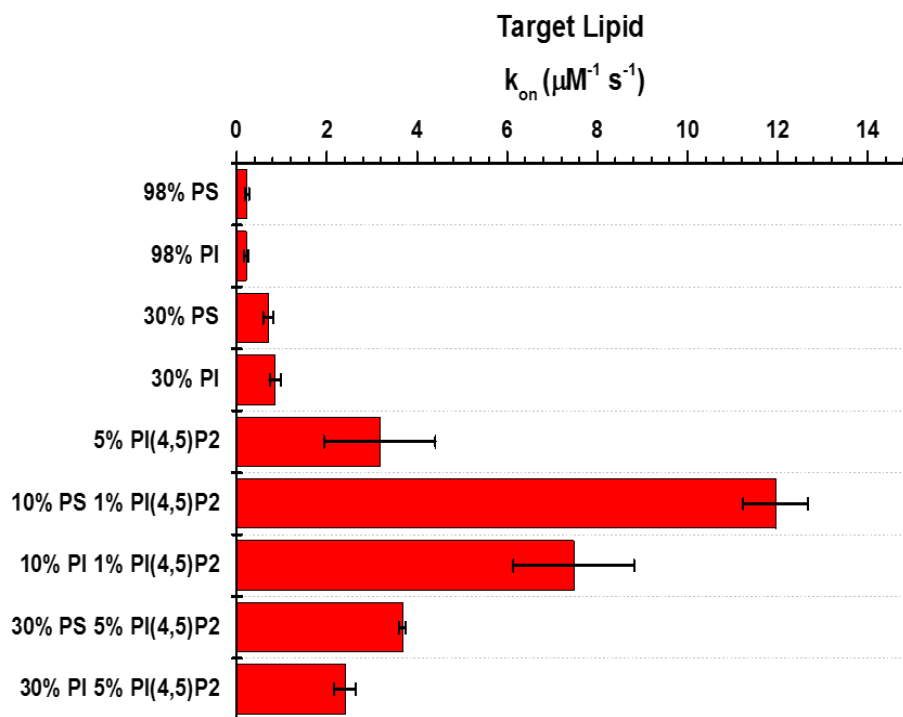


Figure 16. Comparison of the k_{on} values when using the target lipid concentration for the kinetic analysis method of PTEN binding to lipids. 5% PI(4,5)P₂ has the fastest k_{on} of the single component anionic vesicles at $3 \mu\text{M}^{-1} \text{s}^{-1}$, followed by 30% PS and 30% PI with a k_{on} of $0.78 \mu\text{M}^{-1} \text{s}^{-1}$ followed by 98% PS and 98% PI at $0.2 \mu\text{M}^{-1} \text{s}^{-1}$. The overall fastest binding is 10% PS/ 1% PI(4,5)P₂ with a rate of $12 \mu\text{M}^{-1} \text{s}^{-1}$ followed by 10% PI/ 1% PI(4,5)P₂ with a rate of $7.5 \mu\text{M}^{-1} \text{s}^{-1}$ then 30% PS/ 5% PI(4,5)P₂ at $3.5 \mu\text{M}^{-1} \text{s}^{-1}$ and finally 30% PI/ 5% PI(4,5)P₂ with a rate of $2.5 \mu\text{M}^{-1} \text{s}^{-1}$. This method of analysis highlights the difference between the PS and PI in multicomponent vesicles. In both cases, PS has a faster rate compared to PI which is not apparent with the single component vesicles.

potential. The k_{on} values presented in Figure 14 utilized only the concentration of the anionic lipid component(s) since PC is not participating in the binding of PTEN (Figure 10). These data highlight that PI(4,5)P₂ is a more potent binder than either PS or PI. When these single charged lipids are mixed with PI(4,5)P₂, a decrease in the PTEN association rate is observed. This suggests that the complex morphology of these ternary lipid vesicles impact the kinetics of PTEN binding. This underscores earlier findings by our group^{9, 36, 53-55} that PTEN binding to anionic lipids and PI(4,5)P₂ is highly synergistic.

To ensure that the observed effect of PI(4,5)P₂ on PTEN binding is not just from the increased charge of the lipid in comparison to the other anionic lipid species, we also investigated the PTEN association rates as a function of total valence charge (Figure 15). Here 5% PI(4,5)P₂, 30% PS, and 30% PI showed little difference, whereas the 98% PI or 98% PS vesicle systems showed a decreased PTEN association rate. The trend of PTEN binding to PS/ PI(4,5)P₂ having a faster association rate than the PI/ PI(4,5)P₂ system is also found for this analysis approach.

This may suggest that when there is a single component anionic vesicle, the protein is driven to the vesicle surface through electrostatic interactions and hence the overall negative potential as defined by the total valence charge of the lipid(s). And this potential will determine the k_{on} -rates. However, above ~30-40% anionic lipid, an increased overall surface potential will not increase the k_{on} -rates, i.e., the system apparently reaches saturation (as evidenced by the slower rate for 98% anionic lipid). This is in contrast to when there are multiple lipid-binding partners; the association is no longer determined strictly by the surface potential.

Lastly, we analyzed the kinetic data by using the target lipid concentration as input for the calculation of the k_{on} -rates. In the single anionic lipid cases, it is just the mole fraction of the anionic lipid. For the mixtures, we focus only on PI(4,5)P₂. Here we see the fastest association with 10% PS/ 1% PI(4,5)P₂ followed by 10% PI/ 1% PI(4,5)P₂. 5% PI(4,5)P₂ and 30% PS/ 5% PI(4,5)P₂ are next then 30% PI/ 5% PI(4,5)P₂ and finally 30% anionic lipid with 98% anionic lipid being the slowest. This again demonstrates that PI(4,5)P₂ has a role beyond being an electrostatic contributor. If this were the case, we would expect the combination of lipids PI(4,5)P₂/ anionic lipid to change with the overall potential.

The data for vesicle systems with anionic lipid/PI(4,5)P₂ show that PTEN gets to the interface through electrostatic interactions and “something else.” Some of this is, of course, due to the more potent (-4) charge of PI(4,5)P₂ but the interaction of PTEN with these mixed systems is also affected by the second anionic lipid. The data for the single anionic lipid vesicles show that only up to a certain total potential PTEN association rates increase. The lack of increase of association rate with increasing surface potential indicates that there may be surface crowding effects on the vesicles that inhibit PTEN binding. This surface crowding may also be a contributing factor for the decrease in PTEN association rates in the anionic lipid/PI(4,5)P₂ vesicles. This is highlighted in the difference between PI and PS mixed PI(4,5)P₂ vesicles. There is evidence that PI clusters PI(4,5)P₂ into domains.⁹ We originally thought that this clustering would cause an increase in local potential and therefore, would drive the protein faster to the surface. These data show the opposite. In a scenario where there is a domain of PI(4,5)P₂, with 20 to 50 lipids, the protein may only bind to a few them, however, due to the footprint of the protein a

significantly larger fraction is covered and inaccessible to other PTENs. As a result, there is a reduction in the number of binding sites available for other PTEN molecules. Protein crowding is also highlighted in the vesicles that have 30% anionic lipid vs. 98% anionic lipid. Somewhere around 30 mol% charge there is a limit at which the surface area is maximally covered by this protein, and thus any further increase in overall charge will not affect PTEN's rate of association. *An important outcome of our analysis of PTEN association rates with various mixed vesicles is that any procedure one might choose in terms of lipid concentration will overestimate the amount of lipid binding partners available for the protein molecules to bind to. In other words, for surface morphologies with clustered lipids, the k_{on} -values are a low estimate of the actual k_{on} -values since the amount of effective lipid concentration available for binding is lower than the calculated lipid concentration (irrespective of the method that is being used for the analysis)*

Kinetic analysis of PTEN dissociation from mixed vesicles

The data in Figure 17 shows the dissociation rate constant (k_{off}) determined by the analytical method (Figure 12, equation 3). With k_{off} , a high rate is synonymous with the protein quickly falling off the vesicle, while a low or small rate indicates strong binding. The dissociation data reveals more pronounced differences between each of the lipid vesicle compositions. Whereas before the vesicles with 30% anionic lipids (PI or PS) vs. 98% anionic lipids (PI or PS) showed no difference in the association rate constants; there is a dramatic difference observed for the dissociation rate constants. The vesicles with the higher concentration of anionic lipids (PI or PS) show a considerable stabilization of the wtPTEN/vesicle interaction. While there was virtually no difference found for the PTEN association rate constant for the anionic lipid PI vs. PS, we find an additional stabilization

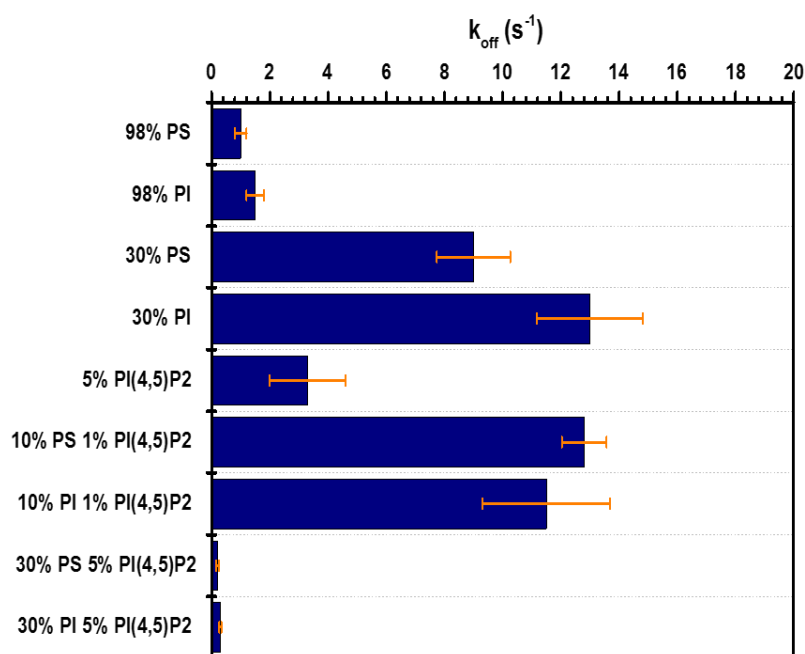


Figure 17. Comparison of the k_{off} values derived from the analytical method (Figure 12, eq. 3) of PTEN binding to lipids. The stability of PTEN binding to single anionic component vesicles trend with surface potential. Binding to 30% PS and 30% PI is the weakest, but there is also a stabilizing effect with the PS vesicle. This trend is also recapitulated with 98% single component anionic lipids. The k_{off} value for PTEN binding to 5% PI(4,5)P₂ is almost as low as it was found for the 98% anionic lipid vesicles, suggesting that PI(4,5)P₂ interacts more strongly with PTEN than the single valence lipids. This idea is further supported in the 10% PI/ 1% PI(4,5)P₂ and 10% PS/ 1% PI(4,5)P₂ vesicles. By far the strongest binding is found for 30% PS/ 5% PI(4,5)P₂ and 30% PI/ 5% PI(4,5)P₂, which exhibit significantly slower dissociation rates than 98% anionic lipid binding scenario.

of PTEN association with the PS lipid. This may suggest that the PS/PTEN system is not purely non-specific electrostatic but also has a minor contribution that is specific for PS. In other words, our hypothesis that PS is fully replaceable by PI seems to be incorrect based on these data (see below for further discussion). The rate constant for PTEN dissociation from 5% PI(4,5)P₂/ PC vesicles has a value between the 30% and 98% single anionic lipid vesicles, highlighting how much more potent PI(4,5)P₂ is in stabilizing the PTEN/vesicle interaction.

Significant differences are observed for PTEN's interaction with PI(4,5)P₂/ anionic lipid (PS or PI) mixed vesicles. For 30% anionic lipid (PS or PI) with 5% PI(4,5)P₂ there is a dramatic increase in the stability of PTEN binding. This is less pronounced for vesicles with 10% anionic lipid and 1% PI(4,5)P₂. These results highlight three fundamental properties of the PTEN/anionic lipid/PI(4,5)P₂ complex: First, PTEN requires a minimal charge density for binding; apparently the 10% anionic lipid/1% PI(4,5)P₂ does not provide an electrostatic environment that supports robust binding. Second, while PTEN binds more stably to vesicles with PS as the single anionic lipid than it binds to vesicles with PI as the only anionic component, this preference for PS is not observed in vesicles that also contain PI(4,5)P₂. In fact, for the 10% anionic lipid/1% PI(4,5)P₂ vesicles there might be a slight preference for the PI-containing system (presumably due to PI/PI(4,5)P₂ domain formation). Third, even a modest amount of the PI(4,5)P₂ dramatically increases the stability of the PTEN-vesicle complex. While we found preferential binding of PTEN to 30% PS over 30% PI vesicles and concluded that PI could not fully replace PS in the interaction of PTEN with the membrane, we find for the binary anionic lipid system that binding to PI/ PI(4,5)P₂ vesicles is at least as good (and probably better) than binding to

PS/ PI(4,5)P₂ vesicles. We hypothesize that the PI/ PI(4,5)P₂ domain formation offsets the slightly less favorable direct binding of PTEN to PI in comparison to PS.

Equilibrium analysis of PTEN binding to mixed lipid vesicles

We next combine these data sets to obtain K_d values for PTEN binding. K_d values obtained through a kinetic analysis are not true equilibrium constants since equilibrium constants are a thermodynamic quantity and thus must be measured with a thermodynamic experiment. This is because our kinetic experiments do not capture every binding step and environmental change that occurs as the system reaches equilibrium. For example, we have set up the experiment to follow the binding of PTEN and lipid, but we know from IR studies that there is a protein conformation change which is difficult to account for in these kinetic experiments³⁶. The values we are reporting are therefore not “TRUE” thermodynamic equilibrium constants that account for all the changes in our system. Nevertheless, the trends of the K_d values seen here are close to what has been previously reported, (Table 3), in our lab as well as our collaborator's lab.

Figure 18 shows the K_d values using the different lipid vesicles analyzed with the total lipid concentration (i.e., including the PC concentration). Again, we are primarily looking at the compositions as a type of vesicle and not distinguishing between which lipids PTEN can interact with. Analyzing the single anionic component vesicles from strongest to weakest it follows 98% anionic lipid, 5% PI(4,5)P₂, and then 30% anionic lipid. The multicomponent vesicles show that 30% anionic lipid/ 5% PI(4,5)P₂ has remarkable strong binding whereas PTEN binding to 10% anionic lipid/ 1% PI(4,5)P₂ is fairly weak. These data illustrate that the binding is driven by the stability of the complex as determined by the k_{off}.

Redfern et. al. Tryptophan Quenching	Total Lipid Kd (μM)
5% PS, 93% PC, 2% PyrenePE	508 +/-13
25% PS, 73% PC, 2% PyrenePE	259 +/- 20
5% PI(4,5)P ₂ , 93% PC, 2% PyrenePE	163 +/- 6
10% PI(4,5)P ₂ , 88% PC, 2% PyrenePE	72 (error not reported)
5% PS, 5% PI(4,5)P ₂ , 88% PC, 2% PyrenePE	41.1 +/- 4.8

Table 3. Thermodynamically determined Kds of PTEN binding to multicomponent lipid vesicles³⁵.

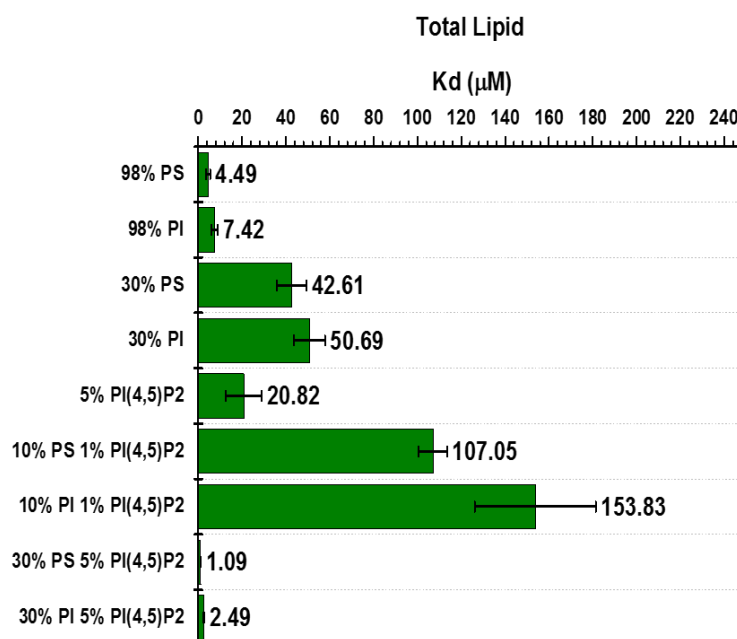


Figure 18. Kd values of PTEN binding to various vesicles (total lipid concentration). These data were analyzed using the total lipid available and were determined by dividing $k_{\text{off}}/k_{\text{on}}$. The strongest interactions are 30% PS/ 5% PI(4,5)P₂ and 30% PI/ 5% PI(4,5)P₂. The closest set is the 98% anionic lipid, which is 10-fold weaker than 30% PS/ 5% PI(4,5)P₂. 5% PI(4,5)P₂ which has a value 20-fold weaker than the multicomponent lipid model. This supports the hypothesis that the mixture of anionic lipid and phosphoinositide interacts with PTEN synergistically.

Figure 19 normalizes the results to the total anionic lipid for the K_d calculation (i.e., PC component excluded). For the vesicles with a single anionic lipid, we see that the difference between PTEN binding to the PI and PS containing vesicles becomes more defined (though technically the difference between K_d values for the 30% PS vs. 30% PI is not statistically different), whereas PTEN binding to 5% PI(4,5)P₂ is strong. The trend that is seen in the anionic lipid/PI(4,5)P₂ combination vesicles follows the trend as seen for the K_d values obtained by the total lipid analysis. 30% anionic lipid/ 5% PI(4,5)P₂ has the most potent binding, though the gain in binding strength over the 5% PI(4,5)P₂ single component system is less pronounced. PTEN binding being stronger when mixed with the PS/ PI(4,5)P₂ system than when mixed with the PI/ PI(4,5)P₂ system is maintained with this analysis.

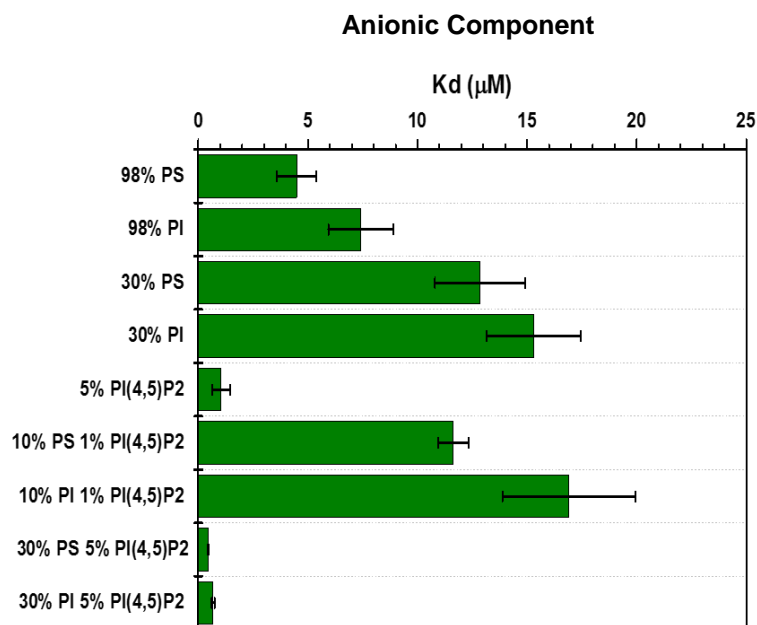


Figure 19. K_d values of PTEN binding to vesicles analyzed by using only the anionic lipid concentration. The strongest interactions are still 30% PS/ 5% PI(4,5)P₂ and 30% PI/ 5% PI(4,5)P₂. Followed by 5% PI(4,5)P₂, though the difference is not as significant as total lipid. This is followed by 98% anionic lipid than 30% anionic lipid. The trend where PS has a stronger interaction held in this analysis.

In Figure 20, we account for the differences between the valence charges of the lipids, where PS/ PI have a (-1) charge, and PI(4,5)P₂ has a (-4) charge. This translates for a 5% PI(4,5)P₂ vesicle to (-20) surface charge/ vesicle, and 30% PS/ 5% PI(4,5)P₂ vesicle would be (-50). Despite considering the higher charge, 5% PI(4,5)P₂ has a binding which is still stronger than we find for 98% anionic lipids. This indicates that there is additional stability engendered to the complex from PI(4,5)P₂ beyond increased potential. This interpretation continues to support the hypothesis that PTEN interaction with PI(4,5)P₂ and anionic lipids is a synergistic binding.

Figure 21 is calculated using the target lipid contribution; this drives home the effect of PI(4,5)P₂ on PTEN binding. We examined the binding considering only the target lipid (strongest PTEN/ lipid interaction). This means for a single anionic lipid vesicle the anionic

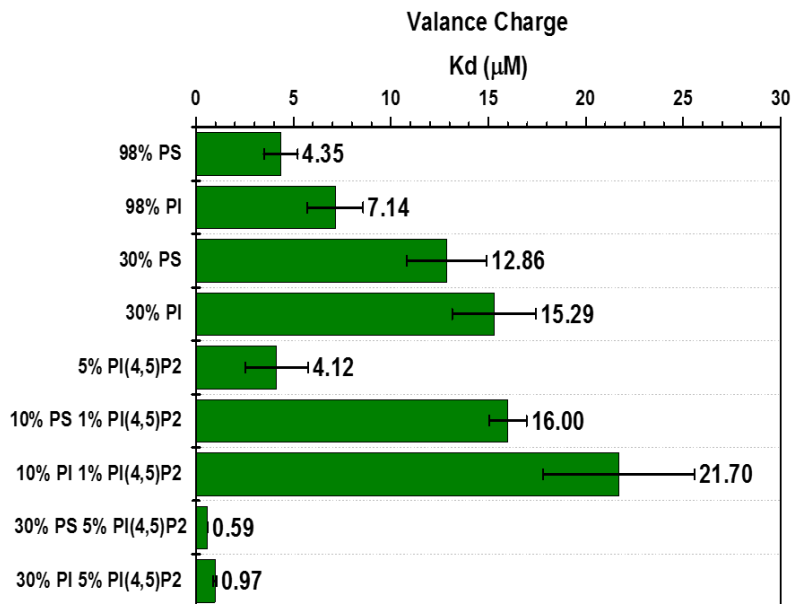


Figure 20. Compares the K_d values of PTEN binding vesicles analyzed by total valence contribution. The strongest interactions are still 30% PS/ 5% PI(4,5)P₂ and 30% PI/ 5% PI(4,5)P₂. These interactions are followed by 5% PI(4,5)P₂, but this is now on par with 98% anionic lipid. This is followed by 98% PI and then 30% anionic lipid. The trend where PS has a stronger interaction held in this analysis. This suggests that when PI(4,5)P₂ is on its own its (-20) anionic charge is on par with a (-98) single valence anionic vesicle. This again shows how potent a binder PI(4,5)P₂ is compared to traditional anionic lipids.

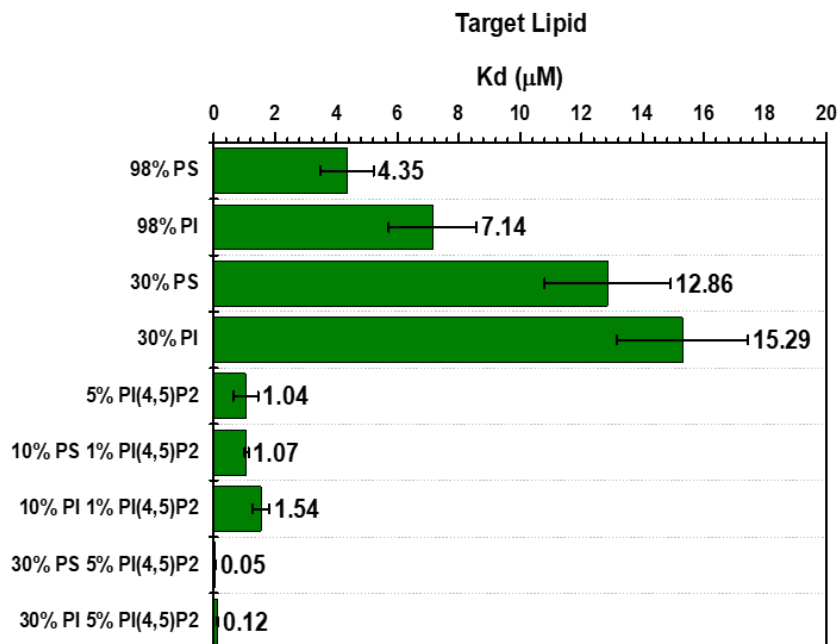


Figure 21. Compares the K_d values of PTEN binding to vesicles analyzed by target lipid concentration. The target lipid analysis singles out the contribution of PI(4,5)P₂ in the mixed anionic lipid vesicles. With the equilibrium constants we see that the strongest binding is with 30% PS/ 5%PI(4,5)P₂ followed by 30%PI/ 5% PI(4,5)P₂. 30 PS/ 5%PI(4,5)P₂ is 21 times stronger than 10%PS / 1%PI(4,5)P₂ and 30% PI/ 5%PI(4,5)P₂ is about 13 times stronger than 10% PI/ 1% PI(4,5)P₂. Another interesting comparison to make is that 5% PI(4,5)P₂ has the same binding constant as 10% PS/ 1%PI(4,5)P₂ and is a little stronger than 10% PI/ 1%PI(4,5)P₂.

lipid concentration is used. For the multi-anionic component vesicles, we report only the mol fraction of PI(4,5)P₂. This is most clearly seen when comparing 5%PI(4,5)P₂ and the 1% PI(4,5)P₂/ 10% anionic lipid. Here the addition of the anionic lipid makes 1% PI(4,5)P₂ comparable to 5% PI(4,5)P₂ vesicle. The addition of 30% anionic lipid to 5% PI(4,5)P₂ dramatically increases the binding, in particular, PS makes the interaction 21 times stronger.

What have we learned from the analysis of the kinetically derived K_d values? First, the data displayed the same trends in PTEN binding strengths as was previously found by using thermodynamic methods (Table 3). Second, PTEN appears to show stronger binding to the PS /PI(4,5)P₂ system than to the PI/ PI(4,5)P₂ system. This is rooted in the faster PTEN association with the PS/ PI(4,5)P₂ containing vesicles (the dissociation of

PTEN from the PI/ PI(4,5)P₂ is, at least for the 10% anionic lipid system, slower than for the PS/ PI(4,5)P₂ system). As noted above, the slower PTEN association to the PI/ PI(4,5)P₂ is most likely due to lipid clustering and the associated limitation of accessible lipid. This highlights the difficulty in comparing protein binding to vesicles with complex lipid compositions and morphologies. *Based on the kinetic data presented above and the calculated K_d values, it might be that the best measure of the protein binding strengths are the dissociation rates since they are mathematically independent of lipid concentration.*

2.3 Global Analysis.

A more rigorous kinetic analysis is to fit the stopped-flow data globally. In this analysis, we import a titration set (Figure 22) like with the analytical method but fit all the curves to a kinetic model simultaneously. The simplest model is:



where (P) is the PTEN concentration, (L) is the surface lipid concentration, and (PL) is the PTEN-lipid complex concentration. The output signal is defined by the FRET signal that occurs during binding:

$$\text{Output signal} = a \cdot PL,$$

where (a), is a multiplier for the output signal. This simple model accounts for the data when PTEN is mixed with single anionic component lipid vesicles composed of either PS or PI.

The model for PTEN binding to vesicles containing PI(4,5)P₂ need two steps to account for the data (Figure 23 a,b). The model to define these data is:



where the additional step is (bPL) bound PTEN-Lipid, signifying a strongly bound protein-vesicle complex. The signal output also has an additional value:

$$\text{Output signal} = (a \cdot \text{PL} + b \cdot \text{bPL}),$$

As shown in Figure 23b, this additional step fully accounts for the titration series. The results of these fits have been compiled in Figure 24.

The first conclusion that can be drawn from the data presented in Figure 24 is that the rate-limiting step is the first step. Interestingly, this step shows remarkably similar values for all vesicle systems ($0.2 - 0.3 \mu\text{M}^{-1}\text{s}^{-1}$), except the 10% anionic lipid/ 1% PI(4,5)P₂. The $k_{\text{on}1}$ values are largely the same as the k_{on} values found for the total lipid analytical approach. There is no dependence on the surface potential above ~14%, counting total valance contribution from the lipids. The $k_{\text{off}1}$ also follows the same trends as found using the analytical method. What the global fit revealed, is the second step not

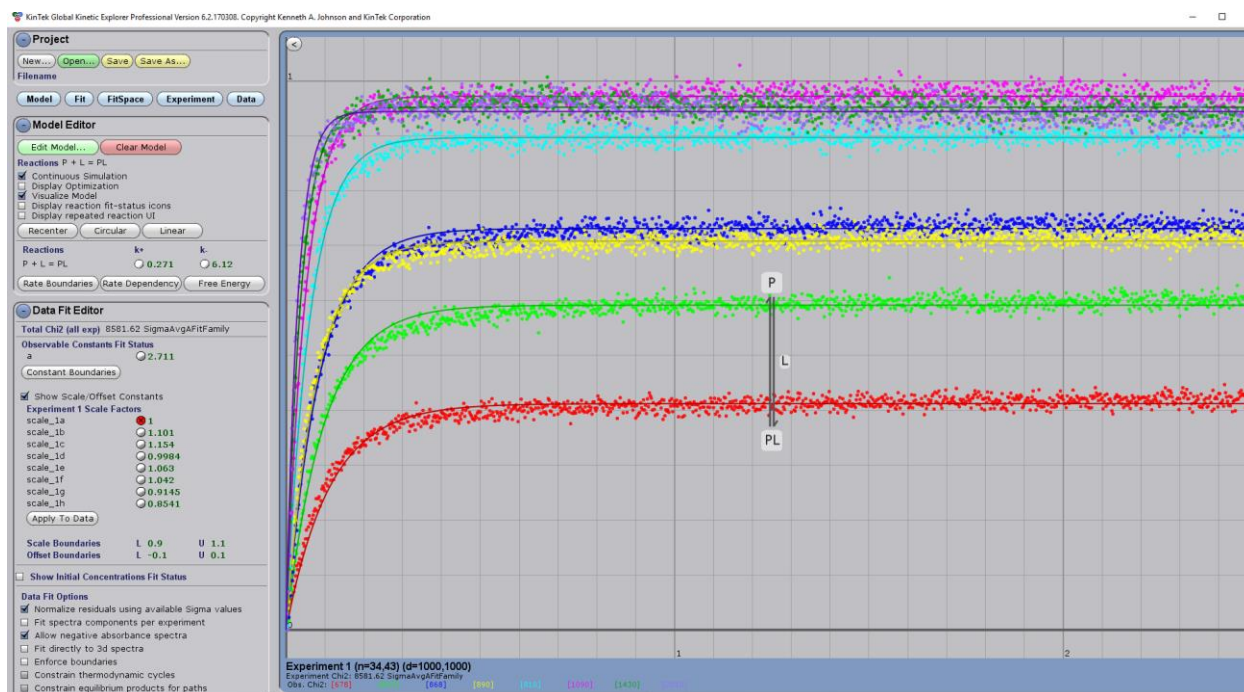


Figure 22. An example of a single component fit. This data set is fully accounted for by the model $P + L = PL$. The data is fit simultaneously to the model to derive the rate constants.

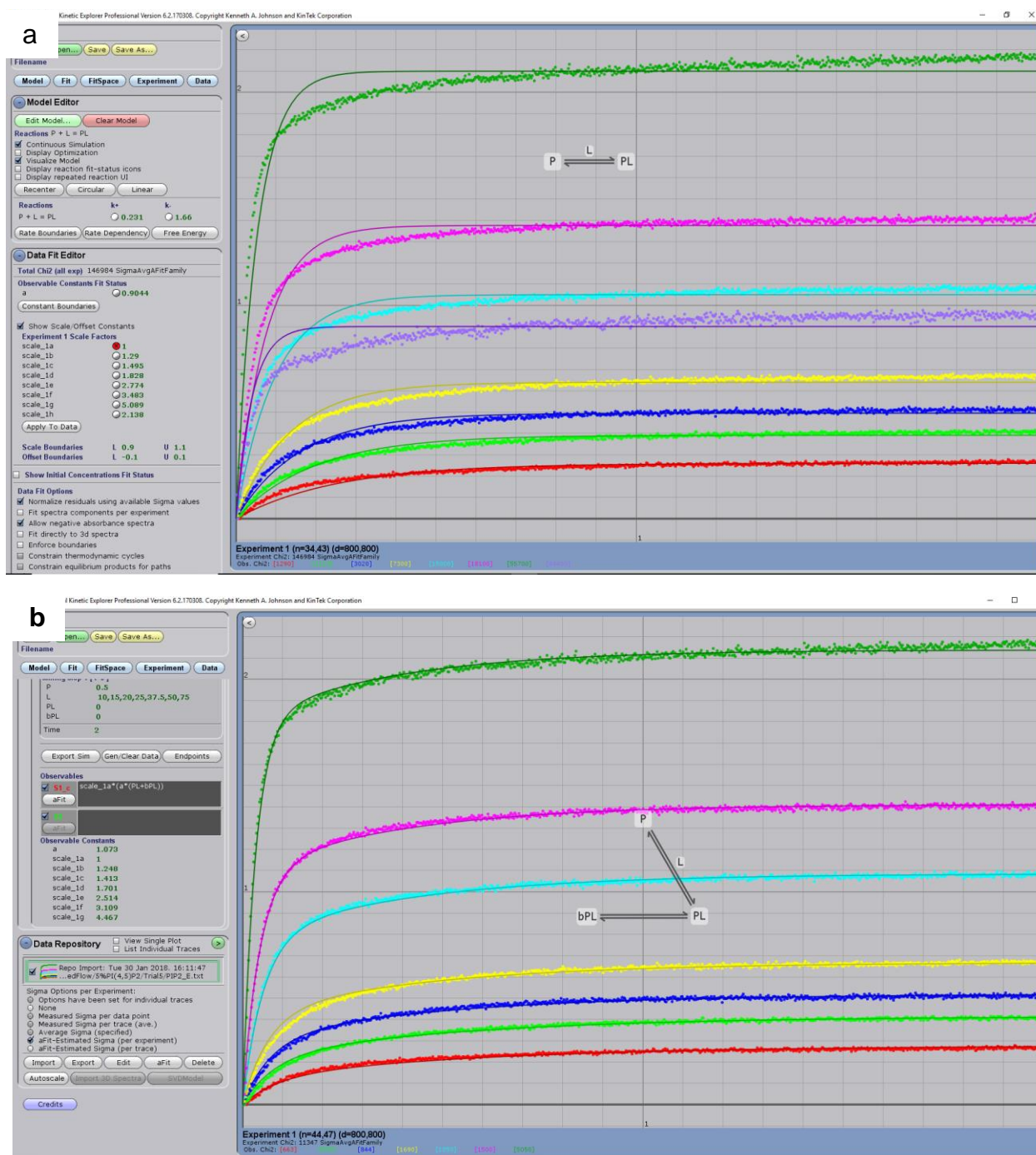


Figure 23. An example of a two-component fit of the stopped-flow spectrophotometric data. This data set is fully accounted for by the model $P + L = PL = bPL$. (a) The top figure shows the result when this data set is forced to a single component fit. Clearly, the model cannot account for the experimental data. (b) This graph has the additional step added to the model. All curves fit nicely into the model indicating that this reaction has a least to two steps.

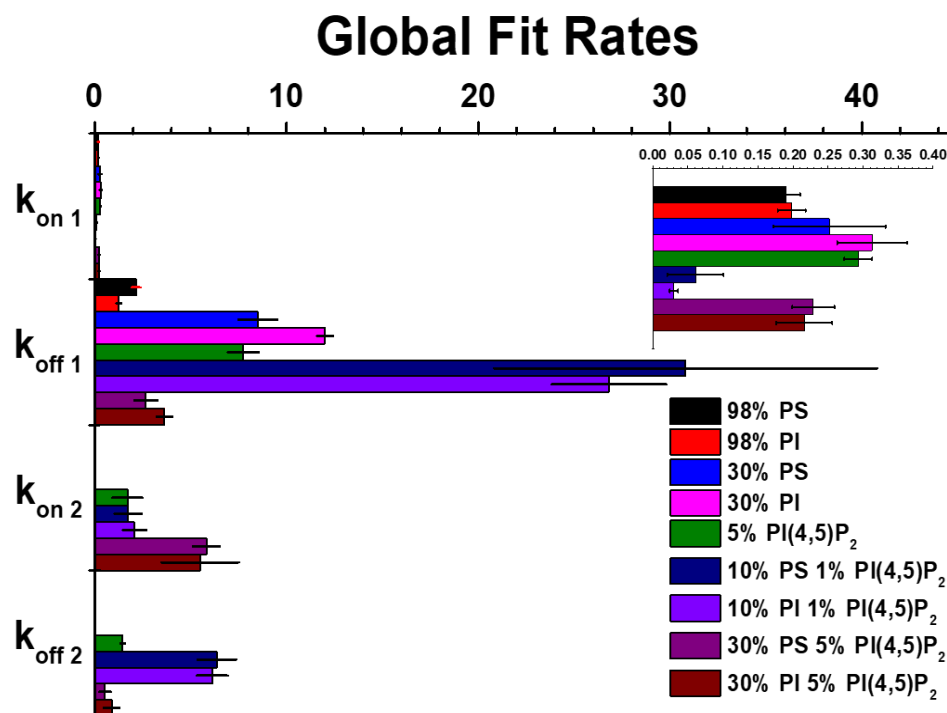


Figure 24. The compilation of all the global fit rates by step of PTEN mixed with multicomponent model vesicles. Inset is the k_{on1} expanded. When PI(4,5)P₂ is present the model goes from a one-step to a two-step description.

found using the analytical analysis. This second step occurs only when PI(4,5)P₂ is present in the vesicle system.

The second step results in a stronger PTEN-vesicle complex. The rates determined for k_{on2} show a fast transition; nearly 10-fold faster than the initial interaction characterized by k_{on1} . This interaction is also strengthened by a slower and thus more stable k_{off2} . The decrease in the k_{off} is a little less than 10-fold as well.

Figure 25 compares the global fits in terms of their K_d values. The K_d values were calculated for each step as well as for the overall process i.e. k_{off2}/k_{on1} . The K_d_{overall} nicely follows the data as determined by the analytical method as well as previously reported results in the lab. The one exception is the 5% PI(4,5)P₂ data. In this data set K_d_{overall} shows a very strong interaction where the analytical fit and previously reported

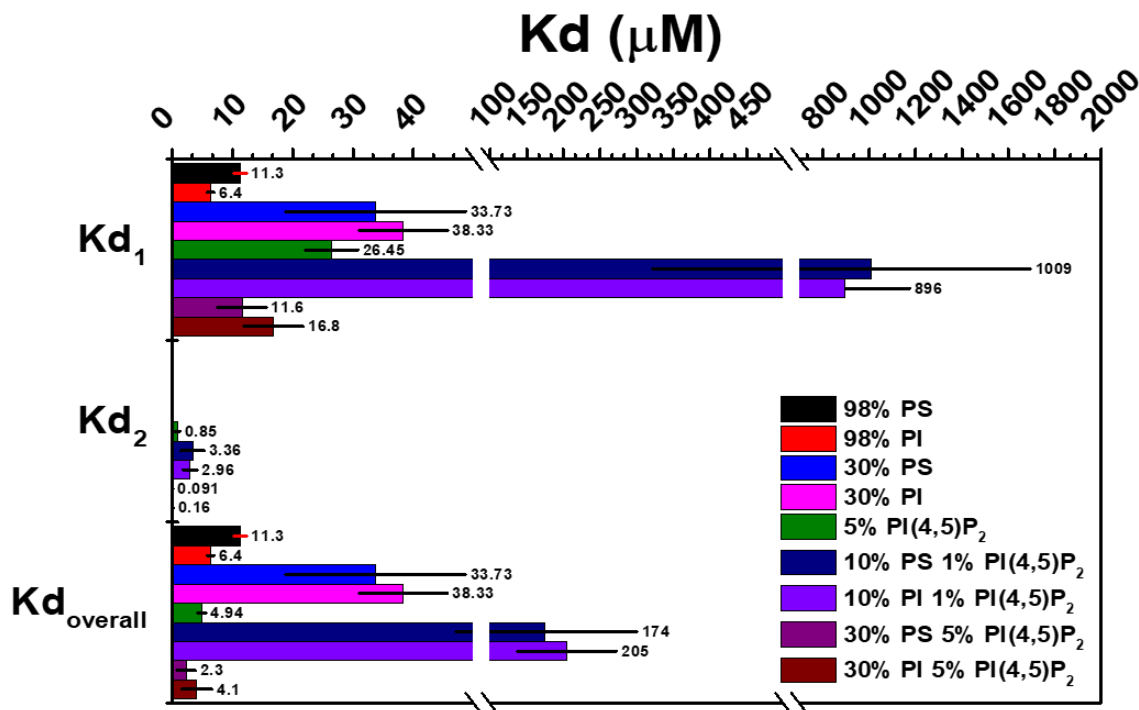


Figure 25. The Kds calculated for each reaction step. Kd_1 is k_{off1}/k_{on1} , Kd_2 is k_{off2}/k_{on2} , and $Kd_{overall}$ is k_{off2}/k_{on1} . The $Kd_{overall}$ from the global fit follows that $Kd_{TotalLipid}$ of the analytical data set, except for 5% PI(4,5)P₂. With this system, the Kd_1 from the global fit matches the analytical data better.

thermodynamically determined Kd shows weaker binding. There is a better comparison between the Kd_1 of the global fit and the other 5% PI(4,5)P₂ data.

2.4 Discussion of Ensemble Kinetics

“Coincidence detection” is a common hypothesis seen in the peripheral binding of plasma membrane proteins. The idea is that proteins use multimodal binding domains, each of which interacts with a unique lipid substrate. In the plasma membrane, these lipids are usually PI(4,5)P₂ and PS. Examples of enzymes that leverage this process are PKC α , myotubularin, and PTEN⁷. PTEN coordinates two distinct lipid sites which are the PBD and the C2 domain. We sought to push this hypothesis one step further by hypothesizing that there may be enhanced binding when the lipid substrates are clustered into domains. There is evidence in previous work that the anionic lipid PI can cluster

PI(4,5)P₂. It is a tempting thought that PI, rather than PS acts as the partner lipid in PTEN binding. It has a (-1) valence charge like PS but also has an additional characteristic that it is the precursor to all phosphoinositides. Also, a cluster of the monovalent lipid with PI(4,5)P₂ could form a potential well and drive the protein to the membrane. The results of these experiments have shown quite unequivocally that this is not the case.

The first hurdle we had to overcome was how to conduct the data analysis. It is apparent from the experiments that the rates are affected by the concentration of the substrates. The result means that the reaction is at least second order. The question with mixed lipid vesicles is how to define the concentration, since they will affect the association rate. The most obvious method is to use the concentration of the vesicles. Our vesicles are monodispersed, so the vesicle number and the lipids making them up are proportional. Our first brush at the calculation is to use the total surface lipid concentration. Using this method, we are testing the effects of the vesicle type on PTEN vesicle binding. The other option is to exclude the neutral lipid component which is known not to contribute to the binding; we dub this total anionic lipid concentration. Next, we can account for the valence of the anionic lipids. PI and PS have a valence of (-1) and PI(4,5)P₂ (-4). This is a necessary analysis to consider since the increased potency of PI(4,5)P₂ could merely be from being a more potent electrostatic contributor rather than a unique stronger interaction such as hydrogen bonding. Finally, we can account for the mol% of the “target” lipid. For the single anionic lipid component vesicles, this is rather simple. With the dual anionic vesicles, there is a large assumption that PI(4,5)P₂ is such a stronger binder that it is only useful to consider the phosphoinositide contribution. All of these methods of analysis allow for unique insights, though by far the fairest test is the

total surface lipid. The drawback is that it likely greatly underestimates the “true” rate of association. After careful analysis using all of these methods for the analytical section, we thought it prudent to limit the global fit to the total surface lipid contribution.

This careful analysis at first revealed how little the surface potential effects the rate of binding. Above a total valence charge of (-14), the rates saturate. Even at the highest possible potential of 98% anionic lipid the value is within the statistical limits of 30% anionic lipid. If there is no difference in the association between these two experiments, it is not surprising that there is no effect when there is a nano-sized domain of binding lipids. Speculation what causes this phenomenon can be explored through the Gouy-Champman-Stern theory⁵⁶⁻⁵⁸.

Gouy-Chapman-Stern theory predicts that when the surface potential, $\psi(0)$, is small, it is related to the surface charge density, σ , and the Debye length, κ^{-1} :

$$\psi(0) = \frac{\sigma}{\epsilon_a \epsilon_0 \kappa}, \quad \text{Eq 4.}$$

moreover, the potential varies with distance from the charged surface:

$$\psi(x) = \psi(0)e^{-\kappa x} \quad \text{Eq 5.}$$

Qualitatively, this theory states the charged surface will attract counterions, repel co-ions and produce an anionic environment within the charged surface’s proximity⁵⁶⁻⁵⁸. Importantly we are working in an electrolyte solution, 150mM. This decreases the potential from the fixed charges on the surface, i.e., negatively charged lipids, and the protein. This translates to a change in Debye length. It has been calculated that in the absence of an electrolyte the magnitude of the potential is 25mV at 1.5 nm from the surface. This decreases to 0.7nm in 100 mM of monovalent salt⁵⁶⁻⁵⁸.

Another unusual quality of charged surfaces is that changes in salt concentration in the bulk solution does not affect the concentration of ions in the double layer. Increasing the salt concentration only contracts the Debye length of the double layer. This has a two-fold effect on our system if we force it to this simple model. (1) There is an upper limit to how many charged PTEN molecules can accumulate in the double layer before the initial interaction. This results in a protein crowding effect. (2) As PTEN binds, it slowly neutralizes the vesicle decreasing the surface potential as PTEN moves from the aqueous layer and becomes a part of the charged surface. This effectively increases the Debye length during the reaction making a larger capacitive gap in which the enzyme has to jump to interact with the surface. (3) There may be a maximum anionic lipid composition for a given salt concentration where a closer Debye length gives no additive benefit. In a simple example with and without an electrolyte, the Debye length decreases by an estimated 0.3 nm. The electrostatics of our systems are more complicated than the theory above, we have multivalent lipids in some of our vesicle mixtures, and PTEN is clearly not a point charge. Nevertheless, even in the simplest models, the changes in potential as an effect of surface charge decreases as the surface charge increases in 100mM salt. All of this together supports our results where after a certain surface concentration of charge is reached, the benefits of increasing the charge further decreases as a route to drive the protein to the membrane.

The second major result from these data is the special role that PI(4,5)P₂ plays in PTEN-vesicle interaction. It has been well established that PI(4,5)P₂ is necessary for the activation of PTEN to turn over PI(3,4,5)P₃. Later it was found that when PTEN binds to PI(4,5)P₂ a conformational change is triggered^{8, 11, 36}. When the studies first began we

thought we might be able to see this conformation change in the tryptophan fluorescence. When binding there is a shift of the emission peak to longer wavelengths, 320nm → 335nm. Unfortunately, the system is too noisy to distinguish if there is a change in the kinetic experiments from the raw data alone. When fitting each curve individually in the analytical method, they fit very well to eq2. Therefore, we concluded that we could not follow the conformation change.

Global fitting was necessary to find this nuanced difference. When trying to fit all the substrate concentration dependent curves simultaneously, it became immediately apparent that the kinetics were more complex than the simple model could account for. This increased complexity manifested itself only in the PI(4,5)P₂ containing vesicle systems. There are two possible explanations for the second rate constant we observe in the PI(4,5)P₂ containing vesicles: First, we may be able to observe the conformational change of the protein, leading to a change of the Trp emission maximum due to the changed environment and hence an altered FRET transfer efficiency. A second possible explanation for this second rate constant is that the protein binds initially weakly electrostatically which is followed by the binding to PI(4,5)P₂.

The comparison between the analytical methods and the global fit methods gives us confidence in our results. For all the data, except 5% PI(4,5)P₂, the trends of the $K_{d\text{overall}}$ and $K_{d\text{Total Lipid}}$ agree with each other. 5% PI(4,5)P₂ in the global fit work shows a stronger binding constant, yet K_{d1} is comparable to $K_{d\text{Total Lipid}}$. Previously in this lab, reported thermodynamic K_d values also show a larger value than the kinetics (Table 3), highlighting the difference between the experiments. Nevertheless, the observed binding trends strongly support each other. This may indicate that thermodynamically, most of the

PTEN population when interacting with a 5% PI(4,5)P₂ containing vesicle, may do so electrostatically and only a small portion makes a successful second step to the more strongly bound complex.

These results highlight how important it is for this bimodal protein to have access to both the phosphoinositide and the monovalent lipids. It is the stability of the complex that drives this interaction, which is determined both by the electrostatic potential of the vesicle and the phosphoinositide triggered conformational change of the protein.

This leaves us with some interesting questions. How does such a weak first step in binding effectively compete with all the activity at the membrane surface? Once the protein is bound is there then an effect on its lipid surface search algorithm whether there are clustered lipids or not? What does this mean for other peripheral, plasma membrane, surface binding proteins? For example, myotubularin is also a 3-phosphoinositide phosphatase which dephosphorylates PI(3,5)P₂ to make PI(5)P and triggers the formation of an activated myotubularin complex¹¹. Does this phosphatase “dance” along the membrane similarly to what we observe for PTEN?

Chapter 3: Single Molecule Study of PTEN lipid interaction

After establishing that PTEN's membrane interaction is determined more by the stability of binding than by the association step, it is natural to investigate the dynamics of the lipid bilayer bound protein. **In the stated hypothesis above, PTEN uses its multiple lipid binding domains synergistically to interact with lipid membranes and efficiently localize to its substrate.** In this part of the project, individual molecules of PTEN interacting with solid supported lipid bilayers (SLBs) are tracked to determine how the different PTEN domains interact with model membranes of various compositions. The protein purification and the TIRF data were acquired by Rakesh Harischandra. I adopted the project after he completed his time in the group and used the developed Mathematica program to filter and analyze the data. The data analysis was based on a program that Dr. Jeff Knight at the College of Liberal Arts and Sciences at the University of Colorado Denver developed a few years back^{59, 60}. We wrote this program based off an exemplary code from Knight and designed it for our work, and its method is outlined below. Single-molecule total internal reflectance fluorescence (smTIRF) microscopy was used to determine the diffusion constants and dwell times of PTEN constructs and compared to the behavior of the wild-type protein. The desired outcome is an understanding of how each part of the protein works together to result in a synergistic PTEN/lipid interaction.

Single-molecule tracking of biological events results in data without the time and population averaging.^{61, 62} This allows for the investigation of the stochastic behavior of individual enzymes in the system, unveiling a nuanced picture which with more traditional methods would have been averaged out. The reality of cellular systems is that at the scale of the biochemical reaction the phenomena are stochastic. A recent paper has

estimated in yeast systems the total abundance of proteins to be between 1,000 – 10,000 molecules.⁶³ This is precisely the level of particles examined in smTIRF microscopy experiments. In this section, two types of single molecule analyses are reported, the diffusion of PTEN on model membranes and the single-molecule dissociation rates of the protein.

Diffusion constants will inform us how many lipids the protein and its domains strongly interact with. Knight et al⁵⁹ have found that the diffusion of peripheral membrane proteins is a function of the number lipids the protein is bound to. The dwell time of the protein on the SLB are the inverse of the dissociation constant. A comparison of these data to the stopped-flow experiments described above is an independent method to check on our ensemble data. With the combination of ensemble data and the single molecule data, we hope to present a descriptive picture of how PTEN interacts with biomembranes.

3.1 Methodology

Supported Lipid Bilayers.

For the single-molecule experiments, the supported lipid bilayers were developed as follows. SUVs in a 50 mM KCl, 20 mM Citrate buffer (pH 3.5) were mixed with 1 M NaCl citrate buffer and flowed over the glass support. The glass support was prepared by first cleaning it in a piranha solution. These slides were then stored in HPLC water until ready for use. When needed the slide was dried with a stream of nitrogen and then cleaned with an oxygen plasma (2min). At this point, the slide is exposed to the SUV mixture and allowed to incubate for 30min. The slides were then washed with 20 mL of HPLC water followed by 20 mL of physiological buffer. To ensure that no bilayer defects are affecting the outcome of the single molecule experiments, holes in the lipid bilayer

were filled by flowing 100 µg/mL of BSA through the system^{8, 64}. All of this work was done on a TIRF microscope slide in a gasket (CoverWell perfusion chamber) purchased from Molecular Probes (Eugene, OR, USA). The CoverWell perfusion chamber gasket was placed on the TIRF microscope slide immediately after plasma cleaning. They are 19 mm X 6mm X 0.5mm and proved to be an easy method to flush the membranes with various buffers and protein solutions as well as to keep the SLB hydrated. For a more thorough discussion on the current mechanism of SLB formation see in the methods section for the microfluidic experiment (next chapter).

Sfp phosphopantetheinyl transferase method.

To label PTEN and the domain constructs, we followed a protocol outlined by Yin, J. et. al.⁶⁵. In brief, the method takes advantage of Sfp phosphopantetheinyl transferase to attach AlexaFlour probes to a short 11-residue peptide tag (ybbR). The ybbR tag has the peptide sequence DSLEFIASKLA which is fused to the C-terminal end of PTEN or its domains⁶⁵. Sfp phosphopantetheinyl transferase covalently attaches 4'-phosphopantetheinyl groups from CoA to the underlined serine of the ybbR sequence. The enzyme is tolerant of small molecules attached to CoA making it a convenient pathway to label proteins with small molecules.

In this work, the fluorophore-CoA conjugates are synthesized by a one-step Michael reaction of the maleimide-functionalized AlexaFlour 647 (Thermo Fisher Scientific, Waltham, MA) and the free thiol group of CoA resulting in a thioether linkage between the two. To a solution of the AlexaFlour probe in 0.25 mL DMSO (starting concentration 5.6 mM) add 0.75 mL of CoA trilithium salt (starting concentration 2.8 mM) dissolved in buffer (buffer: sodium phosphate 100 mM, pH 7.0). The reaction mixture is

stirred in the dark at room temperature for an hour. To a total volume of a 100 μL of buffer (10 mM MgCl_2 , 50 mM HEPES pH 7.5) 0.1 μM Sfp, 5 μM AlexaFluor-CoA, and 5 μM of the ybbR construct are added (all final concentrations). The reaction mixture was allowed to incubate for 30min in the dark. The labeled protein was separated from the free dye by PD MiniTrap G-25 column (GE, Pittsburgh, PA) and the concentration was determined by measuring the absorbance at 647nm (CY5 option) using a NanoDrop spectrophotometer (ThermoFisher Scientific, Waltham, MA)⁶⁴.

TIRF Microscopy

Total internal reflection fluorescence (TIRF) microscopy is a technique which enhances the contrast of the images. This is achieved by angling the excitation laser so that the impinging beam has an incidence angle greater than the critical angle of the quartz slide. This results in total internal reflection within the coverslip and the formation of an evanescent wave which excites the fluorophores. The decay of the evanescent wave is rapid, meaning only a small depth of the sample is excited at one time (~100 nm). This reduces the number of fluorophores that are excited outside of the focal plane and thus results in a very high signal-to-noise ratio of the fluorescence signal⁸. Since TIRF microscopy only images labeled molecules close to the coverslip, it is particularly useful to probe molecules that reside at or near the plasma membrane (cells) or lipid bilayers (model systems).

smTIRF microscopy is incredibly useful in single-molecule studies, especially when investigating processes at interfaces such as the plasma membrane of cells or on supported lipid bilayers. In these studies, protein and lipid dynamics are tracked both in time and space, and the behavior of individual particles are collected. In addition to the

kinetic information, these data can also impart structural information about the interface and how the protein manages complex membranes. This is realized in the cases where the movement of proteins at the interface deviate from Brownian motion. This can indicate obstructions or corralling of the protein as seen by a loss of linearity in the MSD-Time graphs used to determine diffusion constants.

The fluorescence images were obtained with a Nikon (Minato, Tokyo, Japan) Eclipse Ti inverted microscope with a TIRF Illuminator. For excitation sources, coherent 488 nm and 647 nm sapphire lasers were used. Images were captured with an Andor 3iXon CCD camera (Belfast, UK). A Nikon 100 X CFI Apo TIRF oil objective with a 1.49 numerical aperture was used for TIRF imaging. The 488 nm TIRF filter cube and Sedat Quad cube and Cy5 emission filter were purchased from Chroma (Foothill Ranch, Ca).

Fiji and Mathematica Data Analysis

We use Fiji⁶⁶ to do the initial image processing. For particle tracking, we took advantage of the plugin Mosaic.^{67, 68} Here we define three criteria for particle tracking; particle pixel radius (4 pixels), intensity percentage (20%) and nonparticle discrimination score (NpScore) (0). The pixel radius of 4 was chosen since it is just big enough to encompass the 2D Gaussian profile of the particle (Figure 26). Too small, false detections are included in the particle selection, too big then the circumferences overlap. This overlap becomes an issue in the particle linking stage as the program builds the tracks. The program may mistake two particles for one, artificially shortening the trajectories. For these reasons, and with careful inspection a radius of 4 was chosen.

Next, the expected brightness for the particles were selected. This spanned the upper 5%-20% of the intensity range of the image. This, like the radius was determined

by careful manual inspection to ensure white noise was not included in the selection as well as good particles not being missed. Finally, the NpScore was set to 0. This parameter is a cut off filter. By setting the value to 0 we included all NpScores in the data set. The NpScore system, determines the likeliness of a detection being a particle. It is used later in the Mathematica analysis.

After particle selection, we defined the parameters for particle linking to create the trajectories. The first parameter is how many frames should the algorithm link through if the particle blinks off. This was set to 2. The second is how far the particle can move in

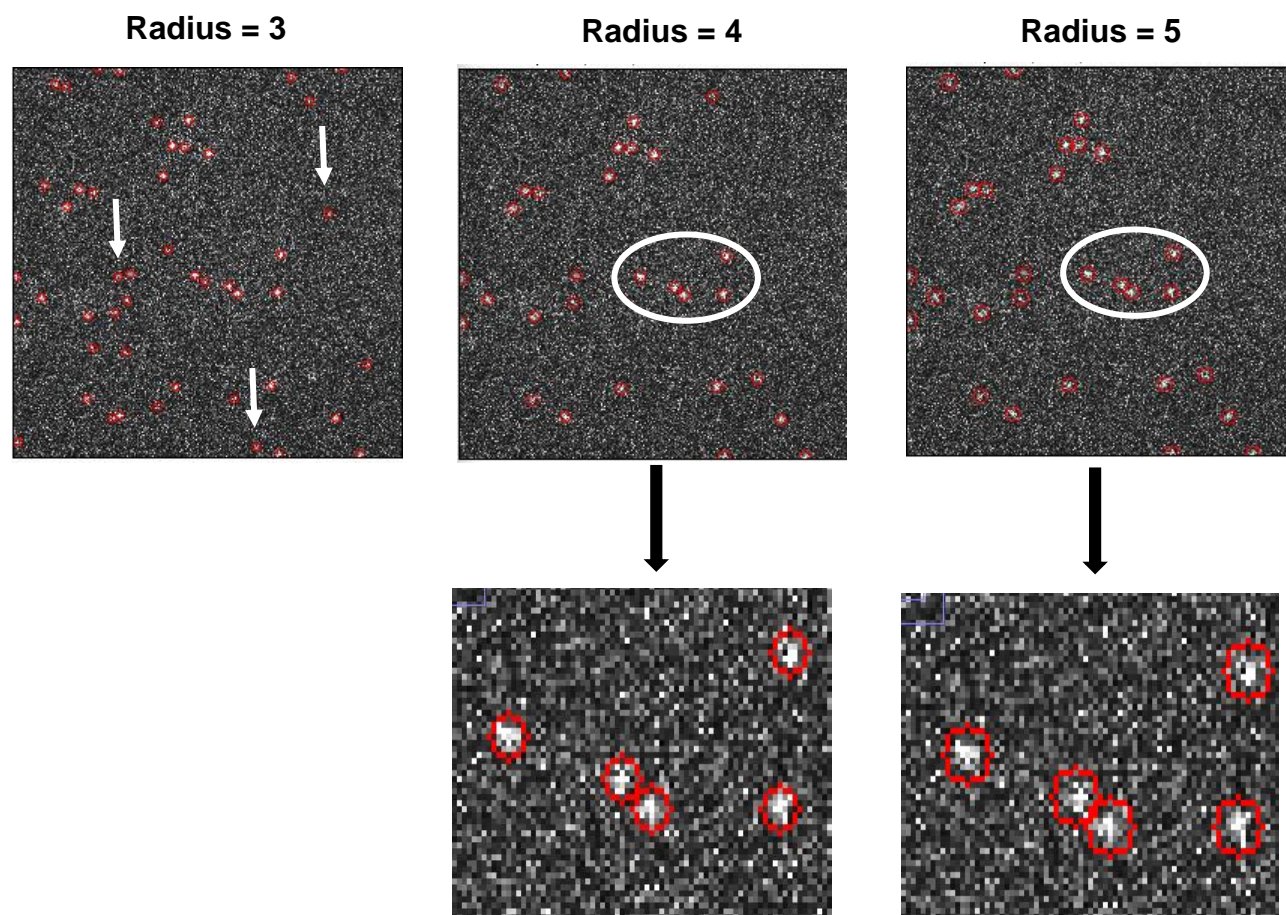


Figure 26. Selection of the radius in the Mosaic plugin is an important step in determining real particles from spurious detections. A radius of 3 is too small and many false positives are included (white arrows). The radius 5 is too big, the red circumferences are starting to overlap for two neighboring particles. They are in danger of being encompassed by a single selection. A radius of 4 is just big enough to outline the 2D Gaussian profile of the particles.

two succeeding frames, this was set to 5 pixels. With a 100X objective 5 pixels cover 0.8 μm . A high diffusion coefficient for a lipid is 4 $\mu\text{m}^2/\text{s}$ or 0.49 μm in 60 ms. We purposely overestimate the distance traveled because PTEN is a weak binder. It is likely that the protein can micro-dissociate from the membrane and re-bind quickly. To account for this phenomenon we used an increased area for which the particle could move and validated it with manual inspection after linking. This method as described above was set to intentionally oversample. Strict filtering rules are applied to the data in a program developed in the Mathematica software before the final analysis.

In the Mathematica program, we run the data through a series of exclusion tests. The first test filters tracks by the non-particle discrimination score (NpScore) (Figure 27). It is a value given to each particle through the mosaic software which determines “true” particles from spurious detections⁶⁹. In the Mathematica program, we find the track NpScore by finding the mean NpScore of all the particle steps in each track. This track

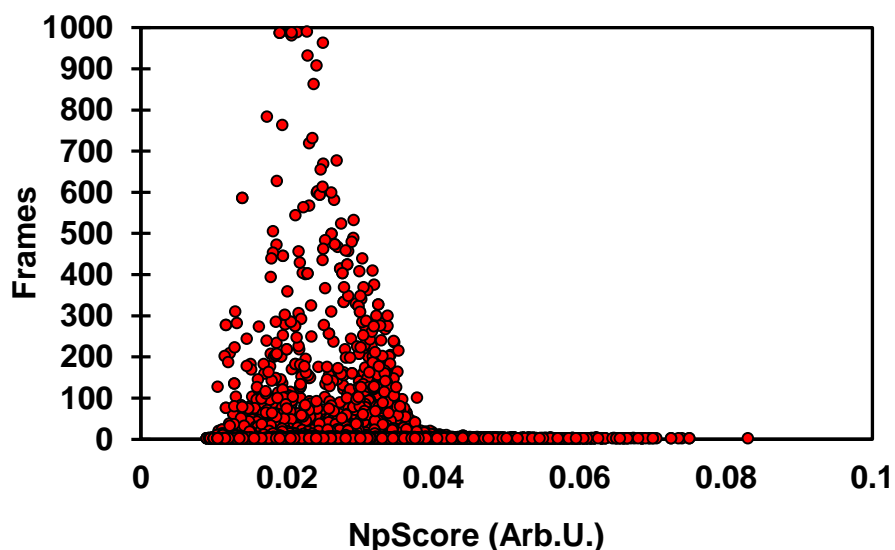


Figure 27. The distribution of of the track NpScore plotted against frames. The track NpScore is calculated by finding the mean NpScore of the steps within a track. By plotting against the frame number, we can tell how long the track exists for a given track NpScore. This graph illustrates that a NpScore above 0.04 does not last for many frames, and likely to be made up of many “bad” particle selections.

NpScore is plotted for each track and plotted as a distribution. A filter is set at the min and max of this distribution to bracket around the trajectories that we want to keep. These data are then further filtered to exclude any tracks shorter than three frames (this will change with the exposure time, which ranges between 30ms – 50ms).

The next filter is designed to exclude spurious detections (dim, short measurements) and contaminates (bright, long-lasting particles) by plotting the averaged particle intensity of a track against time (frames) (Figure 28). The filter is set to exclude these tracks. In the example below the filter is set to 3.5 and 9 to accomplish this. Despite this filter there are still an unacceptable number of immobile particles among the longer trajectories. To exclude these a final diffusion filter is applied.

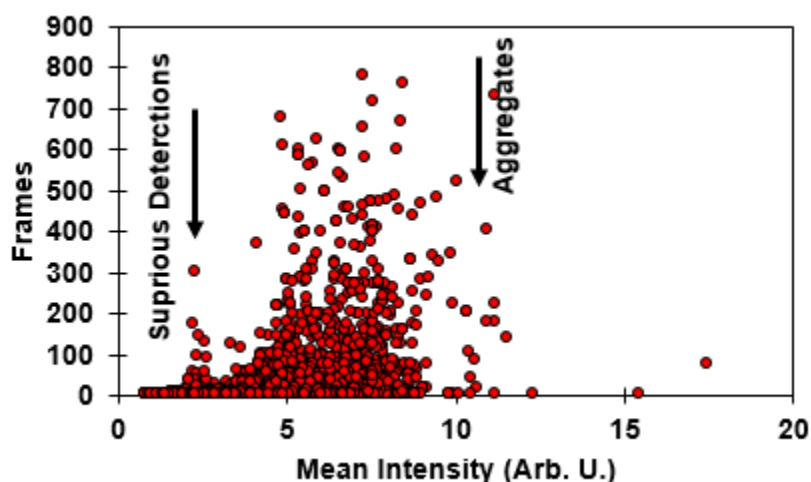


Figure 28. The intensity filter plots the mean intensity of the trajectory against how many frames the tracked particle exists for. The result is the short, dim tracks cluster to the left of the graph while long, bright particles cluster to the right. The short, dim particles arise from spurious detections and should be excluded from the data analysis. There are also some trajectories on the left in this example that exist for a long time. This is due to particles being on the perimeter of the image, on the edge of the 2D gaussian excitation beam. Being close to the perimeter and outside of the center of the excitation source also mean that these tracks are poor candidates for particle tracking. The long, bright particles arise from aggregates and should be excluded as well.

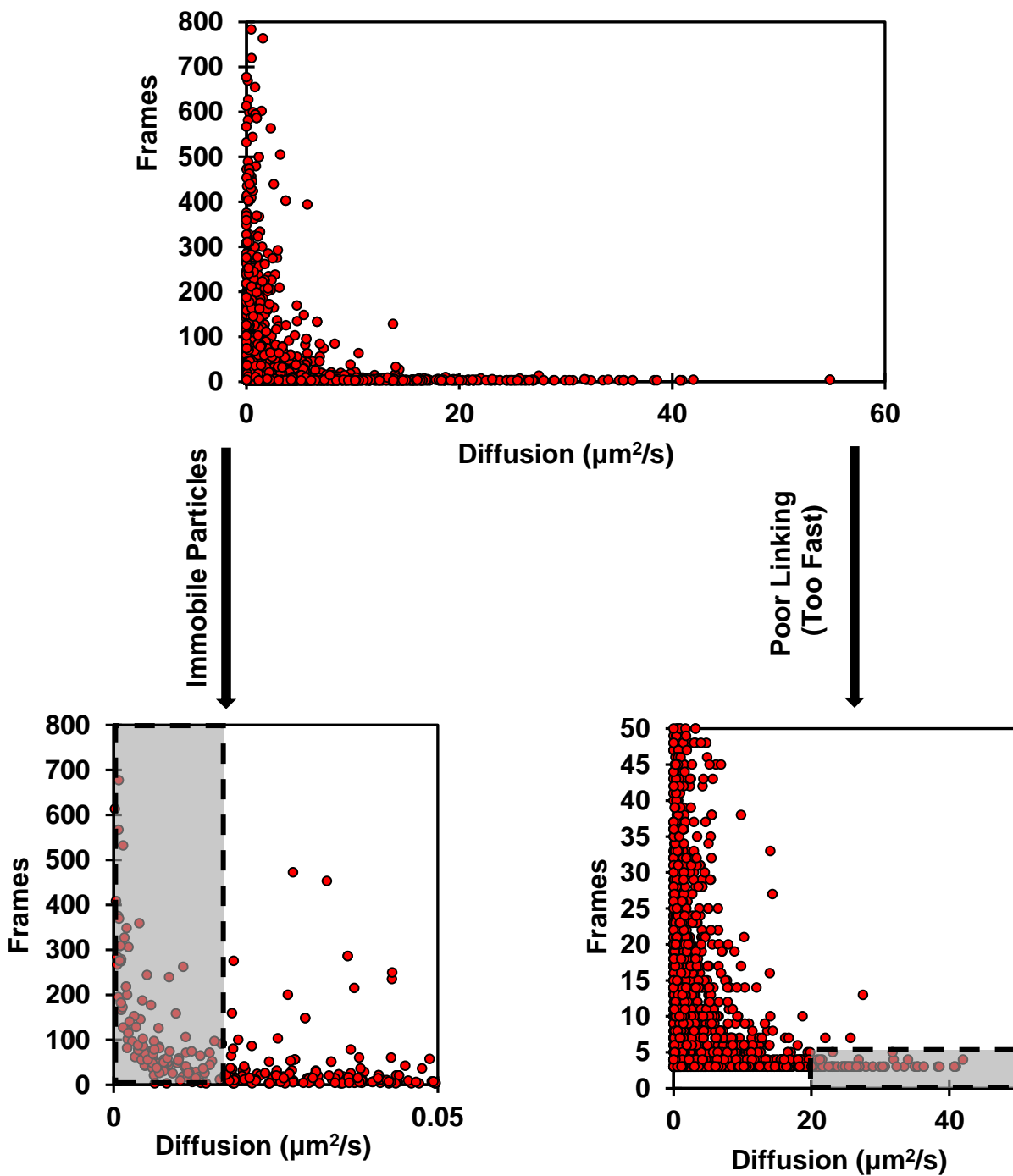


Figure 29. The diffusion filter is the final exclusion test placed upon the data set. The diffusion is calculated for each tack and plotted against the number of frames with which the trajectory exists for. Immobile particles are found on the left side of the distribution. They swing up, composed of slow diffusions that exists for many frames (grey box). In addition, there are several fast diffusions that escape the earlier exclusion tests (right side of the graph). These are also eliminated from the data set.

The diffusion filter plots the diffusion against the number of frames the track exists for (Figure 29). It is mainly to exclude immobile particles, which are clustered on the left side of the plot (approximately $< 0.03 \mu\text{m}^2/\text{s}$). In addition, there are a several tracks on the right of the distribution that are too fast. The selection for the fast diffusion is made when the right tail of the distribution drops below five frames. The remaining data is used to determine the diffusion coefficients and dwell times. Each data set had to have a least 1000 trajectories pass the various filtering modes before being used. This was achieved by compiling multiple movies taken on a single experimental day (5-8 movies for one trial). All error bars in the data presented are from three independent experiments, (i.e., different days, independent protein and SLB preparations).

Dwell Time Filtering and Analysis

The dwell times for the PTEN interaction with different membranes were collected, and their cumulative distribution examined. By plotting the cumulative distribution the effects of binning errors are reduced since the cumulative result is independent of the bin size. In addition, the cumulative distribution is also useful for estimating the number of rate constants. The y-axis is the sum of all the events that has a dwell-time between zero and the associated time. Normalized, the cumulative distribution gives the probability that a dwell time falls below a given value.

The dwell time binning starts after the first three frames of the movie. The bin width is set to be 3X the exposure time (i.e., if the exposure time is 30 ms the bins are at 90ms intervals) and accumulated out to 5 seconds. We chose to plot the dwell times as a fraction of the total cumulative dwell time population. To ensure that the dwell times are not artificially shorted, the data was passed through a few filters. The first is that any track

that starts on the first frame or ends on the last is removed. Also, if a track comes within 6 pixels of the image perimeter, it is also excluded from the dataset.

3.2 Diffusion of PTEN on SLB

To continue the exploration of the dynamics of PTEN on model membranes we tracked single PTEN molecules on the various SLBs using smTIRF microscopy. Figure 30 shows a snapshot from a movie of wtPTEN on a SLB composed of 3%PI(4,5)P₂, 30%DOPS, 67%DOPC and 10ppb Rhodamine-PE. Before acquiring the movies (Figure 30), the frame area was subjected to a high-intensity laser excitation to bleach any aggregates or fluorescent contamination. The laser was turned off, and the SLB was allowed to recover for three minutes. After this rest period, the movies were acquired for data analysis. Particles were selected and linked using the Mosaic plugin in Fiji as described in the methods section. The acquired trajectories were filtered and analyzed in

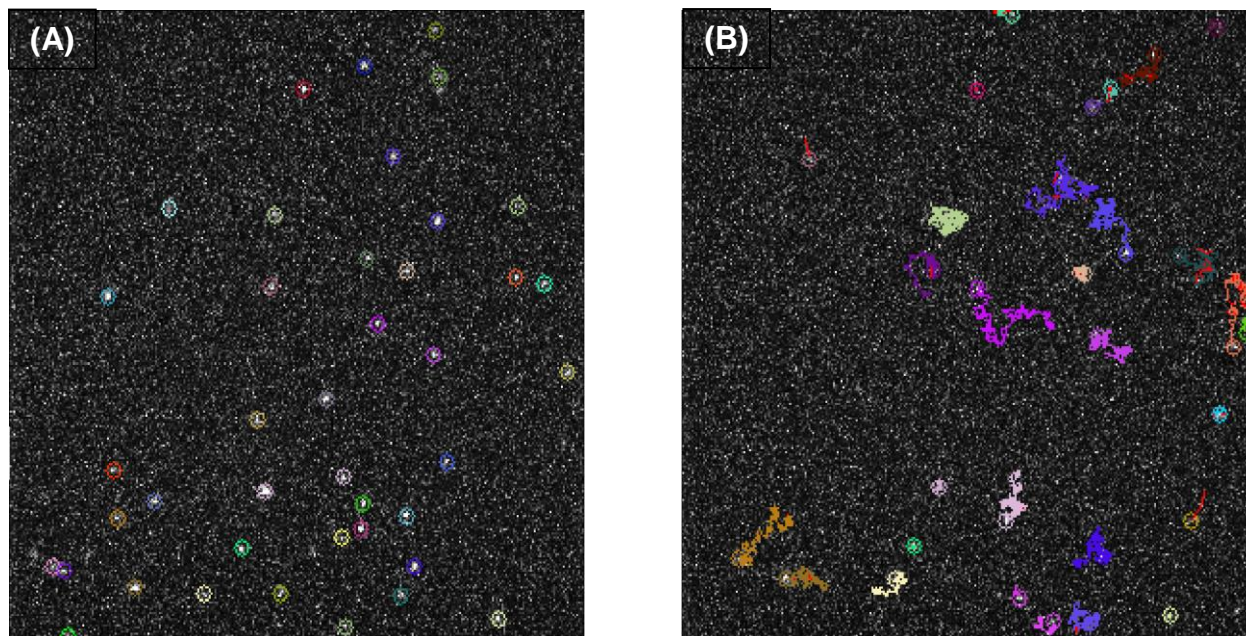


Figure 30. Particle tracking of wtPTEN interacting with PI(4,5)P₂/DOPS/DOPC solid supported lipid bilayers. (A) Particles are determined in the mosaic plugin by criteria selected by the user. These are the radius of the particle, its intensity and non-particle discrimination score (B) The tracked particles after 6.6s. To make the trajectories, the particles are linked between subsequent frames. This is determined by searching for the nearest neighbor within a defined distance. In this work, it was five pixels.

the Mathematica program. Using the filtered data, the diffusion coefficients of the protein and the PTEN domain constructs were determined by a two-step process. First, to determine the mean squared displacement (MSD), the probability of finding the protein is plotted against increasing step sizes (Figure 31). This is done for each time interval for a total of 10 intervals. A time interval is dependent on the exposure length, so in the case of a 30 ms exposure, the time interval step would be 30 ms, 60 ms, 90 ms, etc. Figure 31 illustrates one of these population distribution curves plotted against the step size for the 90 ms time interval. It plots the percentage of PTEN that travels the distance r^2 (μm) in 90 ms. This population data is divided between 100 bins and plotted on a log scale. By plotting the data on a log scale, we can test whether the dependence is single or multi-exponential^{60, 64 70}. Having a multi-exponential fit indicates that there are multiple populations of molecules on the surface. The PTEN population data fit to the double

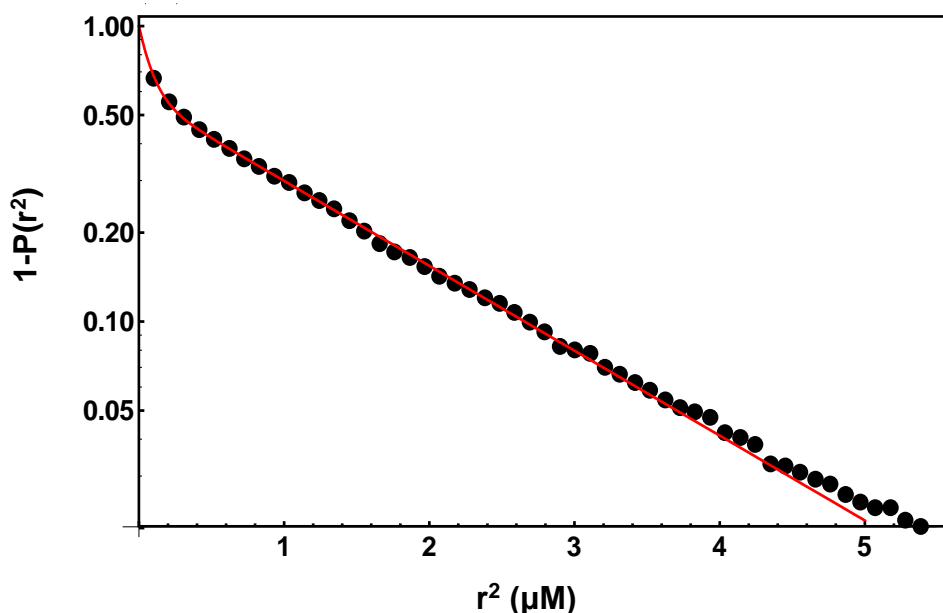


Figure 31. The PTEN population as a function of displacement after 90ms. The data is fit to equation 7. The MSD of the fit are collected. This data fitting is repeated for at least ten time points.

exponential function with the form^{59, 60, 64, 70}:

$$1 - P(r^2) = Ae^{-x/MSD1} + (1 - A)e^{-x/MSD2} \quad \text{Eq.6}$$

where (A) is the population of tracks with the resulting mean square displacement (MSD). (MSD1) and (MSD2) are the mean squared displacements for population 1 and population 2 respectively. The MSD of the protein is determined for at least ten frames (time intervals).

This collection of data is used in step two. In step two, the MSD data is plotted against the time interval it was gathered at to build velocity graphs (Figure 32). The data fitting to two exponentials indicates at least two PTEN populations are existing on the SLB. In Figure 32 the respective populations are split into a fast diffusion and a slow diffusion group. The linear fit to determine the diffusion coefficient is^{59, 60, 64, 70}:

$$r^2 = 4Dt + C \quad \text{Eq. 7}$$

where (D) is the diffusion coefficient, and (c) is a constant. Whether the data fits to line or not, is informative. If the results are non-linear it can indicate anomalous diffusion either from corraling of the protein or directed diffusion (vesicles moving along cellular structures). Within the time range we looked, the data were linear, meaning they moved with Brownian motion, or simple diffusion.

Figure 33 illustrates the difference between the two populations from Figure 32. The graph shows how far the respective populations of PTEN traveled in one second on the PI(4,5)P₂/PS/PC SLBs. It the fast diffusion shows a protein that is able to explore them membrane environment. The slow diffusion sample shows a protein that is dedicated

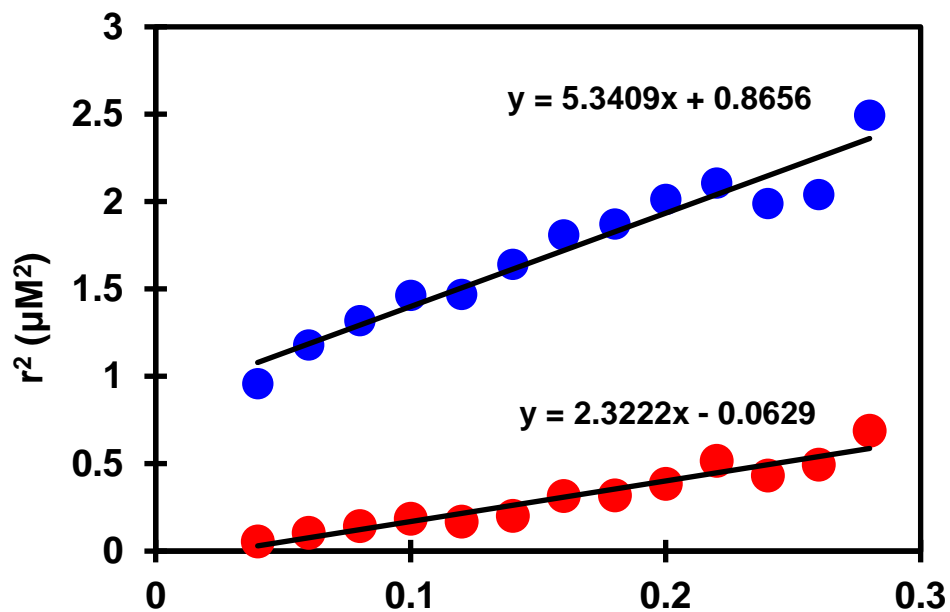


Figure 32. Velocity graphs of wtPTEN interacting with 3% PI(4,5)P₂/ 30%DOPS/ 70%DOPC SLBs. The single molecule diffusion data resulted in two groups, both of which can be fit to equation 8.

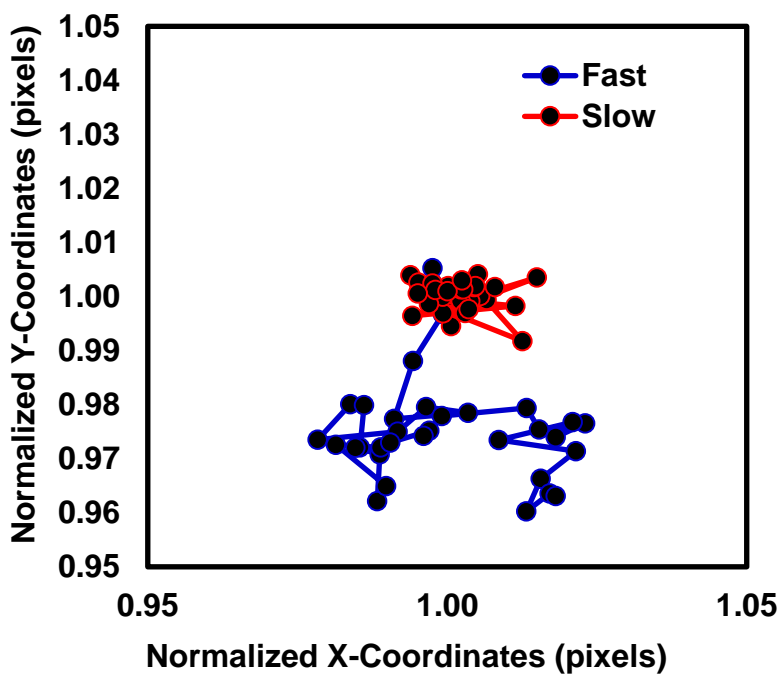


Figure 33. Example tracks determined from the diffusion coefficients from the previous figure. These normalized tracks show the displacement of the fast PTEN vs. the slow PTEN after one second.

to a particular membrane region. We wanted to explore in this section, how the behavior of PTEN on different SLBs change. In addition, we followed the diffusion of PTEN constructs on these model membranes too. We wanted to see, if we could define which domains were responsible for strong interactions with the membrane vs. weak. The protein constructs tested were delPTEN (PTEN₁₆₋₄₀₃, i.e., without the PBD domain) and the PTEN C2 domain (PTEN₁₈₆₋₃₆₂). The resulting diffusion constants and populations making them up have been collected and presented below.

Figure 34 shows the diffusion coefficients of wtPTEN on 30% PS/ 3% PI(4,5)P₂/ 67% PC, 3% PI(4,5)P₂/ 97% PC, and 30% PS/ 70% PC bilayers. The diffusion coefficient of the lipids was found to be 2.40 $\mu\text{m}^2/\text{s}$ (90% of the total lipid population) which is what was expected for a fluid lipid bilayer^{59, 60, 64, 70}. As stated previously, there are two PTEN diffusion populations. When tracking wtPTEN on membranes the major PTEN population has equivalent diffusion coefficients at $\sim 1.0 \mu\text{m}^2/\text{s}$. The effect of different membrane compositions on PTEN dynamics becomes apparent when examining the slower (minor population) component. As expected, the diffusion coefficient increases from the 0.13 $\mu\text{m}^2/\text{s}$ with PI(4,5)P₂/PS membranes to 0.50 $\mu\text{m}^2/\text{s}$ with PS only membranes.

Figure 35 shows the population split of these diffusion coefficients on these membranes. The population data shows that there is a larger population with a fast diffusion with the PI(4,5)P₂/PS membrane when compared to the other two. The PI(4,5)P₂ and the PS membranes have approximately a 60/40 distribution of fast to slow proteins whereas PI(4,5)P₂/PS has a 75/25 ratio. This result was unexpected. For wtPTEN on PI(4,5)P₂/PS SLB we expected a 3 component fit. MSDs for PI(4,5)P₂, PS, and PI(4,5)P₂/PS. Instead, the data fit to a double exponential. Given that the fast diffusion

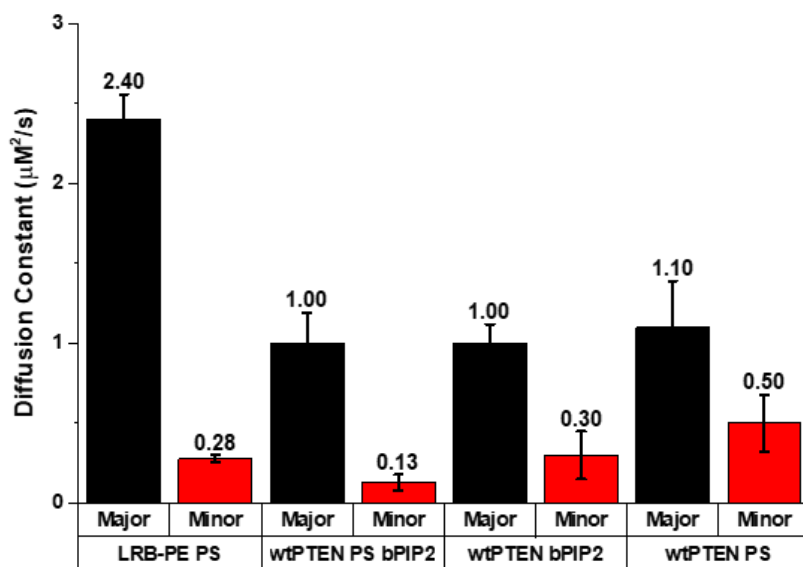


Figure 34. Diffusion coefficients of wtPTEN on various model membranes determined by the analysis described above. There are major, and minor components and the population distribution is outlined below.

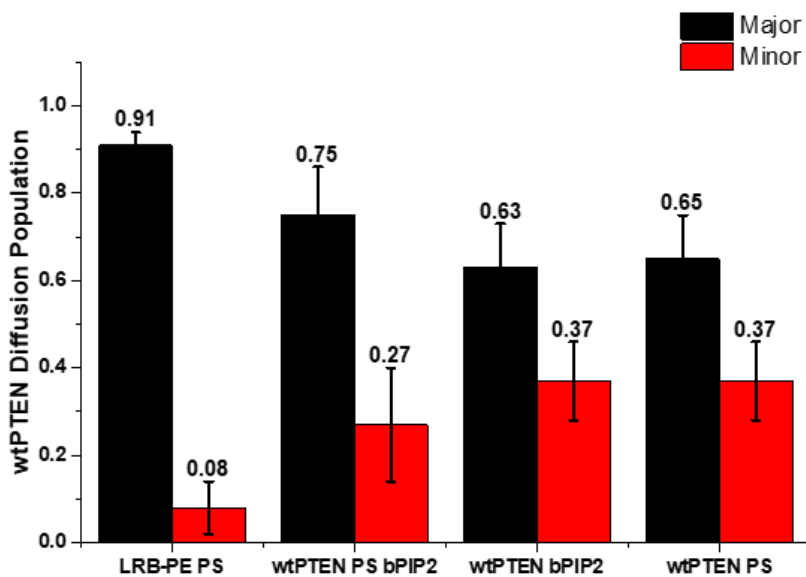


Figure 35. The population of wtPTEN on various model membranes determined by the analysis described above. A large majority of the lipids fall into fast diffusion category and is basically a single population. PTEN has two defined populations.

has such a high population, we hypothesized that wtPTEN-PI(4,5)P₂ and wtPTEN-PS both contribute to it, where the slow diffusion is wtPTEN-PI(4,5)P₂/PS.

Figure 36 and Figure 37 shows a PTEN construct with the PBD domain deleted. The PBD domain has been shown to bind to PI(4,5)P₂ with high specificity. This interaction is necessary for the proper localization of PTEN on plasma membranes and results in a conformational change of PTEN³⁶. The expectation with this construct is that it will make a weaker interaction with the membrane resulting in a faster diffusion coefficient. The fast diffusion rate of delPTEN on the PI(4,5)P₂/PS and PI(4,5)P₂ is the same as for the wtPTEN. While the fast diffusion rate of delPTEN on PS bilayers increased in comparison to wtPTEN. Interestingly, the slow diffusion component remains the same for delPTEN on 30% PS/ 70% PC SLBs. In contrast, the slow component of the delPTEN on PI(4,5)P₂/PS membrane is increased by 6-fold. The slow component of delPTEN with the PI(4,5)P₂ membrane also has the same diffusion coefficient as the

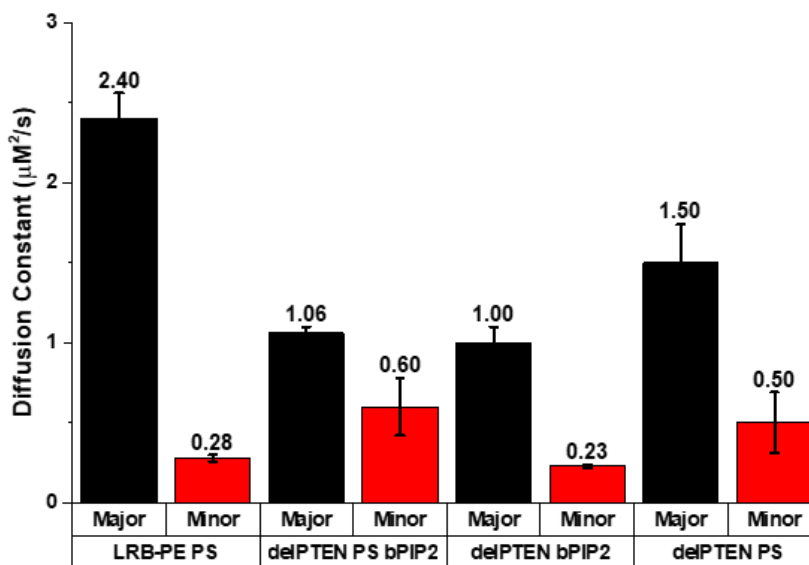


Figure 36. Diffusion of the delPTEN (PBD deleted) construct of various lipid membranes. The fast component of delPTEN 30%PS shows a faster diffusion when compared to wtPTEN. Also, the slow component of 3%PI(4,5)P₂/30%PS has an increased diffusion.

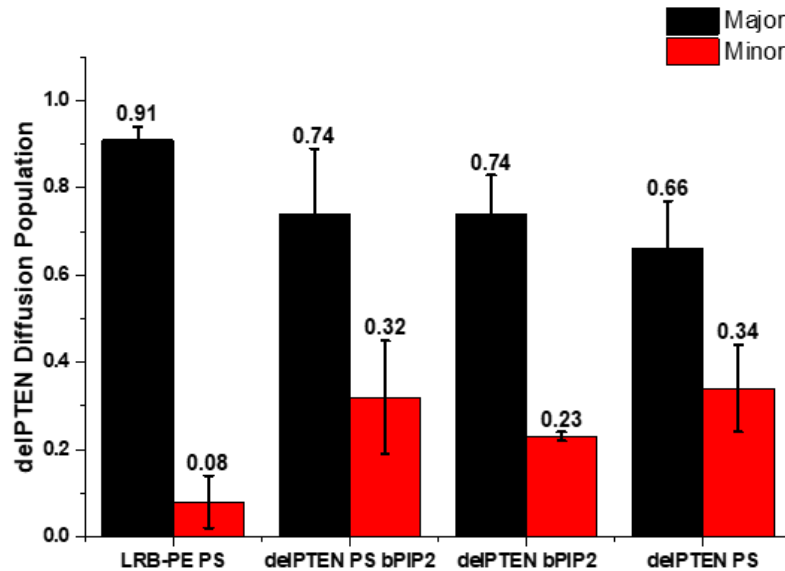


Figure 37. The population of delPTEN on various model membranes determined by the analysis described above. delPTEN on 3% PI(4,5)P₂ membranes distributed to the higher population when compared to wtPTEN data.

wtPTEN. What did change in the PI(4,5)P₂ only system was the population distribution. It shifted from a 60/40 ratio to a 70/30 ratio towards the faster diffusion. Overall, the loss of the PBD domain either resulted in a faster diffusion or a redistribution of the populations to the faster component.

The C2 domain of PTEN has been reported to interact in a Ca²⁺-independent manner with the lipid PS. The interaction, unlike the PBD domain, is nonspecific electrostatic meaning it should show a weak interaction with the membrane. The single molecule results in Figure 38 and 39 show that the C2 domain has the most dramatic difference when compared with wtPTEN experiments. The protein diffusion rate of the fast component for all the membrane systems increased. Also, over 80% of the C2 domain population has shifted for PI(4,5)P₂/PS to the fast diffusion component. The C2 domain on PI(4,5)P₂ membranes has an increased diffusion coefficient in comparison to wtPTEN for the fast component and maintains the shift towards the faster population with

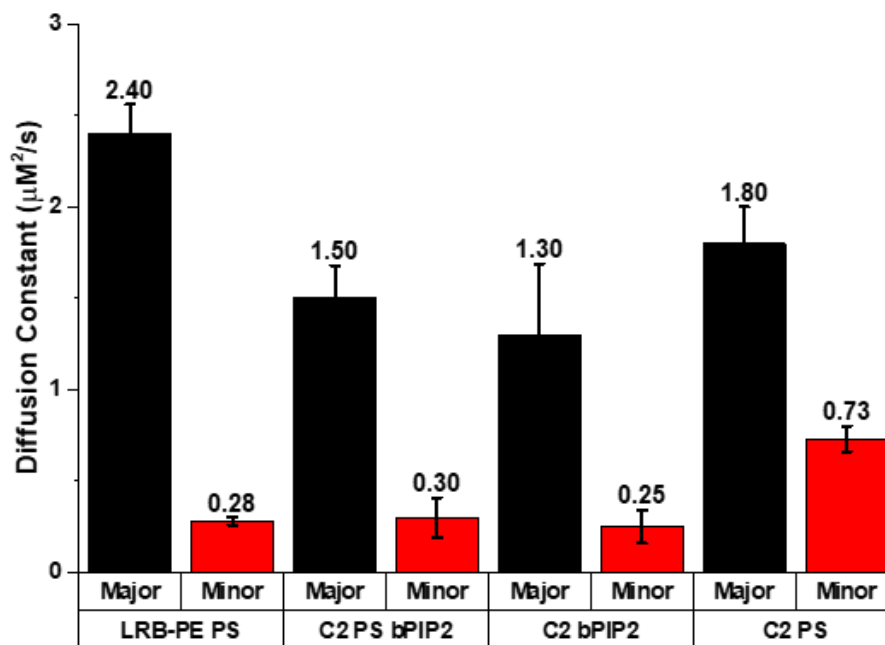


Figure 38. Diffusion of the PTEN C2 domain on various model membranes determined by the analysis described above. All of the fast components display an increase diffusion. The slow component of the PS membrane also has an increased diffusion coefficient.

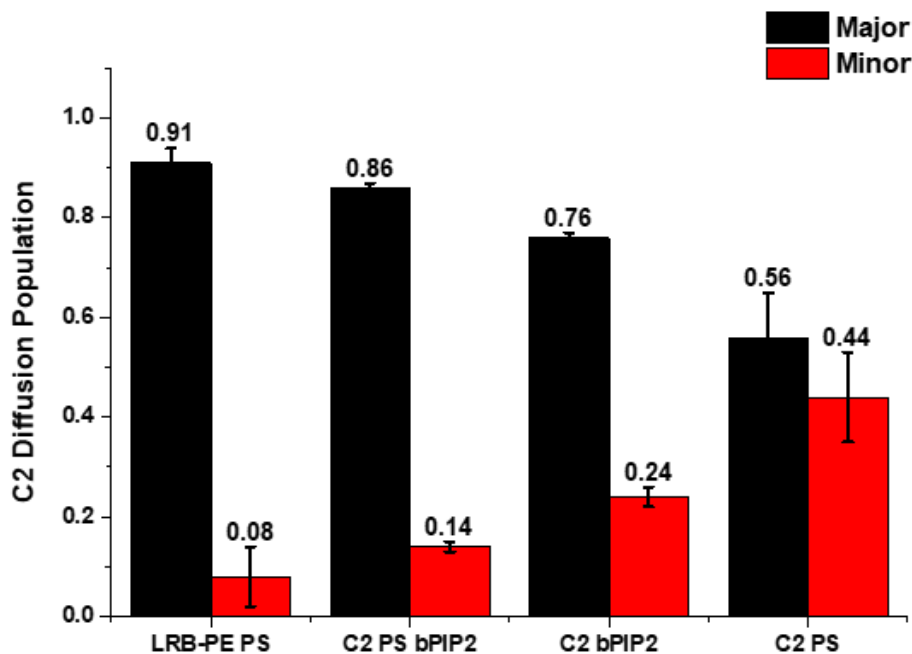


Figure 39. The population of PTEN C2 domain on various model membranes determined by the analysis described above. All three systems show a redistribution of the populations. 3%PI(4,5)P₂/30%PS and 3%PI(4,5)P₂ shift to the faster diffusion, while the C2 domain on the 30%PS is more evenly split between the fast and slow.

75/25 fast/slow ratio. Finally, both the slow and fast diffusion coefficients for C2 domains on PS membranes have a faster diffusion. The difference between the populations decreased slightly but statistically, is still at a 60/40 ratio.

For proteins like PTEN, which bind to the plasma membrane via interactions with lipid headgroups, diffusion coefficients like these tell us how many lipids the protein is interacting with. The relationship, between diffusion and lipid interaction, was uncovered by the Falke group^{59, 60, 64}. They engineered tandem PH domains and determined their diffusion coefficients. The PH domain that they used is well described and known to bind to a single phosphoinositide. By linking, two and three of these domains together with various sized linkers they uncovered this relationship. The diffusion for these types of peripheral binding peptides (like PTEN and PH domains) is dependent only on the lipids the peptide is interacting with, not the size or geometry of the protein. Figure 40 summarizes lipid binding results for these PTEN constructs. Figure 40 highlights that the catalytic domain may be a major contributor in the membrane interaction. This is not usually discussed in the literature. It would be interesting to investigate if there is another specific interaction between PI(4,5)P₂ and this domain. It would also be worthwhile in future work, to see if these data could be discriminated to fit with 3-exponentials, (especially for the 3% PI(4,5)P₂/ 30%PS/ 67%PC). This may deconvolute the results and provide a better picture of what is occurring on these complex surfaces.

3.3 Dwell Times

In addition to the diffusion coefficients, dwell times can be calculated, and their cumulative distribution can be fit to derive a single-molecule k_{off} (Figure 41). Like the diffusion data, population information can also be determined from these single-molecule

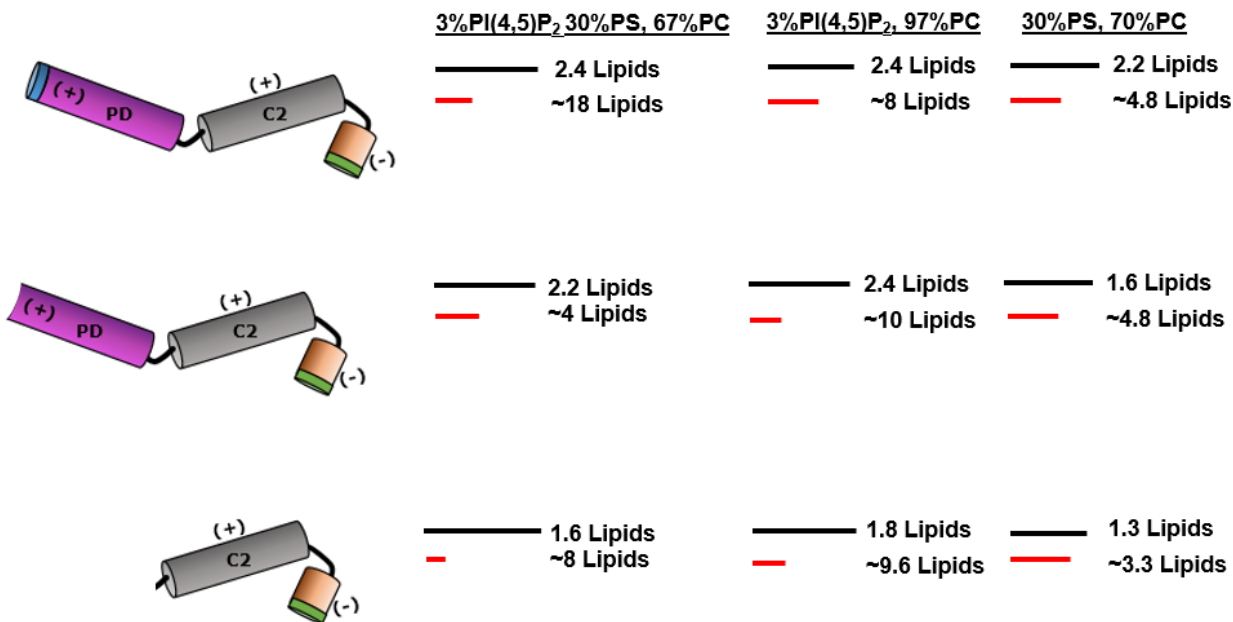


Figure 40. This schematic summarized the diffusion results in terms of bound lipid. The colored lines (Black) and (Red) are representative of the major and minor populations, and are normalized by their length for easy comparison. The tida on the high lipid number is meant as an approximate count, since the relationship between diffusion and lipid number loses linearity after three lipids are bound. This schematic implicates the catalytic domain in the interaction. This particular domain in PTEN us usually over looked we PTEN membrane interactions are described.

fits. The lipid data resulted in a single exponential decay while the protein data had a double exponential result. The cumulative data was normalized to the total dwells and fit to a double exponential with the form^{59, 60, 64, 71-73}:

$$1 - \frac{Dwell_N}{Total\ Dwells} = P e^{T * \tau_{off1}} + (1 - P) e^{T * \tau_{off2}} \quad \text{Eq 8.}$$

where (P) is the population associated with the t_{off} and (t_{off1}) and (t_{off2}) are the rates of dissociation from the supported lipid bilayer. The inverse of these values are the dwell times associated with the protein or its domains on the selected model membranes. The lipid data is representative of the bleaching rate of the fluorophore. As expected it has a single exponential decay. For the protein, the contribution of photobleaching was explored

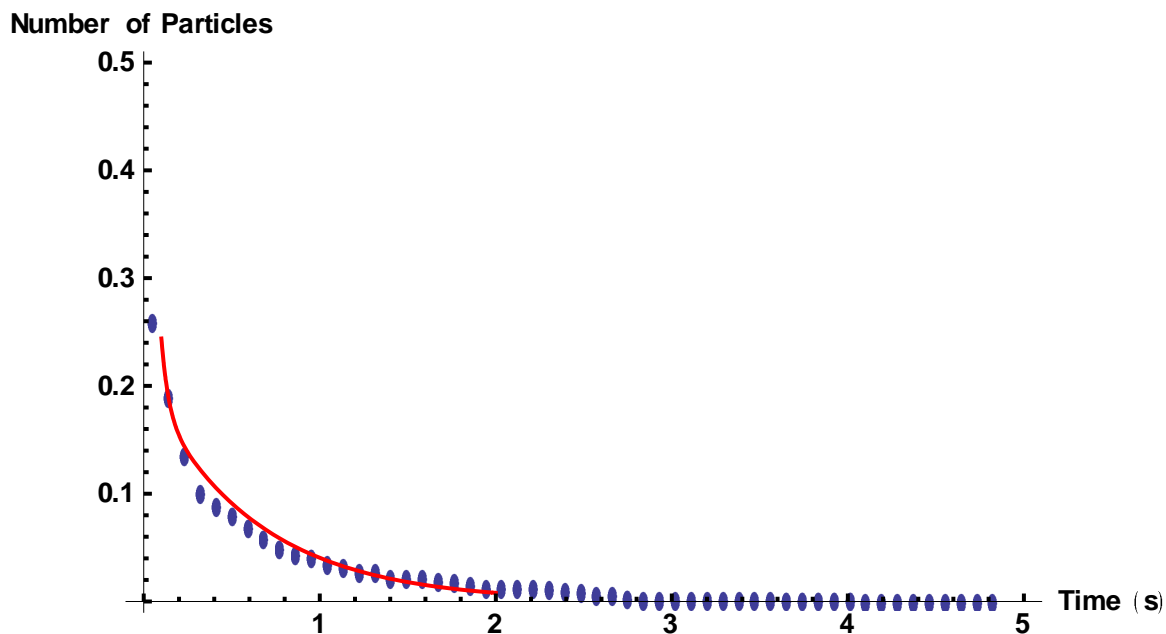


Figure 41. Culmative distribution of dwell times of wtPTEN on 30%PS/3%PI(4,5)P₂. The data is fit to equation 9 and also displays two populations like with the diffusion data. The exception is the lipid data which can be fit to a single exponential.

at two different laser powers. For the AlexaFlour 647, it was found to be a negligible contributor to the rate data⁶⁰.

Figure 42 shows the rates of wtPTEN on 3% PI(4,5)P₂/ 30%PS, 3% PI(4,5)P₂, and 30%PS. The black column is the average of the two rate constants weighted by the particle population distribution from Figure 43. This average resulted in comparable values to the ensemble data obtained from the stopped-flow experiments (Figure 18). The averaged ensemble data for 30% PS and wtPTEN has a k_{off} value of $7 \pm 0.7 \text{ s}^{-1}$ and the single molecule data average is 8 s^{-1} . The similarity of these results is remarkable. The 3% PI(4,5)P₂ and the multicomponent SLB, 3% PI(4,5)P₂/ 30% PS, are difficult to compare since there is no direct comparison to the ensemble work (the PI(4,5)P₂ percent composition is different between the two experiments).

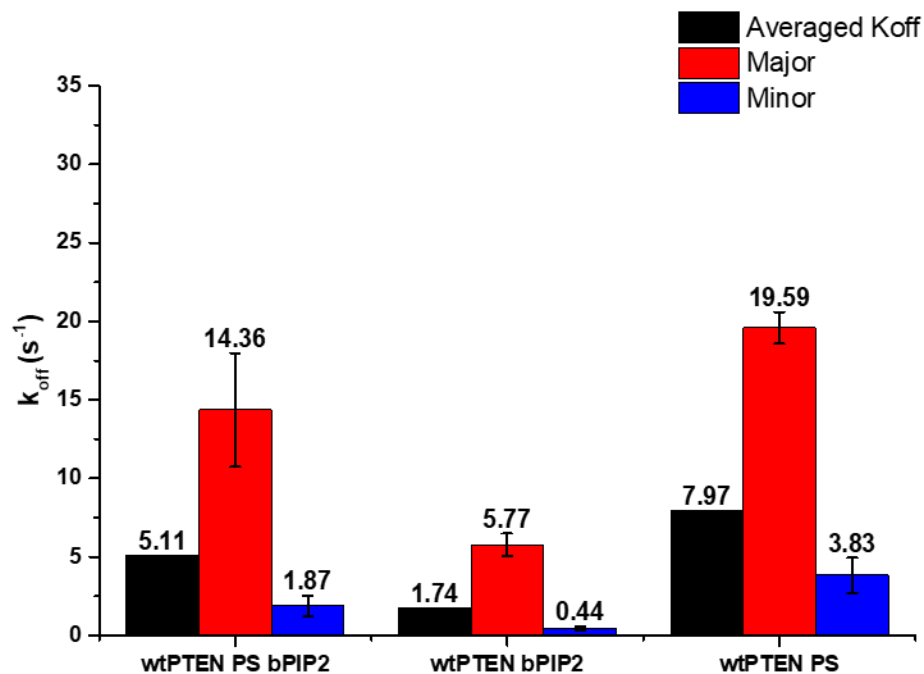


Figure 42. Rate constants of wtPTEN on SLB with the compositions 3% PI(4,5)P₂/30% PS , 3% PI(4,5)P₂,and 30%PS. The black column is the averaged rates weighted by the single molecule population. The red column is the major component, and the blue is the minor.

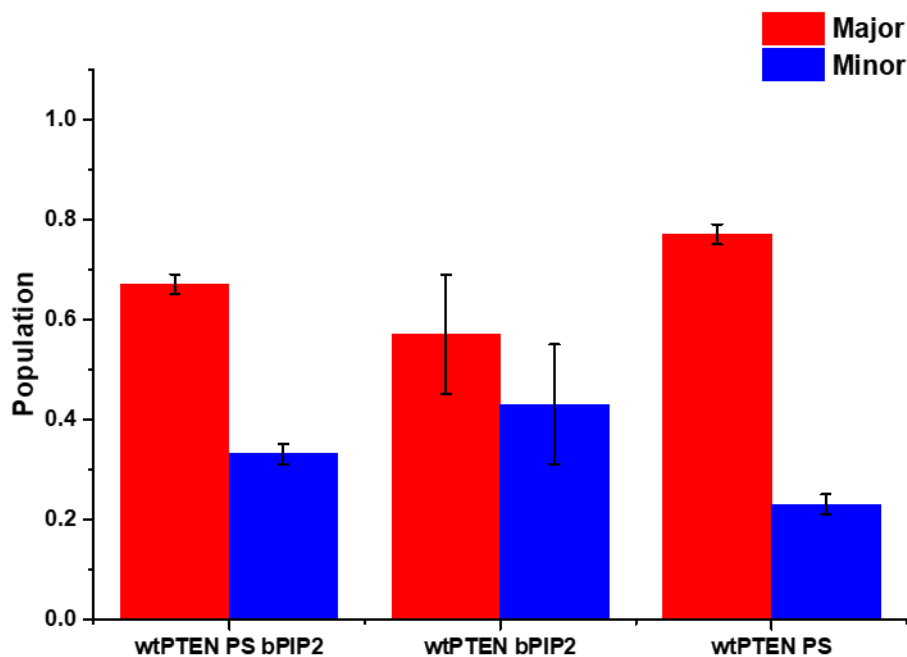


Figure 43. The rate population of wtPTEN on SLB with the three stated lipid compositions. There was only one -component for the lipid only data and two for the PTEN data.

Table 4 shows the global fit results next to the single molecule k_{off} . The rate trend for the multicomponent model membranes is 5%PI(4,5)P₂/ 30% PS < 3% PI(4,5)P₂ /30% PS < 1% PI(4,5)P₂ /10% PS which is expected. The 3% PI(4,5)P₂ single molecule dissociation rates are slightly slower than the ensemble 5% PI(4,5)P₂ global fit results, which is unexpected considering the high PI(4,5)P₂ concentration in the latter. For the fast component, there is a difference of a magnitude of 2 s⁻¹ for the averages and 1 s⁻¹ for the slow component. Even so, the k_{off} values are very close considering the different methods used to investigate these systems.

What the single molecule experiments provide is a direct measurement of the population of PTEN enzymes for each dwell time component. The population distribution (Figure 44) of the dwell times for wtPTEN 3% PI(4,5)P₂/ 30%PS membranes is 70/30 (short/long dwell times). This result is also satisfyingly close to the diffusion rate

Lipid Composition	30% PS	3% PI(4,5)P ₂	5% PI(4,5)P ₂	1% PI(4,5)P ₂ 10% PS	3% PI(4,5)P ₂ 30% PS	5% PI(4,5)P ₂ 30%PS
Global Fit 1 (s ⁻¹)	7.7 +/- 0.2		7.8 +/- 0.8	37 +/- 5		2.7 +/- 0.6
Global Fit2 (s ⁻¹)			1.4 +/- 0.1	6 +/- 1		0.5 +/- 0.3
Average Single Molecule (s ⁻¹)	7.97	1.74			5.11	
Single Molecule 1 (s ⁻¹)	20 +/- 1	5.8 +/- 0.7			14 +/- 4	
Single Molecule 2 (s ⁻¹)	4 +/- 1	0.4 +/- 0.1			1.9 +/- 0.7	

Table 4. A comparison of the global fit ensemble k_{off} results with the single-molecule k_{off} results. The average single molecule the mean of the two components from the single molecule data weighted by their population data.

population distribution (75/25). The 3%PI(4,5)P₂ membranes are at a 60/40 ratio, and the 30%PS membranes have a 75/25 distribution.

The delPTEN (Figure 44 and Figure 45) data shows the most dramatic difference in the short (fast) rate constant. In comparison to the wtPTEN data the 3% PI(4,5)P₂/30% PS delPTEN fast component is 1.3 +/-0.3X faster, 3%PI(4,5)P₂ is 2.6+/-0.8X faster and 30%PS 1.1+/-0.2X faster. The slow component, on the other hand, shows small to no change. For wtPTEN on 3% PI(4,5)P₂/ 30% PS the value is 1.9 +/- 0.7 s⁻¹ while delPTEN is 1.4 +/- 0.2 s⁻¹. For bilayers with 3% PI(4,5)P₂, the dwell times are 0.4+/-0.1 s⁻¹ and 0.84 +/- 0.05 s⁻¹ for wtPTEN and delPTEN, respectively and finally for 30% PS a k_{off} of 4 +/- 1 s⁻¹ for wtPTEN and 1.7 +/- 0.6 s⁻¹ for delPTEN is found. The population distribution of delPTEN has shifted in comparison to wtPTEN towards the higher population for 3% PI(4,5)P₂ from 60/40 to 70/30. For the 30% PS data, the population shifted towards the longer dwell times from 70/30 to 60/40 for delPTEN. The multicomponent bilayer has the same population ratio between the short and long components when comparing wtPTEN and delPTEN.

The C2 domain dissociation rates are not as intuitive as the previous results (Figure 46 and Figure 47). The k_{off} for the C2 domain interacting with 3% PI(4,5)P₂/ 30% PS has the same rate as the delPTEN within the error, 15 +/- 5 s⁻¹ for the short rate constant and 1.5 +/- 0.2 s⁻¹ for the long rate constant. For 3% PI(4,5)P₂, the fast rate increased to 22+/-8 s⁻¹ which is 1.3X time that of delPTEN and 3.6X faster than the wtPTEN dissociation rate. For bilayers with 30% PS, the C2 domain exhibits the same dissociation rate constant as delPTEN. The population data also trends to be 60/40 for 3% PI(4,5)P₂/ 30%PS, 65/35 3%PI(4,5)P₂, and 30% PS 75/25.

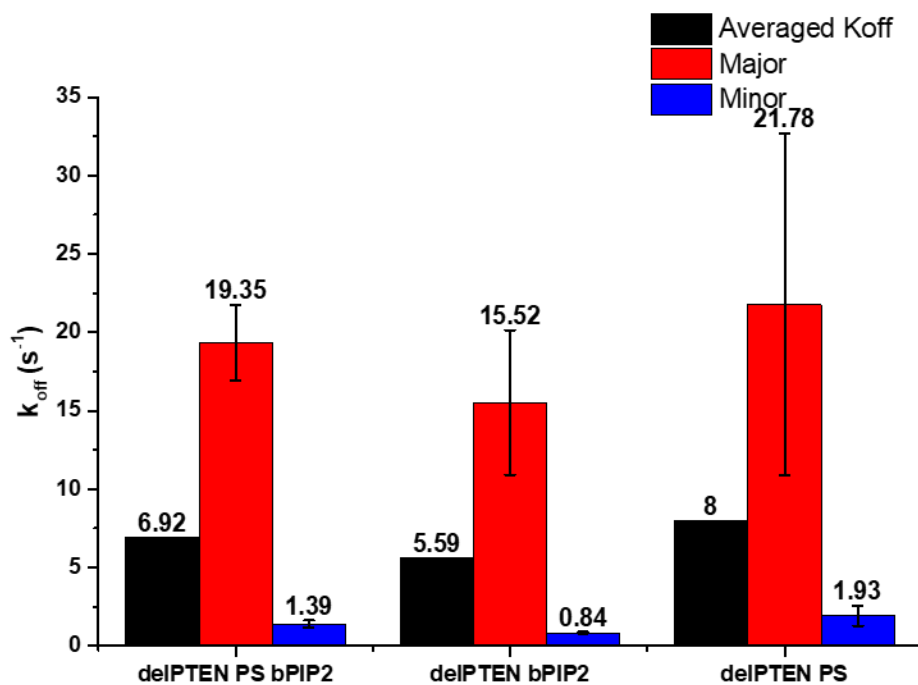


Figure 44. Dissociation rate constants of delIPTEN interacting with SLBs with the compositions 3% PI(4,5)P₂/30% PS , 3% PI(4,5)P₂, and 30%PS. The black columns are the averaged rates weighted by the single molecule population. The red columns are the major component, and the blue is the minor. The delIPTEN is a construct with the PBD domain deleted.

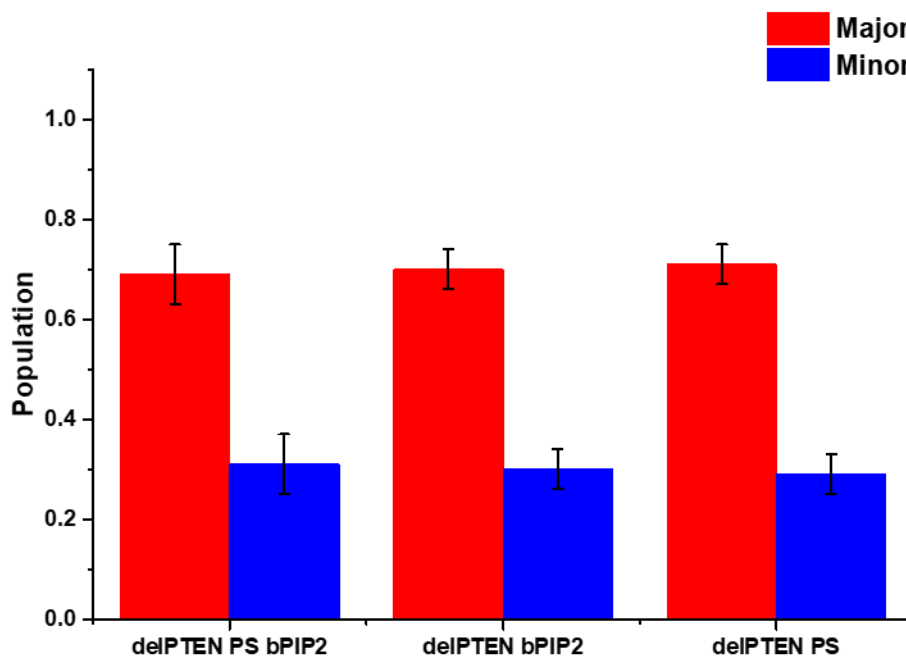


Figure 45. The dissociation rate populations of delIPTEN on SLBs with the three stated lipid compositions. There was only one -component for the lipid only data and two for the PTEN data.

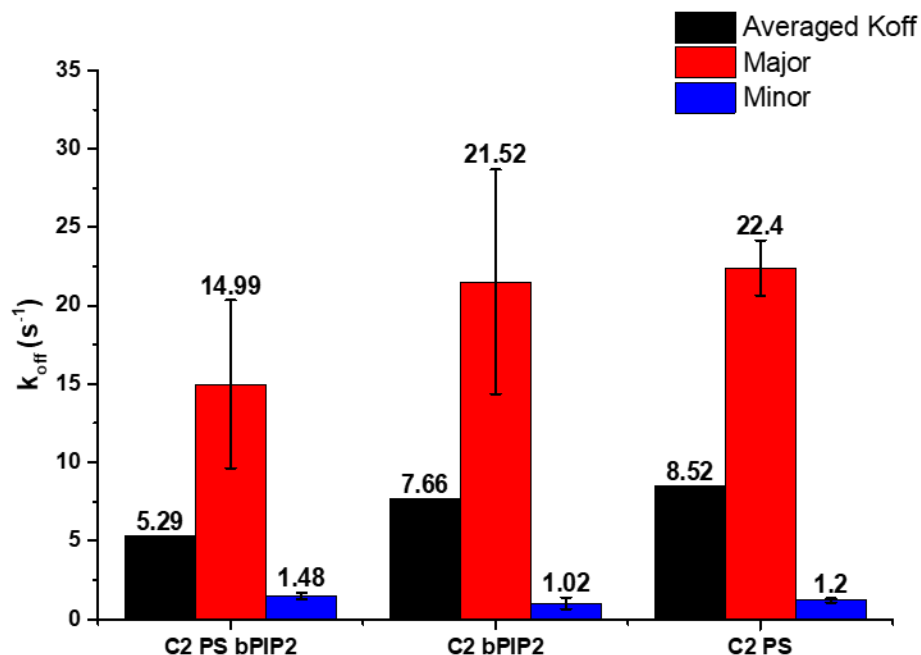


Figure 46. Dissociation rate constants of PTEN's C2 domain interacting with SLBs that have the compositions 3% PI(4,5)P₂/30% PS, 3% PI(4,5)P₂, and 30% PS. The black columns are the averaged rates weighted by the single molecule population. The red columns are the respective major component, and the blue is the minor. The C2 is a construct that is thought to interact with lipid membranes with nonspecific electrostatics via the basic amino acids of the CRB3 loop and acidic lipids.

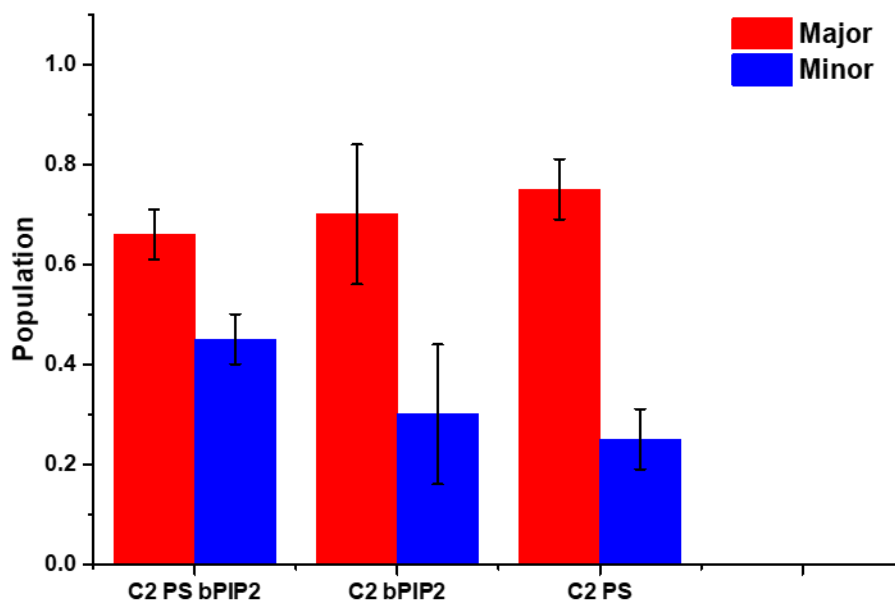


Figure 47. The rate populations of PTEN's C2 domain interacting with SLBs with the three stated lipid compositions. There was only one component for the lipid only data and two for the PTEN data.

Taken all of the dissociation rates together it is surprising that there are not a more dramatic dissociation rate constant differences between the domain constructs. In fact, it is rather remarkable how consistent the data is between the different lipid compositions and the domains. The greatest change seen is between wtPTEN and delPTEN for the 3% PI(4,5)P₂/PC supported lipid bilayers.

3.4 Discussion of Single-Molecule Results

Single-molecule techniques allow for the investigation of biological systems at the actual scale of the biological system. This means gathering stochastic data from complex biological systems but maintaining the heterogenic integrity of enzymes and uncovering new details of these processes not attainable with classic ensemble techniques⁶². In principle, a single-molecule experiment contains all the information of the molecular ensemble. This idea is derived from the statistical mechanic's ergodicity hypothesis. It states that the results over a sufficiently long time-average or a sufficient number of observations of single molecules would be equivalent to a standard population-average snapshot. In a review, N.G. Walter⁶² lists several advantages of the single-molecule experiment. (1) Reveals heterogeneity and disorder in a sample, (2) precise localization and counting of molecules in spatially distributed samples, (3) working at the low numbers observed for many biopolymers (typically 1-1000), (4) quantitative Markovian kinetics and statistics of biological systems, (5) uncover rare or transient species along a reaction pathway, (6) miniaturization and multiplexing of biological assay (i.e. single-molecule sequencing), (7) direct quantitative measurement of mechanical properties of single biopolymers and their assemblies, and (8) as Richard Feynman elegantly said, its also a way to "just look at the thing."⁶²

The dwell time data average for the k_{off} for wtPTEN on 3% PI(4,5)P₂/ 30% PS, 3% PI(4,5)P₂, and 30% PS SLBs, was comparable to the ensemble results. The 30% PS data from the single molecule and the stopped-flow techniques agrees with each other extraordinarily well. The 3% PI(4,5)P₂/ 30% PS single molecule results also followed the trends of the stopped-flow data; 1% PI(4,5)P₂/ 10% PS and 5% PI(4,5)P₂/ 30% PS. The one outlier was with the single molecule 3% PI(4,5)P₂ SLB when compared to the stopped-flow 5% PI(4,5)P₂ system. The single molecule results showed a smaller dissociation constant than expected. Ultimately to check these results, experiments with lipid systems which have the same bilayer compositions needs to be explored. Nevertheless, within the range of our investigation the results recapitulate each other.

Surprisingly, there is not as a dramatic change for the different domains when compared to wtPTEN on these SLB systems. The most significant change occurs on 3% PI(4,5)P₂ SLBs when the PBD domain is removed. The small difference for the 3% PI(4,5)P₂/ 30% PS bilayers between the two constructs is probably due to the overwhelming lipid component being PS. The loss of the PBD domain causes the enzyme to lose the ability sense the difference between the PI(4,5)P₂ bilayers and the PS bilayers. The specificity for PI(4,5)P₂ is associated with the PBD domain, and without it PTEN seems to interact only through non-specific electrostatic forces .

The comparison of the delPTEN and C2 domain gives insight into the contribution to PTEN binding between the catalytic domain and the C2 domain. The standout again is the 3% PI(4,5)P₂ containing membranes. The C2 domain's k_{off} rate constant is even bigger than the one for delPTEN. For the other lipid mixtures though, the data for the C2 domain are not that different from the delPTEN data. This suggests that while there may be some

contribution to the binding from the catalytic domain, overwhelmingly the interaction via electrostatics is through the C2 domain. This is not surprising considering the basic amino acids of the CBR3 loop make a (+5) positive charge contribution. Also, these data drive home that PTEN's specificity for PI(4,5)P₂ is driven through the PBD domain. It also seems to be truly specific to the phosphoinositide as evidenced by the PTEN k_{off} rates not changing with the PS membranes when tested with different domains.

The diffusion data support the rate data. There are two components, a fast diffusion, weakly bound component and a slower diffusing, stronger bound component. For wtPTEN the slow component trends as 3% PI(4,5)P₂/ 30% PS < 3% PI(4,5)P₂ < 30% PS as expected. Interestingly the fast component has the same diffusion coefficient for all three membranes. The delPTEN on 3% PI(4,5)P₂/ 30% PS membrane has a diffusion and dwell time data with values like the 30% PS/ wtPTEN system. The PBD domain has a substantial influence on how many lipids the protein is interacting with. Falke and Knight et al. ^{60, 64} conducted a study where they attached tandem PH domains and investigated their diffusion coefficients. What they found was that diffusion is a measure of how many lipids are bound to the protein. This implies that the shift to a faster diffusion for delPTEN when compared to wtPTEN on the multicomponent membranes directly indicates that the protein is interacting with fewer lipids. The 3% PI(4,5)P₂ may seem to be an outlier in this regard, but an examination of the population data shows a shift to the faster component as well.

The C2 domain diffusion data has a unique difference from the other two data sets. The main effect is that the fast diffusion component has increased in speed. Also, the population data for the PI(4,5)P₂ containing membranes is shifted towards the faster

component while 30% PS became more evenly split. First, examining the 30% PS data indicates that the C2 domain has two interaction states with the membrane. The catalytic domain has some additional interaction with PI(4,5)P₂, though weak as evidenced by the diffusion rate data. It is likely that the interaction occurs in the catalytic domain via the amino acids such as H93, which is known to hydrogen bond to the phosphate in the 5th position of the inositol ring. The real strength of the interaction occurs with the PBD domain. When this domain is deleted from the enzyme the benefit of binding to PI(4,5)P₂ is lost. The question of whether this increase of binding is due to the direct interaction of PI(4,5)P₂ and the PBD domain or because the protein conformation changes causes the entire length on the protein to be a better binder cannot be answered currently. Even so, the slow diffusion coefficient being so small does indicate that PTEN is interacting with many lipids on the surface, probably more than what 15 amino acids could account for.

Using both the ensemble data and single-molecule data we can suggest a detailed model for how the protein interacts with the membrane. The conclusions of these two projects are summarized in Figure 48. First, PTEN approaches the membrane. If the electrostatic potential is high enough, it will form a complex with the anionic lipids. It can either form a weakly bound fast diffusing complex, or if PI(4,5)P₂ is present, can form a strongly bound complex. If it is weakly bound complex, the protein can quickly scoot across the surface until it finds PI(4,5)P₂ and then form the strongly bound complex. Most of the protein is weakly bound, as shown by the single molecule work.

This weak interaction allows for a highly efficient search mechanism, only making a strong interaction if PI(4,5)P₂ is present. The strong interaction with PI(4,5)P₂ sacrifices lateral diffusion speed for the higher probability of finding the rare PI(3,4,5)P₃. Even in a

scenario where there is only PI(3,4,5)P₃ to start, PTEN would make PI(4,5)P₂ causing the protein to having a longer residency time and ensure all the PI(3,4,5)P₃ is turned over.

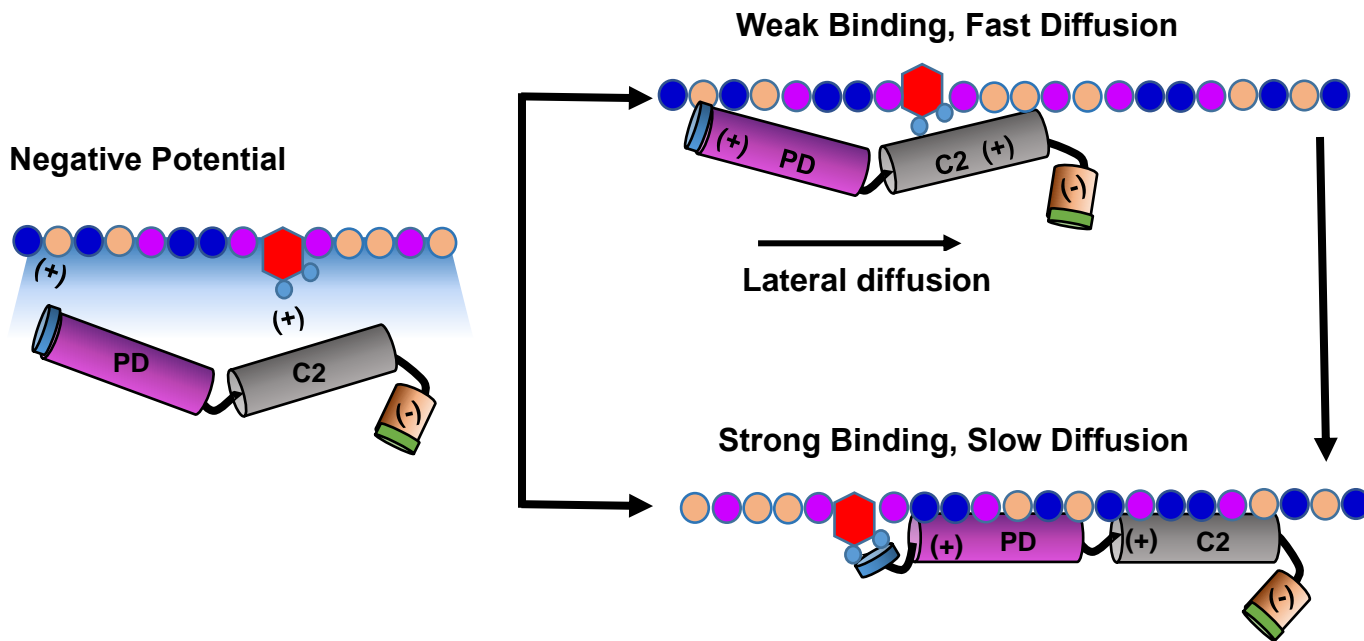


Figure 48. A model to account for the ensemble and single molecule results. First PTEN approaches the membrane due to the negative potential from the lipids. Second, depending on whether PI(4,5)P₂ is present or not PTEN can either be a weakly bound and fast diffusing or strongly bound and slow diffusing. If it is weakly bound, PTEN can quickly scoot across the membrane until it finds PI(4,5)P₂ and then become a strongly bound complex. The single-molecule data suggest that the majority, 60 to 70% of the membrane-associated PTEN is the weakly bound complex while only a minor portion of the population is strongly bound.

Chapter 4: Using Microfluidics to Generate a Gradient of PI(4,5)P₂ in Supported Lipid Bilayers

Many eukaryotic cells display distinct plasma membrane morphologies that depend on their life cycle. These morphologies are often dynamic, show a high level of complexity and in some instances give rise to polarized cells. We are interested in understanding how cells control micron scale polarization of membrane organization as seen during processes such as cytokinesis and chemotaxis or within statically polarized epithelial cells. PIPs and their interactions with proteins are pivotal for many of these dynamic and static membrane polarizations^{74, 75}.

A laterally non-uniform distribution of phosphoinositides is the hallmark of many important cellular events. In cytokinesis, for example, PI(4,5)P₂ production and polarization are crucial for spindle orientation, mitotic cell shape and bridge stability after furrow ingression. Subsequently, PI(4,5)P₂ hydrolysis is essential for normal cytokinesis abscission⁷⁶⁻⁷⁹. Chemotaxing cells, such as *Dictyostelium discoideum* or neutrophils, show distinct and dynamic phosphoinositide polarization characterized by the accumulation of PI 3-kinase and phosphatidylinositol-3,4,5-trisphosphate (PI(3,4,5)P₃) at the leading edge of the migrating cell⁷⁶⁻⁸⁰. An example for polarized cells with a globally static polarized structure is absorptive epithelial cells. Epithelial cells increase their surface area by developing the so-called “brush border” membrane, which is a highly structured plasma membrane characterized by long, thin, highly curved structures (typically 100nm in diameter and 100nm - 2,000nm in length). The apical side of epithelial cells shows increased PI(4,5)P₂ concentrations, while the basolateral side exhibits increased PI(3,4,5)P₃ concentrations in the PM^{76, 77, 79, 81}.

Phosphoinositides have been shown to bind a broad range of protein targets that are involved in an extraordinary array of physiological functions⁸² including those crucial to cell motility. Temporal and spatial control of phosphoinositide levels consequently regulates the phosphoinositide-binding protein functionalities. This spatiotemporal organization is an important aspect for the proper execution of these signaling events. While several studies have described polarized phosphoinositide distribution in living cells in response to external stimuli, many aspects of the generation and maintenance of such gradients, in particular concerning the physical chemistry of the underlying processes, have not been sufficiently detailed. Despite the obvious benefits of combining the results from *in vivo* and *in vitro* studies, there is, to the best of our knowledge, currently no *in vitro* platform available that provides the experimental freedom required to investigate the many biophysical facets of lateral membrane gradients. To understand the biophysical underpinnings of membrane gradients concerning mediating signaling events, it is important to have complete experimental freedom concerning the composition and physical properties of the lipid bilayer as well as the nature of the chemical species (e.g., proteins, bivalent cations) interacting with that bilayer. It is the goal of this project, to develop a device that allows for the systematic investigation of how gradients can be created, how they are maintained and how proteins affect and interact with such lipid gradients^{76, 77, 79}.

Solid-supported lipid bilayers have been established as facile tools for the biophysical characterization of model membrane systems⁸²⁻⁸⁶. The Sanii⁸⁷ and Huskens⁸⁸ groups both utilized SLBs to develop biomimetic devices for the preparation of lipid membrane gradients. With the device developed by the Sanii⁸⁷ group, a membrane

gradient can be created that enables the investigation of gradient diffusion, protein-lipid interactions, and gradient dependent domain formation. Their method uses a three-dimensional PDMS stamp to deposit two spatially separated multilamellar lipid stacks onto a glass coverslip. Upon rehydration, the stacks “heal” the divide between them forming a contiguous unilamellar SLB with a gradient between the two deposited multilamellar lipid stacks⁸⁷.

The Huskens⁸⁸ group developed an experimental platform that can ‘lock-in’ the desired lipid gradient profile in an array of micron-sized Cr corrals. In their work, they use a mixture of zwitterionic and negatively charged lipids with a high melting point to obtain the lipid bilayer. Heating the system to above the phase transition temperature causes the lipids to enter a mobile fluid phase, and a gradient of the negatively charged lipids within the lipid bilayer is obtained by applying a voltage that draws the charged lipids to one side of the corral. Upon cooling below the phase transition temperature of the lipid mixture, the lipids enter the gel phase, “locking-in” the gradient⁸⁸.

The Sanii group’s experimental platform is simple and generally has no limitations concerning the composition and physical properties of the lipid stacks (e.g., lipid phase transition temperature and charge). However, the shape and slope of the lipid gradient cannot be controlled by this device. The method introduced by the Huskens group allows for a highly tunable lipid gradient; the length scale of the membrane gradient is in a physiologically relevant range, and the gradient can be “locked-in,” which is potentially a major advantage for sensor applications. However, the method requires lipids with high gel/liquid-crystalline phase transition temperatures and the use of an electric field to create a lipid gradient of anionic lipids. In both methods, the gradient formation is

restricted to the SBL, i.e., the fluid phase above the lipid bilayer cannot exhibit a gradient of one or more of its constituents (e.g., a non-uniform distribution of a lipid-modifying enzyme).

The device that we have developed combines the advantages of both existing techniques. These include the freedom of choice concerning the lipid composition and physiologically relevant length scales over which the gradient is generated. In addition to this, our device adds the ability to create a protein or bivalent cation gradient in the aqueous phase above the lipid bilayer. It is even possible to fabricate a gradient in the lipid bilayer with an opposing gradient in the aqueous phase. The steepness of the respective gradient and within certain limits its functional behavior can be chosen based on the experimental objectives. To show the broad applicability of this microfluidic device, we will demonstrate that we can create phosphoinositide gradients on various length scales, ranging from 2 mm to 50 μm . We further show how a gradient in the aqueous layer above a homogeneous lipid bilayer can impart a non-uniform response in the lipid bilayer. This biomimetic platform can be combined with a Total Internal Reflection Fluorescence (TIRF) microscopy setup, which allows for the convenient observation of the time evolution of the gradient and the interaction of ligands with the lipid bilayer.

4.1 Methodology

Constructing the Microfluidic Platform

The Sylgard 184 silicon elastomer kit (Dow Corning, Midland, MI) was used to make the polydimethylsiloxane (PDMS) component of the microfluidic device. This piece of the device is where the channels are imprinted from a silicon master during the molding process. To do this, curing agent (10% by weight) added to the elastomer base and then

mixed vigorously. This was then followed by degassing the mixture for an hour. The uncured PDMS was poured onto the silicon master, degassed for an additional 10 minutes and then cured in the oven at 72°C for 45 minutes. The now hardened PDMS was cut from the silicon master, and the inlet and exit holes were punched with a blunt 19 gauge BD PrecisionGlide needle. This PDMS mold, with the silicon master design imprinted on its surface, was further cleaned with Scotch tape to remove dust and debris. This is the top of the microfluidic device.

The base of the microfluidic device is a 24X40mm N0.1.5 Gold Seal cover glass slide used for TIRF microscopy. The TIRF slide was piranha cleaned for an hour, rinsed with copious amounts of HPLC water and stored in HPLC water until needed. The slide is then rinsed with methanol and dried under N₂ gas.

At this point, the PDMS mold and TIRF slide are plasma cleaned with an air plasma. First, the TIRF slide is placed in the chamber and plasma cleaned for two minutes. Then the Scotch tape is removed from the PDMS, and the PDMS is added to the chamber. The PDMS and TIRF slide are cleaned for an additional 45 seconds. The slide is then placed over the PDMS mold and with gentle pressure sealed to the PDMS. This is an irreversible attachment.

Developing a Supported Lipid Bilayer in the Microfluidic Platform

To form SLBs loading buffer is passed through the microfluidic device from the outlet. By passing this solution in the reverse direction of the setup, we ensure that all air bubbles are pushed out of the device. Also, this priming allows us to check for leaks since the pressure from pushing the fluid by hand into the device is much higher than the pressure achieved by the syringe pump that will be used during the experiment. To

introduce any liquid from the inlet side into the microfluidic device, a 3mL syringe with a 25-gauge needle is attached to the inlet using PTFE#3 AWG thin wall tubing from Cole-Parmer. This tubing OD and the needle OD were matched to ensure a liquid-tight seal. In our observation, the only time leaking occurs is when there is back pressure due to a clog.

The vesicle suspension can be introduced through the inlets. Here three syringes are attached to two feet of tubing. When making homogeneous SLBs, the three syringes are filled with vesicle suspensions of equal concentrations (1mM). When the syringe pump is run at 10 μ l/min and with two feet of tubing it takes twenty minutes for the vesicles to reach the observation chamber. This “dead-time” can be adjusted by either changing the length of the tubing or speed of the syringe pump. This method was used in our initial test experiments to follow SLB formation by fluorescence microscopy.

A more convenient method is to introduce the vesicle suspension through the outlet of the microfluidic device by using a hand-driven syringe. This is the procedure we used to obtain laterally homogeneous lipid bilayers once we had confidence in the SLB formation. After 100 μ l of the suspension is passed, the vesicle suspension is allowed to sit for 30 minutes in the observation chamber. Then 100 μ l of HPLC water is passed to break any remaining intact vesicles due to osmotic stress. This is followed by 100 μ l of the physiological buffer. While we were not able to discern any macroscopically visible imperfections in the lipid bilayer (e.g., holes), it cannot be ruled out that such imperfections exist below the resolution limit of the microscope. To fill in these potential holes, a 100 μ l of a BSA solution (5 μ g/mL) was introduced into the observation chamber and allowed to sit for 30mins. This is followed by a final wash with a 100 μ l of our physiological buffer

again. To maintain the integrity of the SLB, it is important that no air bubbles are moving through the device as these various solutions are introduced.

Establishing a PI(4,5)P₂ Gradient

Insertion Method

The critical micelle concentration (CMC) for TopFluorPI(4,5)P₂ is not known, however, using dynamic light scattering measurements we have found for nanomolar concentrations that TopFluorPI(4,5)P₂ is dissolved as a monomer. We take advantage of this property, by creating three TopFluorPI(4,5)P₂ solutions of different concentrations below the CMC, which are then being used to generate a gradient of fluorescently labeled PI(4,5)P₂ embedded in an otherwise homogeneous lipid bilayer. Aqueous TopFluorPI(4,5)P₂ solutions with three different concentrations are obtained by drying appropriate amounts of the lipid from organic stock solutions as described above and redissolving the lipid film in the loading buffer. The aqueous samples are then drawn up into three 1mL syringes, and any air bubbles present in the syringe are removed. Then a 25G needle with two feet of tubing is attached to the syringe. The syringe plunger is depressed so that the solution is pushed through to the end of the tubing. All three syringes are placed in the syringe pump, and the bar is placed against the plungers so that there is a small drop at the end of each tube. The tubes are inserted into the microfluidic inlets, and the syringe pump is started. The syringe pump is run for 20 minutes at 10 μ l/min. During this time the TopFluorPI(4,5)P₂ partitions into the homogeneous SLB that has been previously made. To push any labeled lipid that did not insert into the lipid bilayer out of the observation chamber, the syringe pump is stopped, and the syringes with the lipid solutions are replaced with three new syringes that are loaded with physiological buffer solutions. The physiological buffer solution is run for 20 minutes at

the same rate as the lipid solution before. After this point, the syringe pump is stopped, and the fluorescence imaging of the bilayer starts. For these experiments, a 60X TIRF objective is rastered across the observation chamber perpendicular to fluid flow.

While the method described above is suitable for the microfluidic device with the large observation chamber because of the long equilibrium times for the gradient, a different method is needed for the microfluidic device with the sub-millimeter chambers (for the narrower chambers the equilibration occurs on a time scale of minutes rather than hours). To deposit the labeled PI(4,5)P₂ and flush the SLB with buffer, the transition between these solutions needs to be immediate. To achieve this the labeled solution with the labeled PI(4,5)P₂ is first pushed through the syringe to the end of the tubing before attaching it to the microfluidic system. The syringe is then switched with a buffer loaded syringe. This is then attached to the inlets of the platform. The result is that when the syringe pump is started labeled PI(4,5)P₂ is introduced and immediately chased with buffer in a process we deem as a load (deposition of labeled PIP₂) followed by flush (wash with buffer). The imaging is started when the syringe pump is started. With the load-flush experiment, the buffer is run for twenty minutes and then stopped with an image taken once every minute for an hour at the start of the syringe pump.

Direct Deposition Method

Gradients Beyond Lipids

The SLB films were prepared as described before. Three membranes were tested for the interaction with a Ca²⁺ gradient: 5% PI(4,5)P₂, 94.9% DOPC, 0.1%TopFluor®PI(4,5)P₂; 5% PI(4,5)P₂, 30%Cholesterol, 64.9%DOPC, 0.1%TopFluor®PI(4,5)P₂; 30%POPS, 69.9%POPC, 0.1%TopFluor®PS. Physiological buffer solutions (see above) with 1mM, 2mM, and 3mM calcium concentrations were

prepared and loaded into the three syringes connected to the inlets of the microfluidic device. The Ca^{2+} buffer solutions were pumped through the microfluidic device with 10 $\mu\text{l}/\text{min}$ rate while simultaneously obtaining TIRF images of the respective lipid bilayer. Images were taken every 5 minutes for an hour for the $\text{PI}(4,5)\text{P}_2$ SLBs. For the PS-containing membranes, the objective was rastered in a 2.0mm x 2.5mm rectangle once every 20min for 22hrs. The images at each time point were stitched together and analyzed.

Imaging the Gradients

The stitching of the rastered images to a single image was done using the Nikon Elements software. All other image processing was done in ImageJ (NIH Bethesda, MD). For the topology images, a movie at nine positions across the channel was acquired. The mean fluorescence intensity was calculated for each frame of the movie. These data were imported into Origin software (Northampton, MA) and a topology graph of the mean fluorescence intensity was plotted against time and position.

For the Ca^{2+} experiments, the data was acquired by the same means as above. Instead of calculating the mean fluorescence intensity, the intensity was thresholded to the top 1.3% of intensity brightness. This was then converted into a binary image where the brightest areas are counted as domains by selecting the thresholded areas that have pixel diameter greater than 5^2 pixels and a circularity between 0.5 - 1. These domains were counted, the average diameter calculated, and percent area of the frame determined for each frame of each movie. These data were imported into the Origin software, and two topology graphs were constructed: number of domains as a function of time and position, and the percent area of the frame as a function of time and position⁶⁷.

4.2 Insertion of aqueous PI(4,5)P₂ in SLB

The work of Byfield *et al.*⁸⁹ was the inspiration behind using a microfluidic gradient generator to make laterally heterogeneous supported lipid bilayers (SLB). The “Christmas tree” design of this microfluidic platform, originally fashioned by S. Dertinger *et al.*,^{90, 91} takes three different initial concentrations and forms a

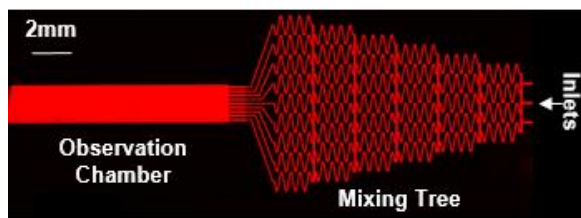


Figure 49. Wide-field fluorescence image of the microfluidic gradient generator with a homogenous SLB composed of DOPC and 1%RhodaminePE. The three initial concentrations are introduced into the inlets. They are of equal concentrations and composition, resulting in no gradient. The high fluorophore percentage was used for aesthetic reasons to highlight the features of the microfluidic platform

gradient in the observation chamber of the device. The lamellar flow of the fluid prevents mixing perpendicular to the flow direction once the fluid enters the observation chamber (Figure 49). At the first level of the mixing tree, there are three inlets that split and

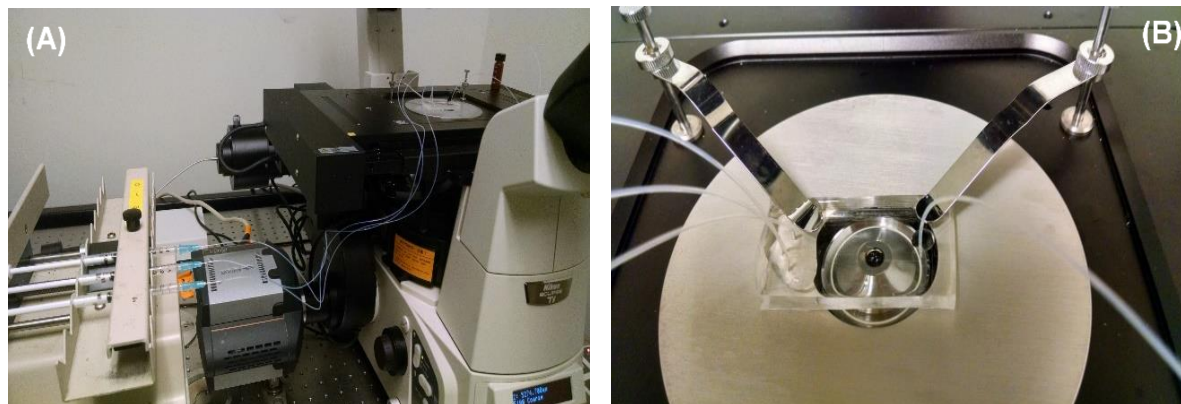


Figure 50. The setup of the microfluidic platform on the TIRF microscope. (A) Demonstration of the connection between the syringe pump and the microfluidic platform. The fluids in the syringe set varies in concentration and or composition to develop a gradient. The syringes are connected via 2ft of tubing to the microfluidic device, and the rate of flow is controlled by the syringe pump. (B) The tubing connections to the microfluidic platform as well as the outlet tubing which empties into a waste vial. The objective is centered over the observation chamber to record the changes of the SLB gradient. Since this setup is placed directly on the microscope, images can be acquired in real time at all stages of the experiment, which is critical for monitoring the gradient evolution under various conditions.

recombine the initial sample concentrations to form four new concentrations. This process is repeated at each subsequent level, ending in a total of nine outlets which recombine into the large observation chamber. When a concentration series is introduced into the microfluidic device, (see Figure 50 for the physical setup of the device and Figure 51 for images of a lipid sample gradient) the concentration gradient brackets the lowest and highest concentrations of the three samples introduced through the device inlets. The steepness of this gradient is highly tunable by controlling the flow rate of the fluid through the device, where at the highest speeds the gradient forms a step function⁹¹. The lamellar flow of the fluids as they exit the nine channels to enter the observation chamber is essential for successful gradient development. The lack of turbulent mixing perpendicular to the fluid's flow direction means that the only physical pathway for the gradient to equilibrate is by the Brownian motion of the dissolved molecules or suspended vesicles. The lamellar flow of the fluid is a key physical characteristic of the device since it provides maximum flexibility concerning the kind of gradient that is being generated, being it dissolved molecules or suspended unilamellar vesicles^{92, 93} (Figure 51).

4.3 Generation of a PI(4,5)P₂ gradient in a DOPC SLB.

To generate a PI(4,5)P₂ gradient, first, a homogenous SLB composed of DOPC and Rhodamine-PE (Rh-PE/10ppb) was created in the microfluidic device (Figure 51B). The Rh-PE is added to the SLB lipids to check for macroscopic defects and to check the bilayer's fluidity using smTIRF (in our experiments we bleach a portion of the SLB and check for recovery in that area after 10 mins). To visualize the gradient of phosphoinositides, we utilized fluorescently labeled TopFluor-PI(4,5)P₂ (10nM, 30nM,

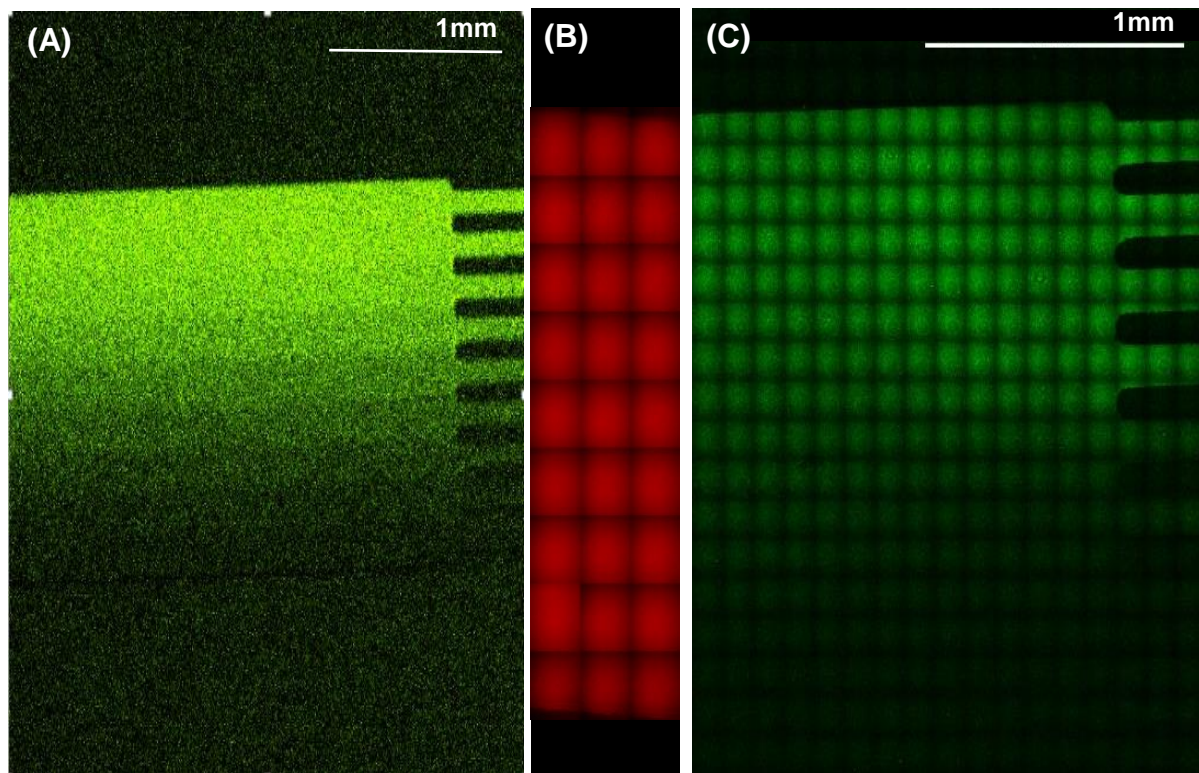


Figure 51. TopFluorPI(4,5)P₂ gradient in a homogeneous DOPC bilayer labeled with Rhodamine PE. (A) Widefield fluorescence image of the microfluidic platform's observation chamber showing a TopfluorPI(4,5)P₂ gradient in the aqueous phase above the SLB. (B) Stitched fluorescence image of the homogeneous DOPC bilayer labeled with 10ppb Rh-PE. After the SLB was fully developed, the observation chamber was flushed with buffer solution to remove any remaining lipid vesicles. After the wash, the TopfluorPI(4,5)P₂ gradient with inlet concentrations of 10nM, 30nM, and 60nM was introduced. (C) Stitched TIRF image of the DOPC bilayer with inserted TopFluorPI(4,5)P₂. The individual image squares are representative of one camera frame (single individual image before stitch, 138.24 μm x 138.24 μm).

60nM). We have found that the lipid is monomeric in aqueous solution at these concentrations. Due to the negative charge of the TopFluorPI(4,5)P₂ headgroup and the steric hindrance imposed by the large fluorescent label on the acyl chains, the mutual interaction of these lipids is dominated by repulsive electrostatic forces, resulting in a critical micelle concentration (CMC) significantly higher than the nanomolar concentrations used in our experiment (please note that the CMC for unlabeled PI(4,5)P₂ is in the 30 – 40 μM range)⁹⁴. A gradient of monomeric (dissolved) TopFluorPI(4,5)P₂ can, therefore, be obtained in the aqueous phase when these three different

concentrations of the lipid are introduced into the three inlets of the microfluidic device (Figure 51). The partition coefficient between the aqueous solution and the SLB of the lipid still leans toward membrane incorporation, so, as the TopFluor-PI(4,5)P₂ flows over the DOPC SLB, the labeled lipid will spontaneously insert. The lamellar flow of the microfluidic device ensures that there is no cross-channel mixing (Figure 51A), maintaining the aqueous PI(4,5)P₂ gradient during the insertion process (Figure 51C).

Figure 52 shows the results of TIRF imaging of the SLB after the insertion of the TopFluor[®]PI(4,5)P₂. We acquired image 52A by rastering the 60X TIRF objective perpendicular to the fluid flow, taking an image at nine equally spaced positions. This scan was repeated once every 30min for 24 hours to monitor the time evolution of the PI(4,5)P₂ gradient. As can be seen qualitatively, the TopFluor[®]PI(4,5)P₂ gradient is maintained as the lipid inserts into the preformed SLB and slowly equilibrates over 24 hrs. Figure 52B shows the mean fluorescent intensity per image frame across the observation channel (i.e., perpendicular to the flow direction). The initial distribution of the fluorescently labeled lipid is close to the distribution expected from a sigmoidal model. Figure 47C shows the temporal evolution of the TopFluorPI(4,5)P₂ gradient as a topology graph (see also the corresponding movie in the supplementary material). For this graph, a single raster across the channel perpendicular to the fluid flow was charted against time and color-coded to indicate the fluorescence intensity. The color map shows the time-dependent equilibration of the gradient. It takes over 22 hrs for the gradient of TopFluorPI(4,5)P₂ to equilibrate across the chamber. This is expected for a lipid diffusing via Brownian motion at about 2.7 - 2.8 $\mu\text{m}^2/\text{s}$ ^{8, 64, 70} in a

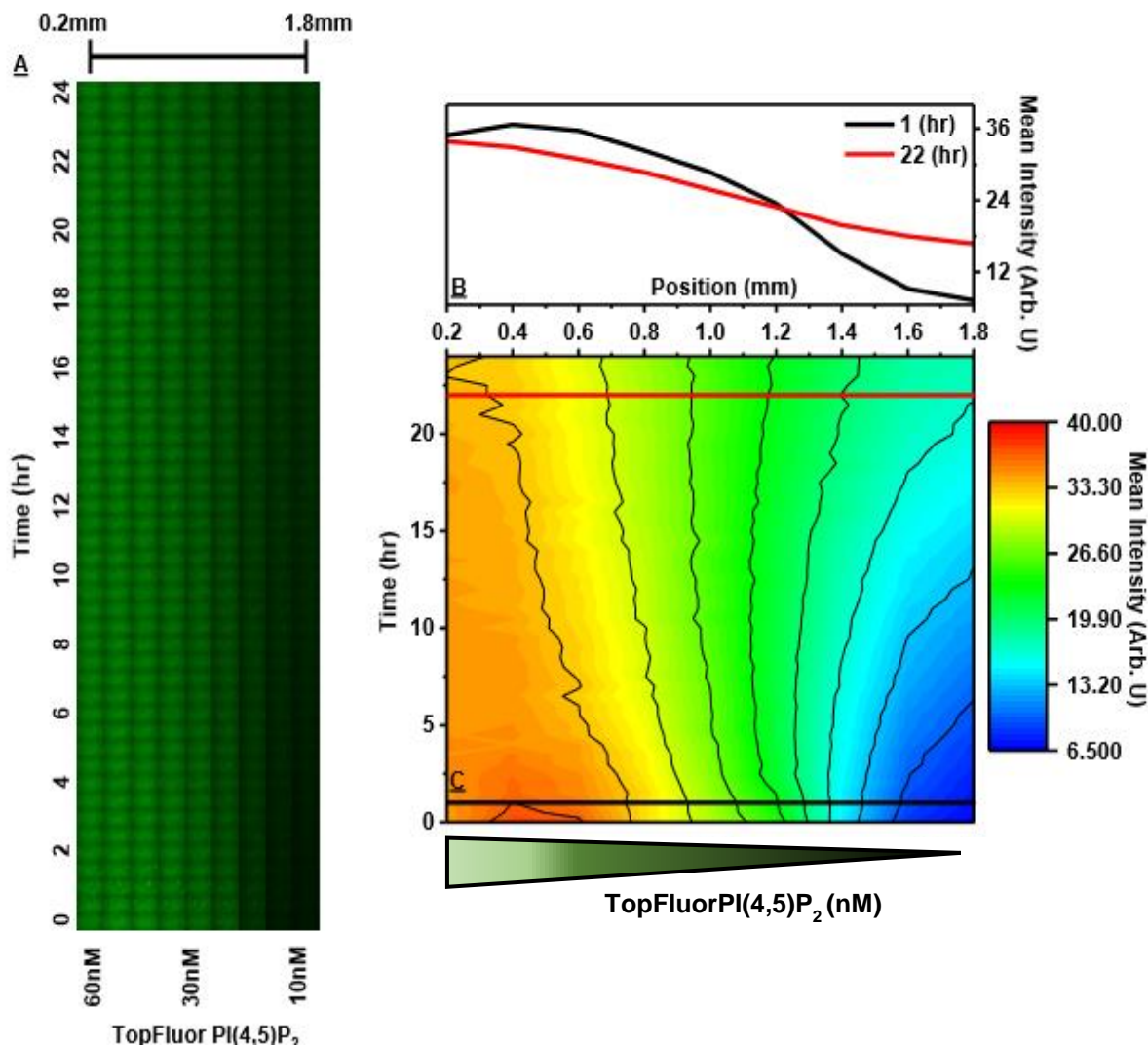


Figure 52. Temporal evolution of the PI(4,5)P₂ gradient in the DOPC SLB. It takes over 22hrs for the TopFluorPI(4,5)P₂ gradient to equilibrate across the 2 mm chamber. (A) Once an hour nine images were taken across the chamber and stitched together. Over time we see the brightest areas become dimmer and the darkest image parts becomes brighter indicating equilibration by diffusion (B) Integrated fluorescence intensities for each sub-image across the chamber at the beginning of the experiment. (C) Contour graph of the fluorescence intensity distribution as a function of time. The concentration ranges from 10nM to 60nM TopFluorPI(4,5)P₂.

chamber of 2 mm width. We found these measurements to be highly reproducible ($n=5$). For each set of parameters, i.e., TopFluorPI(4,5)P₂ start concentration, flow speed, and SLB composition, the gradient is consistent and repeatable as measured by the equilibration time of the gradient.

The second option to obtain a PI(4,5)P₂ gradient is to use vesicles with different compositions at the three inlet ports of the microfluidic device. To illustrate this approach, three unilamellar vesicle suspensions with the following compositions were made: 10%PI(4,5)P₂, 0.1%TopFlour PI(4,5)P₂, 90%POPC; followed by 3%PI(4,5)P₂, 0.03%TopFlour PI(4,5)P₂, 97%POPC; and 100% POPC (all percentages are mol%). These three initial vesicle compositions, when combined in the mixing tree, will result in nine ratios of the three compositions spanning across the outlets of the device. This is in contrast to the lipid monomer insertion, where there are nine different concentrations of the monomeric lipid after mixing. In comparison to the monomeric lipid insertion method, where the degree of lipid insertion is unknown, this method has the advantage that the precise lipid composition in the SLB is known; in this case, the range of the gradient is 10%PI(4,5)P₂ – 0%PI(4,5)P₂.

Figure 53C shows quantitatively the temporal evolution of the lipid gradient, which is similar to the equilibration of the gradient obtained through lipid insertion (Figure 52C). One might be concerned that the deposition of lipid vesicles with different compositions may lead to patchiness at the submicrometer scale. However, the image does not reveal any patchiness (though such patches would be at the limit of the resolution of the microscope) and there is no other indication of such heterogeneities. We believe that mixing of the lipids between adjacent vesicles occurs during the formation of the SLBs.

Also, if such small patches existed, local diffusion would lead to mixing at a sub-minute timescale.

Both methods, the lipid insertion and deposition of vesicles with different compositions, exhibit advantages and disadvantages regarding creating lipid gradients. The lipid insertion method creates very smooth gradients, while the deposition of vesicles with different lipid ratios leads to a less smooth gradient that has an initial appearance closer to a step function. Regarding the quality of the gradient, the lipid insertion method

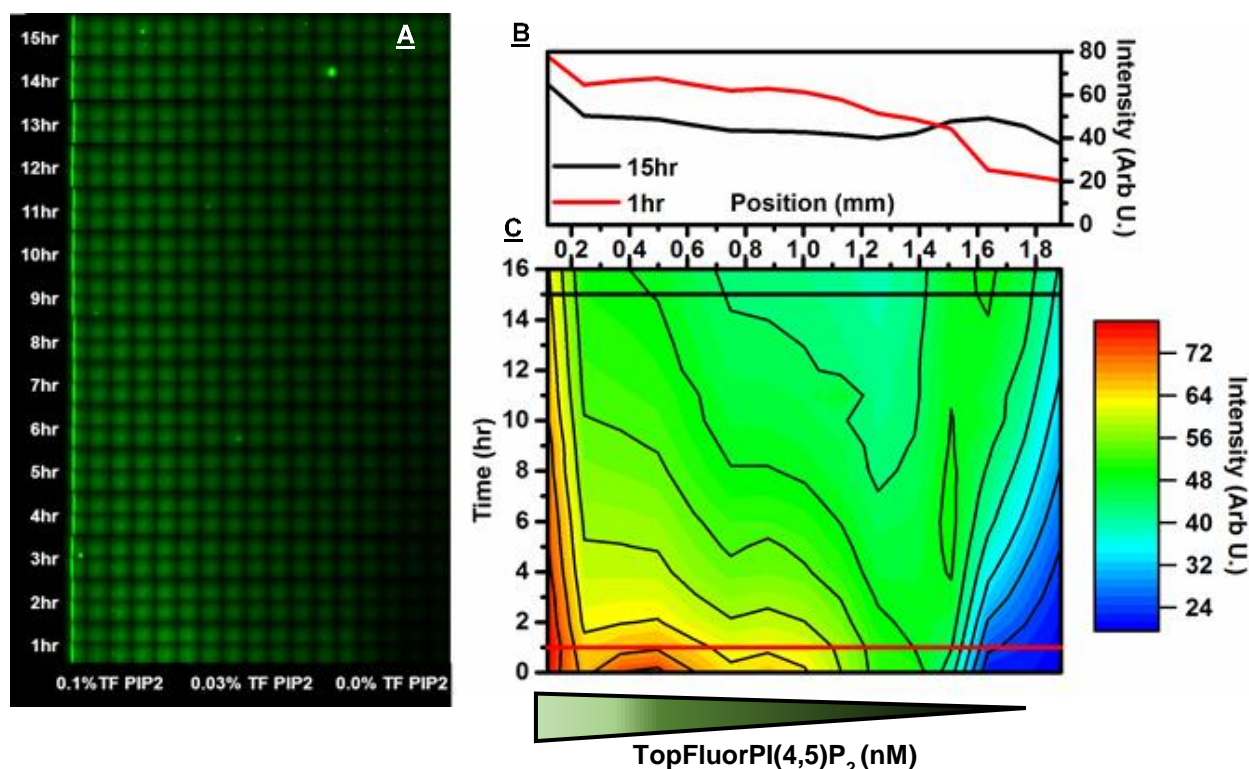


Figure 53. Gradient of PI(4,5)P₂ obtained using vesicles with different PI(4,5)P₂ concentrations.

Vesicle suspensions with equal vesicle concentrations but different vesicle compositions were introduced into the three inlets of the microfluidic device. The vesicle compositions were 10%PI(4,5)P₂/0.1%TopFluorPI(4,5)P₂/90%DOPC, 3%PI(4,5)P₂/0.03%TopFluorPI(4,5)P₂/97%DOPC, and 100%DOPC. The ratio of the unlabeled/labeled PI(4,5)P₂ is kept constant for all vesicle compositions. It is assumed that distribution of the unlabeled PI(4,5)P₂ mirrors the distribution of the labeled PI(4,5)P₂ analog. (A) Image obtained by taking once an hour 9 images across the chamber and stitching them together. (B) Integrated fluorescence intensities for each sub-image across the chamber at the beginning of the experiment. (C) Contour graph of the fluorescence intensity distribution as a function of time.

is therefore preferable. However, this method is limited by the type of the lipid that is being used and its concentration, since it requires the inserted lipid to be monomeric in solution. The major advantage of the vesicle deposition method is that one has complete freedom concerning the type of lipid gradient that is being created. The experimental context will determine which method is the preferred one to answer a particular biophysical question.

4.4 Effects of a Gradient of Ligand on Homogenous Bilayer

To test whether a gradient of a solute interacting with a laterally homogeneous SLB can impart a gradient specific response in that SLB, we investigated the interaction of a Ca^{2+} gradient with SLBs composed of anionic lipids. The domain-forming effect of calcium upon interaction with anionic lipids like phosphatidylserine (PS) or $\text{PI}(4,5)\text{P}_2$ containing membranes is well established⁹⁵. We hypothesized that the interaction of a Ca^{2+} gradient present in the bulk phase above mixed PC/PS or PC/ $\text{PI}(4,5)\text{P}_2$ SLBs leads to the formation of domains in a Ca^{2+} gradient-dependent manner.

The interaction of PS with Ca^{2+} is well studied, and it has been hypothesized that Ca^{2+} interacts with the PS headgroup via two modes. (1) Ca^{2+} is interacting with the carboxylic acid group of the serine. (2) Ca^{2+} can also interact with the phosphate linker of the glycerol backbone⁹⁵⁻¹⁰¹. While it is unclear which type of interaction is the dominant one, either interaction can lead to a bridging of adjacent PS molecules, causing clustering of the lipid in mixed lipid bilayers. Visualization of PS clustering in an SLB with fluorescence microscopy is not trivial, and usually, high-resolution techniques like AFM are used to visualize these domains in fluid bilayers. To circumvent this problem, we used mixed POPS/POPC SLBs. POPS in the absence of Ca^{2+} has a gel/liquid-crystalline phase transition temperature of 14°C ,¹⁰² i.e., POPC and POPS form a mixed fluid phase at room

temperature. In Langmuir film experiments, the addition of Ca^{2+} leads to condensation of PS monolayers^{103, 104} and the addition of Ca^{2+} to a mixed POPC/POPS SLB is expected to give rise to domain formation in the leaflet distal to the glass support. We hypothesized that these PS domains would form in a Ca^{2+} gradient-dependent manner.

In figure 54, we show an SLB composed of 30% POPS, 0.1% TopFlourPS, and 69.9%POPC as it interacts with a Ca^{2+} gradient. The Ca^{2+} concentrations of the solutions introduced into the inlet channels were 1mM, 2mM, and 3mM, respectively, and the experiment was carried out at room temperature. In contrast to the previous experiment, where we stopped the flow of the buffer solution during imaging, the Ca^{2+} gradient flow was maintained throughout the entire duration of the experiment. This was to avoid that the Ca^{2+} in the fluid phase equilibrates across the observation channel. Figure 54 is a montage of images that are obtained near the mixing channel outlets (see the corresponding movie in the supplementary material). The stitched image was obtained by combining individual images acquired across the channel using TIRF microscopy. This rastering was repeated once every 20 minutes over 3 hours (it takes 5min to obtain all images for the stitched image). POPS forms gel phase domains, as inferred from the jagged nature of the domain boundaries, upon interaction with the Ca^{2+} cations. The formation of these domains always starts in the area of the highest Ca^{2+} concentration, though the precise position within the high concentration region is difficult to predict. The mechanisms that lead to the seeding of these domains are unclear and exploring this aspect further is beyond the scope of this paper. After 30 minutes POPS/ Ca^{2+} domains start to form and expand across the SLB as the Ca^{2+} continues to flow.

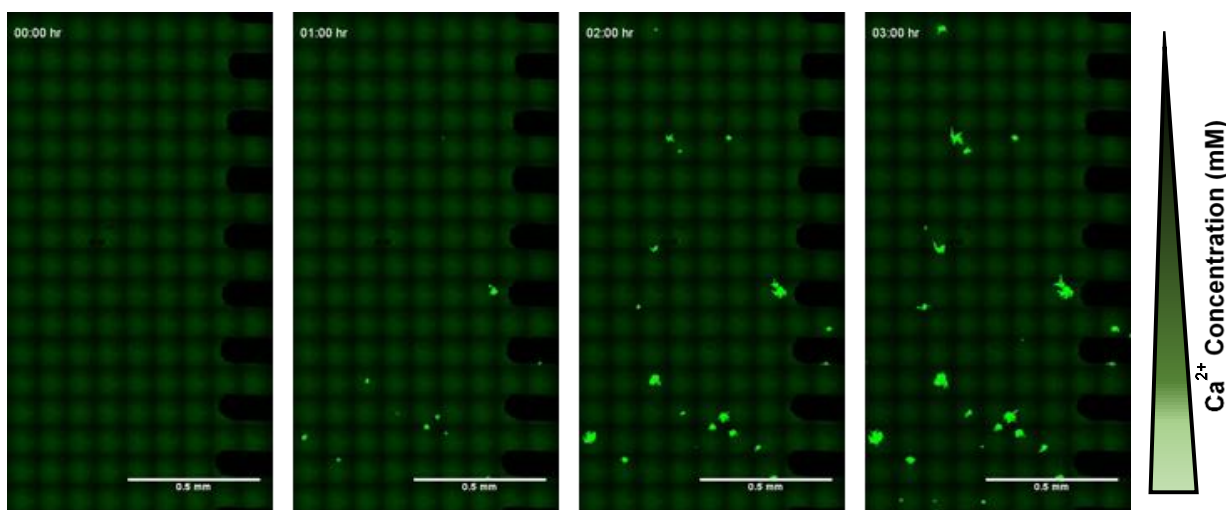


Figure 54. Montage of stitched TIRF images showing heterogeneous domain formation due to a Ca^{2+} gradient flowing over a homogenous SLB composed of 30%POPS/0.1%TopFlourPS/69.9%POPC. Each stitched image covers a range of 2.0 X 2.5mm, and this raster was carried once an hour for 3 hours (5 minutes total time to obtain a full stitched image). This experiment was repeated five times, where the domain formation is always biased towards the high Ca^{2+} concentration, yet it is difficult to determine exactly where the domains will appear within this high Ca^{2+} concentration range.

The domains form first in the regions with the higher Ca^{2+} concentration, and a gradient of domains across the channel remains as the experiment progresses. To further explore this phenomenon where a heterogeneous aqueous ligand can impart asymmetry on a homogenous SLB, we expanded these Ca^{2+} experiments to include lipid compositions of $\text{PI}(4,5)\text{P}_2$ and $\text{PI}(4,5)\text{P}_2/\text{Cholesterol}$.

Figure 55 is a montage of one image area over time for a 5% $\text{PI}(4,5)\text{P}_2$, 95% DOPC, 0.1% TopFlour $\text{PI}(4,5)\text{P}_2$ SLB. After 20 min of Ca^{2+} exposure, we see the membrane punctuated with small areas of high fluorescence intensity. We believe that this is the result of TopFlour $\text{PI}(4,5)\text{P}_2$ / $\text{PI}(4,5)\text{P}_2$ clustering due to the bridging effect of Ca^{2+} (Ca^{2+} induced $\text{PI}(4,5)\text{P}_2$ clustering has been previously reported by the Janmey group^{105, 106}). Like previous experiments, we obtained images by rastering the objective across the observation chamber and acquired an image at nine locations across the membrane perpendicular to the fluid flow. This process was repeated once every five minutes for an hour. Each position was compiled as a movie (see supplementary material) and analyzed in ImageJ. Since the domains for the $\text{PI}(4,5)\text{P}_2/\text{Ca}^{2+}$ interaction are significantly smaller than that was found for the PS/Ca^{2+} interaction, we present the data in a slightly different way. We selected domains by setting a threshold for the intensity to create a binary image where the high-intensity regions were domains, and the low-intensity regions were interpreted as background. Figure 56A shows the percent area covered by domains as a function of time and location within the chamber. Here we can see a dramatic increase in the percent area occupied by the $\text{PI}(4,5)\text{P}_2/\text{TopFlourPI}(4,5)\text{P}_2/\text{Ca}^{2+}$ domains. The domain area increases from 0 to 3% of

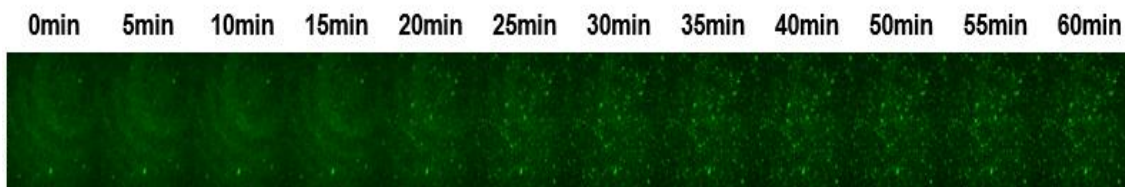


Figure 55. TIRF images for a single position showing domain formation due to the interaction of Ca^{2+} with a homogenous SLB composed of 5%PI(4,5) P_2 /0.1%TopFlourPI(4,5) P_2 /94.9%DOPC. The membrane was imaged once every 5min for an hour with a continuous flow of Ca^{2+} over the SLB. The high fluorescence regions appear after about 15-20 minutes. These high-intensity regions are thought to be due to the clustering of PI(4,5) P_2 and its fluorophores due to Ca^{2+} interaction (for better image quality, please see the movie in the supplementary material).

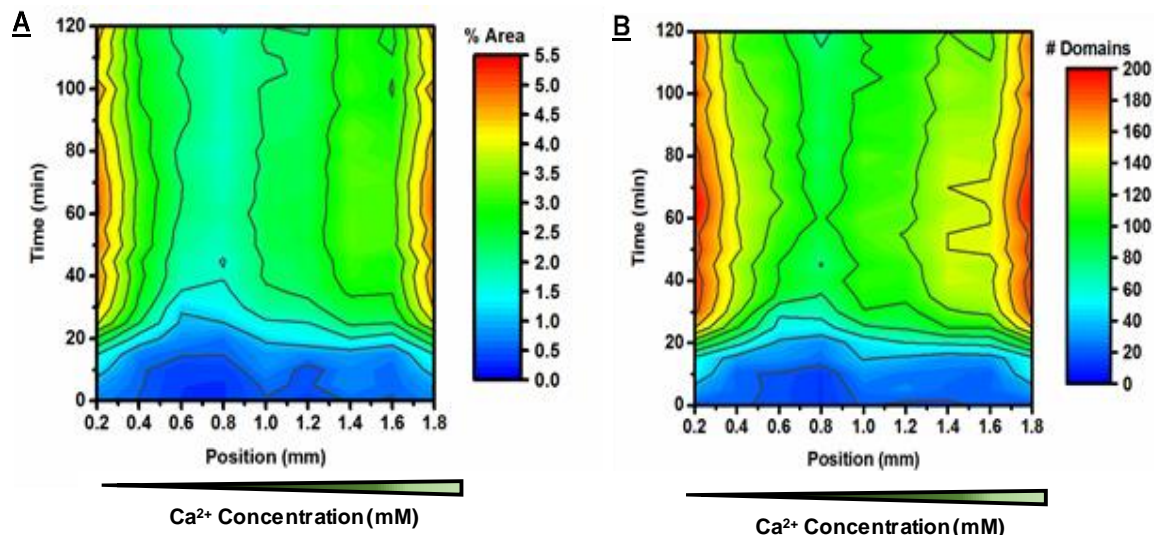


Figure 56. Temporal evolution of PI(4,5) P_2 domain formation upon interaction with a Ca^{2+} gradient. Images were obtained for a Ca^{2+} gradient flow over a homogenous SLB composed of 5%PI(4,5) P_2 /0.1%TopFlourPI(4,5) P_2 /94.9%DOPC. The original data set was acquired by rastering the objective across the 2 mm observation chamber perpendicular to fluid flow, taking a total of nine images once every 5 minutes for an hour. The raw images were analyzed in ImageJ software (A) Number of PI(4,5) P_2 %Area vs. time and location across the observation chamber (B) Domain number vs. time and location. To define a “domain”, for each image a threshold was set that distinguished the high-intensity areas from the background and then converted to a binary image. From this, each measurement compiled and the topology graphs constructed. Domains first appear at approximately 15 min after flow begins. By the end of the experiment, the domain number spans from about 100 to 400 domains. The number of domains as well as the area occupied by the domains is largest for the area with the highest Ca^{2+} concentration.

the total image. The highest percent domain area correlates with the highest Ca^{2+} concentration. Domain formation in the regions with the lower Ca^{2+} concentrations occurs later than it is observed for, the higher Ca^{2+} concentration regions. Figure 56B shows the number of domains counted at each position (heatmap) as a function of time (x-axis) and position (y-axis). This topology image shows that for all time points the largest number of domains are found in the regions with the highest Ca^{2+} concentrations. Domain formation starts at around 20 minutes and reaches a plateau at about 30 minutes. While domain formation in the areas with the lower Ca^{2+} concentration starts at the same time, the number of domains in these regions is significantly less than what is found in the areas with higher Ca^{2+} concentrations. The effects of the Ca^{2+} on PI(4,5)P₂ containing SLBs is evident by the spatiotemporal clustering of the PI(4,5)P₂ fluorophore in response to the Ca^{2+} gradient. In addition to this, we noticed edge effects in this experiment. The increase domains at the edge of the microfluidic device may be caused by the disruption of the speed of the lamellar flow at the wall of the PDMS. This could lead to a longer interaction between the Ca^{2+} and the PI(4,5)P₂ causing a more robust domain formation.

It is well documented that cholesterol aids in the formation of PI(4,5)P₂ domains in the absence and presence of Ca^{2+} ¹⁰⁷⁻¹⁰⁹. We would, therefore, expect that for the same experimental conditions as described above, the presence of cholesterol will cause domains to form faster and to grow to larger sizes. Figure 57 shows the development of PI(4,5)P₂/cholesterol domains upon interaction with Ca^{2+} for one image area as a function of time, while the data in Figure 58 illustrate the development of the PI(4,5)P₂/cholesterol domains upon interaction with a Ca^{2+} gradient. The Ca^{2+} has less impact on the

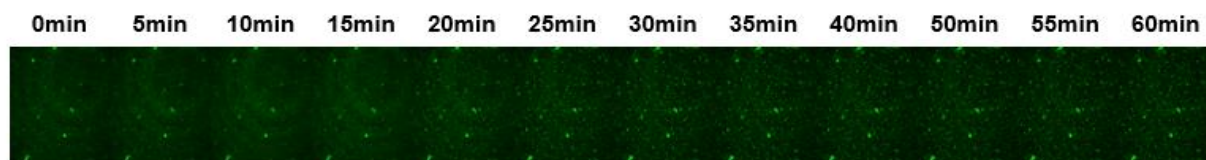


Figure 57. TIRF images for a single area showing domain formation due to the interaction of Ca^{2+} with a homogenous SLB composed of 5%PI(4,5) P_2 /0.1%TopFlourPI(4,5) P_2 /30%Cholesterol/64.9%DOPC. The SLB was imaged once every 5 min for an hour with a continuous flow of the Ca^{2+} gradient over the SLB. The high fluorescence regions appear after a period of 15min of Ca^{2+} flow. These high-intensity regions are thought to be due to the clustering of PI(4,5) P_2 /TopFlourPI(4,5) P_2 due to the interaction with Ca^{2+} . In comparison to the bilayer without cholesterol, there are more large domains at the start of the experiment. This is line with the hypothesis that cholesterol stabilizes these fluid PI(4,5) P_2 domains. (for better image quality, please see the movie in the supplementary material).

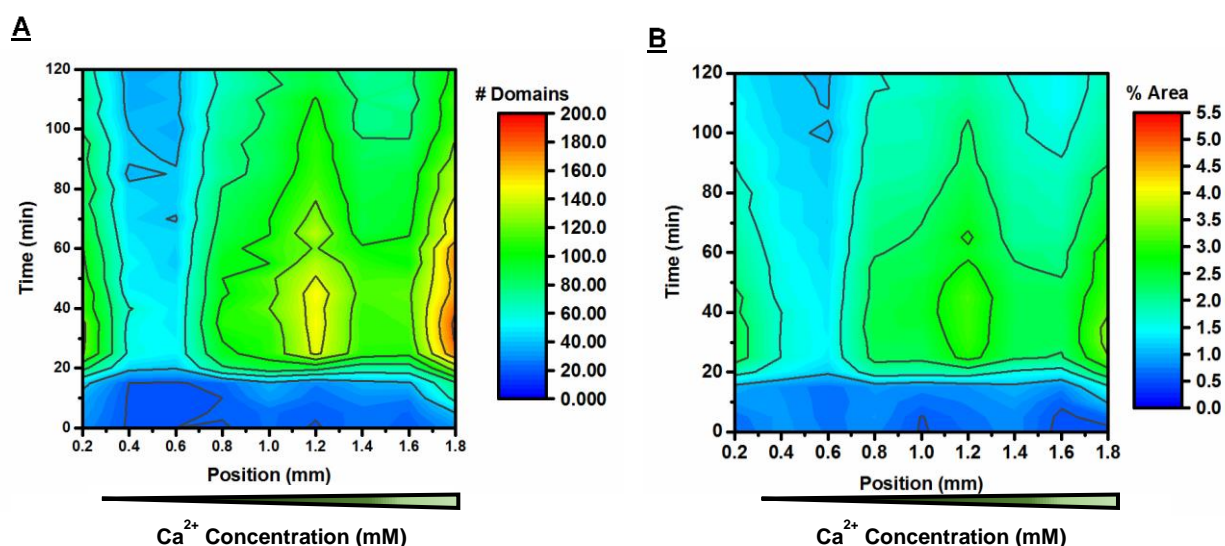


Figure 58. Temporal evolution of PI(4,5) P_2 /cholesterol domain formation upon interaction with a Ca^{2+} gradient. Images were obtained for a Ca^{2+} gradient flow over a homogenous SLB composed of 5%PI(4,5) P_2 /0.1%TopFlourPI(4,5) P_2 /30%Cholesterol/64.9%DOPC. The original data set was acquired by rastering the objective across the 2mm observation chamber perpendicular to fluid flow, taking a total of nine images once every 5 minutes for an hour. The raw images were analyzed in ImageJ software (A) Number of PI(4,5) P_2 /cholesterol domains vs. time and location across the observation chamber. (B) Percent domain area relative to the total field of view vs. time and location. To define a “domain”, for each image a threshold was set that distinguished the high-intensity areas from the background and then converted to a binary image. From this, each measurement compiled and the topology graphs constructed. Domains first appear at approximately 15 min after flow begins. By the end of the experiment, the domain number spans from about 100 to 400 domains. The number of domains as well as the area occupied by the domains is largest for the area with the highest Ca^{2+} concentration.

cholesterol/PI(4,5)P₂/DOPC SLB morphology (Figure 58) than that observed in the absence of cholesterol (Figure 55). For the cholesterol-containing SLB, PI(4,5)P₂ enriched domains can be seen even in the absence of Ca²⁺ (before the addition of Ca²⁺). In particular, for the regions with lower Ca²⁺ concentrations (1 mM and 2 mM Ca²⁺), where for the cholesterol-free SLB only moderate domain formation occurred, an increased number of domains are found. From a kinetic point of view, the plateau where no additional domain formation is observed is reached faster (about 25 minutes after the Ca²⁺ was introduced in the chamber, see Figure 58). Furthermore, there is less domain size disparity; without the cholesterol, the domain sizes ranged from 5 to 15 pixels, while in the presence of cholesterol the size range is 10 to 13 pixels. This is likely due to the domain stabilizing effects of cholesterol, which leads to larger domain size. The percent domain area plot shows for the SLB with cholesterol a shallower gradient as compared with PI(4,5)P₂ only. These results are in agreement with the earlier formulated hypothesis that cholesterol stabilizes PI(4,5)P₂ domains, i.e., while an additional PI(4,5)P₂ domain forming effect is observed in the presence of Ca²⁺, the impact of the Ca²⁺ on domain formation is less profound than in the absence of cholesterol^{108, 109}. The edge effects are also less pronounced in this experiment as compared to the former.

These three experiments, PI(4,5)P₂, PI(4,5)P₂/Cholesterol, and POPS (in a DOPC SLB) show domain formation as an effect of Ca²⁺ exposure. As expected, the extent of domain formation is highly dependent on the Ca²⁺ concentration as evidenced by the Ca²⁺ gradient dependent kinetics of anionic lipid domain formation. These experiments underscore the versatility of the microfluidic device because not only can we successfully produce lipid bilayers exhibiting a lipid gradient but it is also possible to expose a

homogenous bilayer to a gradient of a solute in the aqueous phase, which triggers a gradient specific response.

In addition to what has so far been discussed, we have discovered an unexpected but highly welcomed side effect of using the microfluidic device. SLBs that contain highly negatively charged lipids are usually challenging to form. We have found with our method that the microfluidic device helps with the SLB formation (fewer defects in comparison to more traditional methods¹¹⁰). We attribute this to the shear forces the vesicles experience as they are entering the observation chamber, which apparently leads to a better settling of the lipid bilayer onto the glass support. While we have not tested this exhaustively, we expect that the use of the microfluidic device will expand the scope concerning lipid composition, allowing us to conduct experiments with more complicated, physiologically relevant lipid compositions.

Despite the robustness of the experiments described above, we realize that the size of the observation channel is too large to accomplish one of our goals, which is to investigate lipid gradients at physiologically relevant length scales. The comparatively large size of the observation channel presents a two-fold problem. (1) From a logistical point of view, the experiments take far too long, over 24hrs, for the gradient to come to equilibrium. This not only limits throughput, but it also requires control of all experimental parameters (e.g., temperature) over quite long time periods. (2) Physiologically relevant length scales are in the range of tens of microns, while our observation chamber has a width of 2 mm. With this in mind, we fabricated a different microfluidic platform with a design based on a device developed by the Whitesides group⁹¹.

Figure 59 shows the design and dimensions of the microfluidic device with a tapered design. There are several choices of observation widths ranging from 900 μm down to 50 μm . The large size would be used for experiments where one wants to look at several frames of similar membrane composition, providing replicates of an experiment from a single microfluidic setup. The 100-micron and 50-micron size chambers are useful for studying effects in the SLB at length scales that are similar to large cells. Also at 100 μm , the entire channel can fit in the field of view of the microscope, making it unnecessary to stitch images together to acquire gradient information.

To test whether the gradient in the fluid phase is maintained throughout the entire device, we experimented with a fluorescein gradient (figure 55, a pure glass substrate with no SLB). The experiment was carried out at several different flow rates to illustrate how the steepness and functional form of the gradient can be manipulated. For the highest flow rates, the gradient assumes the form of a step function, while at slower flow rates the gradient is smooth. Most importantly, there is a gradient of fluorescein

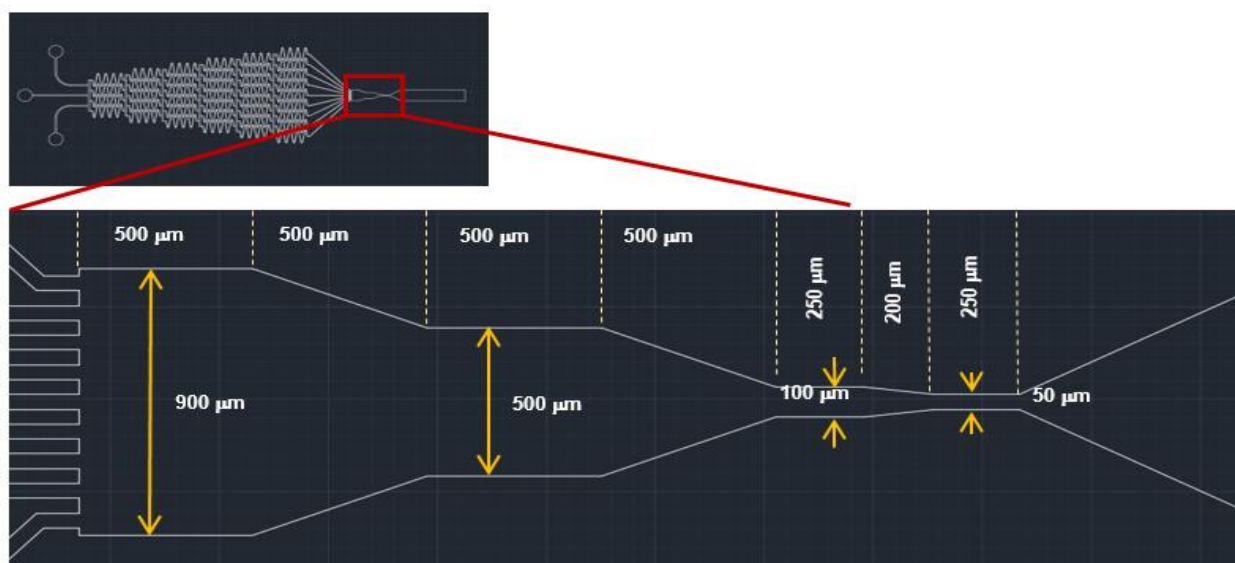


Figure 59. Microfluidic platform design with tapered features which allows to choose several different widths to explore gradients in artificial membranes. The smallest widths are at the maximal end of large cell diameters allowing us to conduct more physiologically relevant experiments.

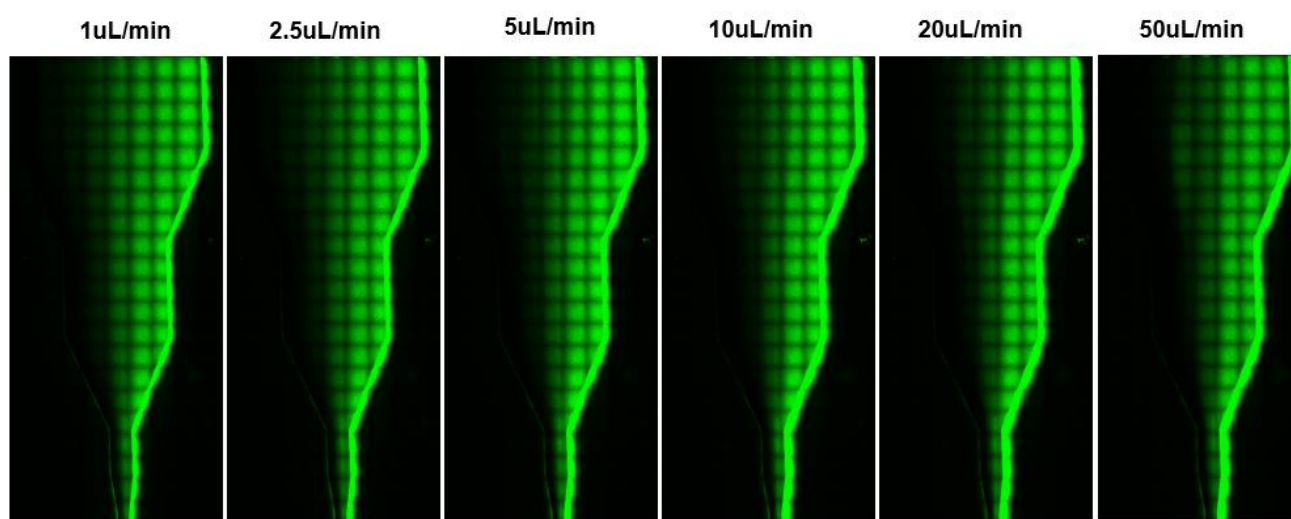


Figure 60. TIRF images of a fluorescein gradient flowing through the tapered microfluidic device at different flow rates. Despite the tapered design, the gradient in the aqueous phase is maintained. These experiments highlight the effect of the flow rate on the steepness of the gradient. For the slowest flow rate the gradient is smooth and integrated, while for high flow rates the fluorescence intensity has the form of a step

throughout the entire tapered design, even in the last compartment with the smallest dimension (Figure 60 and Figure 61). As the last step, we tested the tapered design by performing the TopFluor® PI(4,5)P₂ SLB insertion experiment in the same way as described above for the conventional microfluidic device. Figure 62 shows two images from the beginning and end of a movie showing TopFluor®PI(4,5)P₂ inserting as a gradient (see supplementary material for the movie). The gradient comes to equilibrium corresponding to the size of the channel, i.e., the smallest channel equilibrates quickest (~10 min), while for the largest channel it takes the longest (~10 hrs). With this design, we now have access to PI(4,5)P₂ gradients on membranes with physiological dimensions and realistically testable time spans (Figure 62 and 63).

4.5 Conclusions and Outlook with the microfluidic platform

Cells have micron scale control over their plasma membrane morphology as seen by the formation of lipid and protein gradients during processes like chemotaxis or cytokinesis. We have developed a device that enables the fabrication of solid-supported

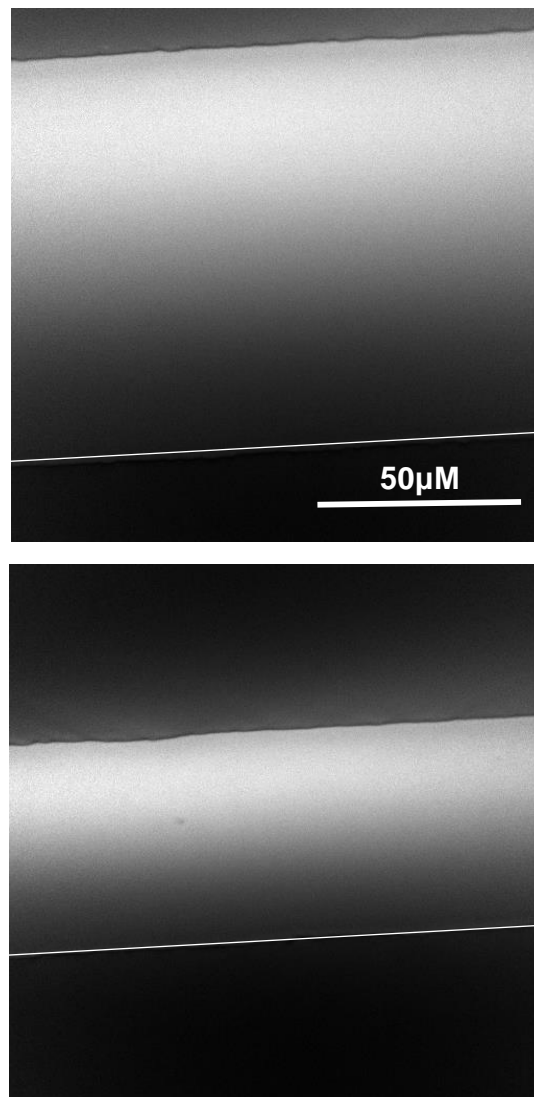


Figure 61. Image of the fluorescein gradient in the two narrowest chambers. The gradient is well maintained throughout the entire microfluidic device.

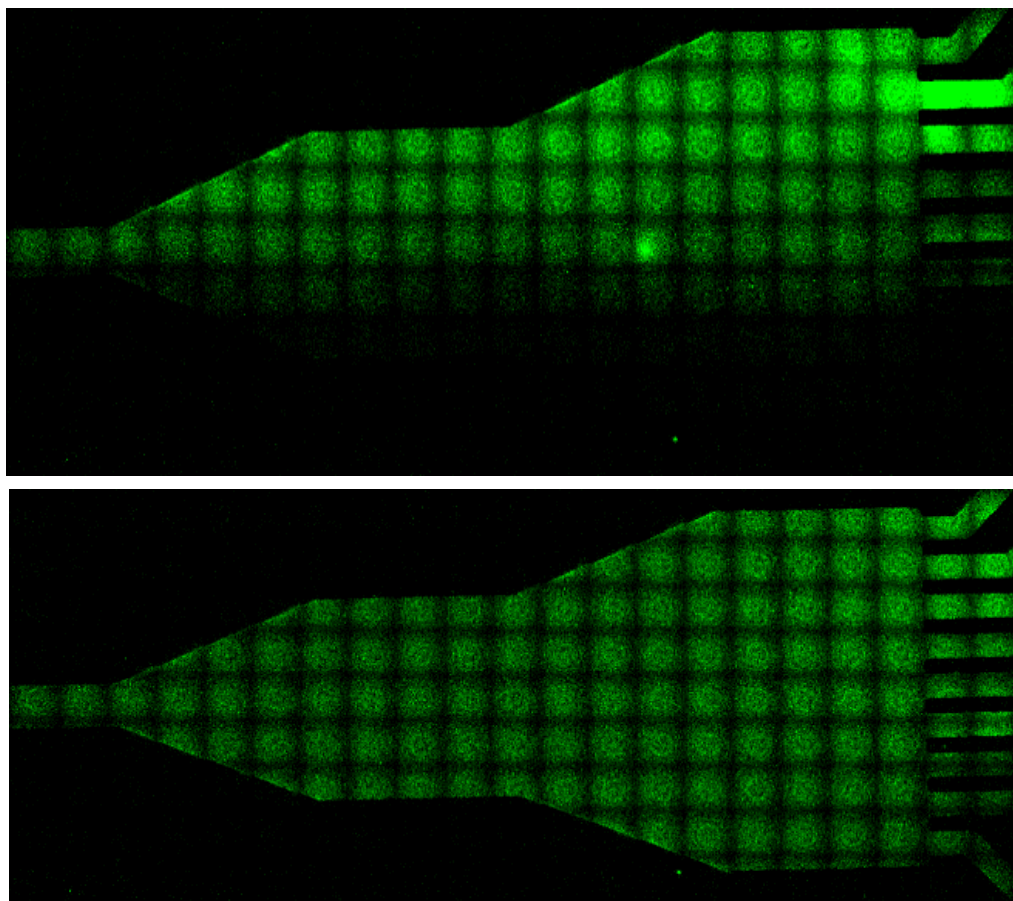


Figure 62. Shows the first TIRF stitch image of TopFlourPI(4,5)P₂ inserted as a gradient in SLB composed of DOPC and the final image after the PI(4,5)P₂ gradient comes to equilibrium.

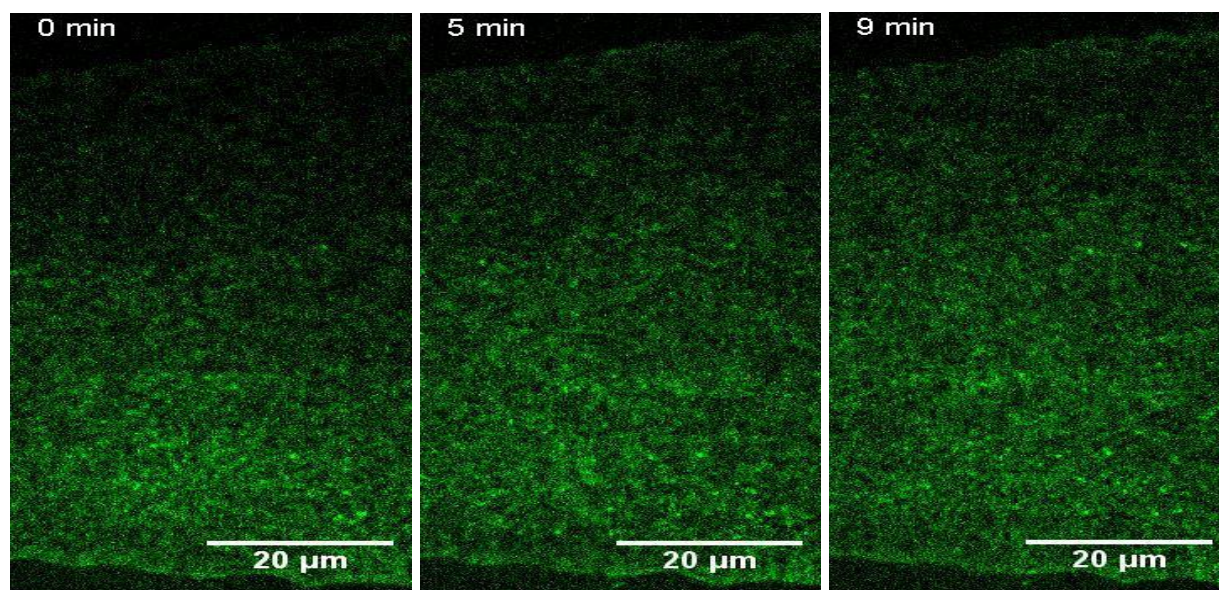


Figure 63. Is the zoomed in area montage of the TopFlourPI(4,5)P₂ experiments showing the gradient in the narrow chambers.

lipid bilayers that exhibit a lateral gradient concerning their lipid composition. Also, we have shown that we can elicit a gradient specific response in a homogenous lipid bilayer when this bilayer is in contact with a fluid that exhibits a gradient of one or more of its components.

We have successfully generated a PI(4,5)P₂ gradient which is testable and robust. We can make the SLB *in situ* on the TIRF microscope by either floating monomeric lipid molecules over the preformed SLB or by laying down vesicles that exhibit differences in lipid composition. Ca²⁺ gradient-dependent domain formation on PI(4,5)P₂, PI(4,5)P₂/Cholesterol, and PS-containing membranes illustrates that we can elicit a gradient specific response when a homogeneous SLB is exposed to an appropriate gradient in the fluid phase. This opens up the opportunity to use a gradient of protein, e.g., a lipid-modifying enzyme, in the fluid phase and to study the spatiotemporal response in the lipid bilayer. With the most recent iteration of our platform, we can generate a gradient on length scales typical for large cells.

In the future, we plan to use this platform to quantitatively ascertain the stochastic balance between the phosphatase PTEN and the kinase PI3K as these proteins interact with a PI(4,5)P₂ containing bilayer. We hope to fill gaps in the current mechanistic understanding of motility and cancer metastasis work. Such dynamic protein competition on laterally non-homogeneous SLBs, as we have developed in this study, would be a highly interesting target to investigate.

5.0 Future Directions

5.1 Kinetics Experiments

The next place to take this work is the further development of the global fit model. Experiments done with lipid mixtures of PI/cholesterol and PI(4,5)P₂/cholesterol would further establish the effects of lipid domains on PTEN membrane binding. These domains, in contrast to PI(4,5)P₂/PI, cluster the phosphoinositide without the addition of charge. This allows us to explore the effects of the spatial density of PI(4,5)P₂ without adjusting the overall potential of the lipid vesicle. A question one would ask is which lipid composition, 5%PI(4,5)P₂ or 5%PI(4,5)P₂/cholesterol, has the faster rate constant. If the trends continue with what we have observed, it would be expected that 5%PI(4,5)P₂/cholesterol would have a slower k_{on} but also have a more stable interaction (slower k_{off}). In this case, what is the determining factor, is the k_{off} so slow that it effects the K_d resulting in a net increase of PTENs on the lipid vesicle? Or, is the protein crowding competitive enough that the increased stability has little effect, i.e there are too few binding sites to be useful.

Exploration with the stopped-flow of different domain constructs of PTEN would expand the kinetic story. These data could also be used to validate the single-molecule results. With the C2 domain a different FRET pair would have to be constructed since there is no tryptophan occurring in the sequence. Since the ybbR tag is already present, this should be a simpler route than re-cloning the protein with tryptophan. To continue to parse out the effects of specific binding, mutations studies of PTEN at sites such as H93 should be undertaken. Data with these disease constructs would continue to develop the understanding of the diseased phenotypes and new therapeutic pathways would be

revealed. In addition to this experiments with wtPTEN and mixed PI(5)P/ PI(4)P could also be informative. It would be interesting to see if these phosphoinositides would induce a second step or not in the kinetic data. In addition, would there be a change in the diffusion coefficients, indicating a decreased protein-lipid interaction, or would the population distribution shift?

This thesis is as much about PTEN and lipids as it is about *how* to describe proteins binding to these dynamic surfaces. We argue that a protein binding to a negatively charged membrane can use both electrostatics and a bi-molecular approach. For every example of a protein interacting with a membrane due to pure electrostatics (MARCKS) there is one where the chemistry matters (PH domains). Conceptually it is easy to say, the protein feels the electrostatic field which drives it to the membrane through the electrostatic double layer to have an interaction with the lipid membrane. At some point during this process peptides seem to behave as if interacting with individual lipids rather than “*just*” a negatively charged surface. A barrier to determining the true k_{on} value is how do you count the lipids to appropriately describe the bimolecular model? Conversely, one could account for the complex stability by reporting the k_{off} values, which are concentration independent. A simple investigation that needs to be explored is to find the experimental dissociation constant. We have available to us the reagents and the equipment. By finding these values they can be directly inserted in the KinTeK global fit program while allowing the others values to float. This would allow for the exploration of other models with multiple steps (Figure 48). In addition, these values can be used to validate the single molecule dwell time results above.

The more sophisticated solution is an investigation of single molecule kinetics. It would be very interesting if single molecule FRET could be designed to directly probe the PI(4,5)P₂ and PTEN interaction. If it is possible to get a high enough signal with TIRF you could quantify the amount of free donor vs. FRET. Since all of the PTEN that we can see is bound to the membrane, we would observe the “electrostatic” PTEN vs. “PI(4,5)P₂-bound PTEN. Both the life-times of each species would be informing with how proteins deal with complex lipid surfaces. How would the relationship change with lipid domain containing supported lipid bilayers?

In addition to this, the cumulative dwell times can also be fit in the global fit software. In combination with the ensemble experiments we could define a detailed, complex protein-membrane interaction. Ultimately, if these experiments are expanded to other phosphoinositide metabolizing/interacting proteins would we uncover a generalized mechanism. Do other phosphoinositide binding proteins use this coincidence detection and multimodal membrane interactions as a means to scan biological surfaces efficiently? How does this change in disease and is there a way to rescue the diseased membrane surface?

5.2 Microfluidics

The next step in the microfluidic device project is to explore the effects of proteins on these membranes. The first thing I would do is acquire a labeled PH domain specific for PI(3,4,5)P₃ and see if we could see a gradient of these lipid through the PH domain binding. Once that is established I would flow PTEN as a homogenous solution over a lateral gradient of PI(3,4,5)P₃ and follow the catabolism of the phosphoinositide as a function of the loss of the PH domain. It would be interesting to follow the turnover with

different membrane compositions and explore the rate of the lateral gradient decay. After this system was well established I would explore this with PI3K and then have a competition experiment between the kinase and the phosphatase. It would also be interesting to design an even narrower microfluidic chamber (10-5 microns) and see if stochastic effects begin to dominate the averaging behavior. Since those sizes are cellular dimensions, it may lead to unique insights on how these enzymes behave on a complex membrane surface.

List of Figures

Figure 1. The classic fluid mosaic model of the plasma membrane developed by Singer and Nicolson.

Figure 2. The chemical variability of phospholipids is due to the rich functionality of the molecule.

Figure 3. There are seven members of the phosphoinositide family.

Figure 4. The rarity of the phosphoinositides belies their importance.

Figure 5. PI3K-Akt signaling pathway and PTEN's regulatory role in humans.

Figure 6. The structure of PTEN.

Figure 7. The hypothesis model of PTEN interacting with complex model membranes.

Figure 8. FRET transfer between PTEN W247 and dansyl-PE when PTEN binds to a vesicle composed of 5% PI(4,5)P₂, 2% DansylPE, 93% PC.

Figure 9. Comparison of PTEN binding to vesicles with different mixed lipid compositions.

Figure 10. Stopped-flow dansyl-PE fluorescence intensity curves upon PTEN binding to mixed PI/PC vesicles.

Figure 11. General graph showing the difference between a rate limited, two-step reaction (red), and a one-step reaction (blue).

Figure 12. Rate constant k_{obs} as a function of lipid concentration, (anionic component), of vesicles composed of 30%PI 2%DansylPE, 68%PC.

Figure 13. Comparison of k_{on} rates derived from the analytical method using total surface lipid concentration in the analysis of PTEN binding to mixed lipid systems.

Figure 14. Comparison of the anionic component k_{on} derived from the analytical method of PTEN binding to lipids.

Figure 15. Comparison of the charged normalized k_{on} derived from the analytical method of PTEN binding to lipids.

Figure 16. Comparison of the k_{on} values when using the target lipid concentration for the kinetic analysis method of PTEN binding to lipids.

Figure 17. Comparison of the k_{off} values derived from the analytical method (Figure 12, eq. 3) of PTEN binding to lipids.

Figure 18. K_d values of PTEN binding to various vesicles (total lipid concentration).

Figure 19. K_d values of PTEN binding to vesicles analyzed by using only the anionic lipid concentration.

Figure 20. Compares the K_d values of PTEN binding vesicles analyzed by total valence contribution.

Figure 21. Compares the K_d values of PTEN binding to vesicles analyzed by target lipid concentration.

Figure 22. An example of a single component fit.

Figure 23. An example of a two-component fit of the stopped-flow spectrophotometric data.

Figure 24. The compilation of all the global fit rates by step of PTEN mixed with multicomponent model vesicles.

Figure 25. The Kds calculated for each reaction step.

Figure 26. Selection of the radius in the Mosiac plugin is an important step in determining real particles from spurious detections.

Figure 27. The distribution of of the track NpScore plotted against frames.

Figure 28. The intensity filter plots the mean intensity of the trajectory against how many frames the tracked particle exists for.

Figure 29. The diffusion filter is the final exclusion test placed upon the data set.

Figure 30. Particle tracking of wtPTEN interacting with PI(4,5)P₂/DOPS/DOPC solid supported lipid bilayers.

Figure 31. The PTEN population as a function of displacement after 90ms.

Figure 32. Velocity graphs of wtPTEN interacting with 3% PI(4,5)P₂/ 30%DOPS/ 70%DOPC SLBs.

Figure 33. Example tracks determined from the diffusion coefficients from the previous figure.

Figure 34. Diffusion coefficients of wtPTEN on various model membranes determined by the analysis described above

Figure 35. The population of wtPTEN on various model membranes determined by the analysis described above.

Figure 36. Diffusion of the delPTEN (PBD deleted) construct of various lipid membranes.

Figure 37. The population of delPTEN on various model membranes determined by the analysis described above.

Figure 38. Diffusion of the PTEN C2 domain on various model membranes determined by the analysis described above.

Figure 39. The population of PTEN C2 domain on various model membranes determined by the analysis described above.

Figure 40. This schematic summarized the diffusion results in terms of bound lipid.

Figure 41. Culmative distribution of dwell times of wtPTEN on 30%PS/3%PI(4,5)P₂.

Figure 42. Rate constants of wtPTEN on SLB with the compositions 3% PI(4,5)P₂/30% PS , 3% PI(4,5)P₂,and 30%PS.

Figure 43. The rate population of wtPTEN on SLB with the three stated lipid compositions.

Figure 44. Dissociation rate constants of delPTEN interacting with SLBs with the compositions 3% PI(4,5)P₂/30% PS , 3% PI(4,5)P₂,and 30%PS.

Figure 45. The dissociation rate populations of delPTEN on SLBs with the three stated lipid compositions.

Figure 46. Dissociation rate constants of PTEN's C2 domain interacting with SLBs that have the compositions 3% PI(4,5)P₂/30% PS , 3% PI(4,5)P₂,and 30%PS.

Figure 47. The rate populations of PTEN's C2 domain interacting with SLBs with the three stated lipid compositions.

Figure 48. A model to account for the ensemble and single molecule results. First PTEN approaches the membrane due to the negative potential from the lipids.

Figure 49. Wide-field fluorescence image of the microfluidic gradient generator with a homogenous SLB composed of DOPC and 1%RhodaminePE.

Figure 50. The setup of the microfluidic platform on the TIRF microscope.

Figure 51. TopFluorPI(4,5)P₂ gradient in a homogeneous DOPC bilayer labeled with Rhodamine PE.

Figure 52. Temporal evolution of the PI(4,5)P₂ gradient in the DOPC SLB. It takes over 22hrs for the TopFluorPI(4,5)P₂ gradient to equilibrate across the 2 mm chamber.

Figure 53. Gradient of PI(4,5)P₂ obtained using vesicles with different PI(4,5)P₂ concentrations.

Figure 54. Montage of stitched TIRF images showing heterogeneous domain formation due to a Ca²⁺ gradient flowing over a homogenous SLB composed of 30%POPS/0.1%TopFlourPS/ 69.9%POPC.

Figure 55. TIRF images for a single position showing domain formation due to the interaction of Ca²⁺ with a homogenous SLB composed of 5%PI(4,5)P₂/0.1%TopFlourPI(4,5)P₂/94.9%DOPC.

Figure 56. Temporal evolution of PI(4,5)P₂ domain formation upon interaction with a Ca²⁺ gradient.

Figure 57. TIRF images for a single area showing domain formation due to the interaction of Ca^{2+} with a homogenous SLB composed of 5%PI(4,5)P₂/0.1%TopFlourPI(4,5)P₂/30%Cholesterol/64.9%DOPC.

Figure 58. Temporal evolution of PI(4,5)P₂/cholesterol domain formation upon interaction with a Ca^{2+} gradient.

Figure 59. Microfluidic platform design with tapered features which allows to choose several different widths to explore gradients in artificial membranes.

Figure 60. TIRF images of a fluorescein gradient flowing through the tapered microfluidic device at different flow rates.

Figure 61. Image of the fluorescein gradient in the two narrowest chambers. The gradient is well maintained throughout the entire microfluidic device

Figure 62. Shows the first TIRF stitch image of TopFlourPI(4,5)P₂ inserted as a gradient in SLB composed of DOPC and the final image after the PI(4,5)P₂ gradient comes to equilibrium.

Figure 63. Is the zoomed in area montage of the TopFlourPI(4,5)P₂ experiments showing the gradient in the narrow chambers.

List of Tables

Table 1. The number of proteins containing these domains was gathered by using the SMART database.

Table 2. COSMIC database results of PTEN point mutations for different tumor tissues.

Table 3. Thermodynamically determined Kds of PTEN binding to multicomponent lipid vesicles³⁵.

Table 4. A comparison of the global fit ensemble k_{off} results with the single-molecule k_{off} results.

Appendix

Procedure for the BioRade FPLC:

- (1) HPLC water 20 mL at 2mL/min.
- (2) Stripping Buffer (20 mM HEPES pH 7.5, 500mM NaCl, 50mM EDTA).10mL at 1mL/min.
- (3) HPLC water 20mL at 2mL/min.
- (4) NiSO₄ (100mM) 3mL 1mL/min.
- (5) HPLC water 20mL at 2mL/min.
- (6) Equilibration Buffer (20 mM HEPES pH 7.5, 500 mM NaCl, 5mM Imidazole, 10 mM B-ME) 20mL at 2mL/min.
- (7) Lysis Supernatant 1mL/min until full volume is gone.
- (8) Equilibration Buffer 20mL at 2mL/min.
- (9) Elution Buffer (20 mM HEPES pH 7.5, 500 mM NaCl, 500mM Imidazole, 10 mM B-ME) 10mL at 1mL/min.
(Collect the elution which corresponds to the 280nm peak.)
- (10) HPLC water 20mL at 2mL/min.
- (11) 20% Ethanol 20mL at 2mL/min and store column at 4 °C.

The protein is then dialyzed overnight in 1L of (150 mM NaCl 20mM HEPES pH 7.5, 10 mM B-ME). Then the solution is passed over a Chitin column and an HiTrap Q HP anion exchange column.

The procedure for the chitin column with 1 mL of slurry wash with:

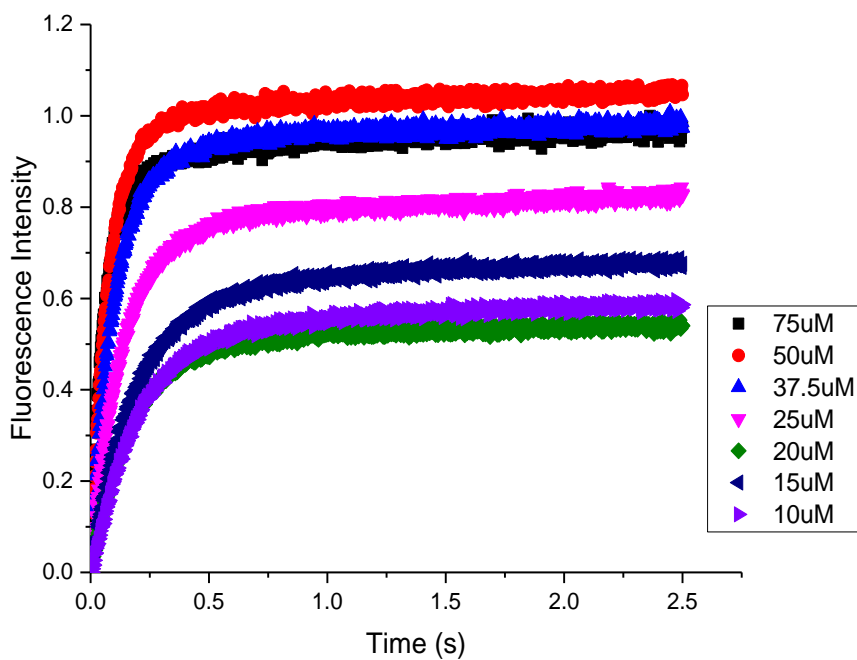
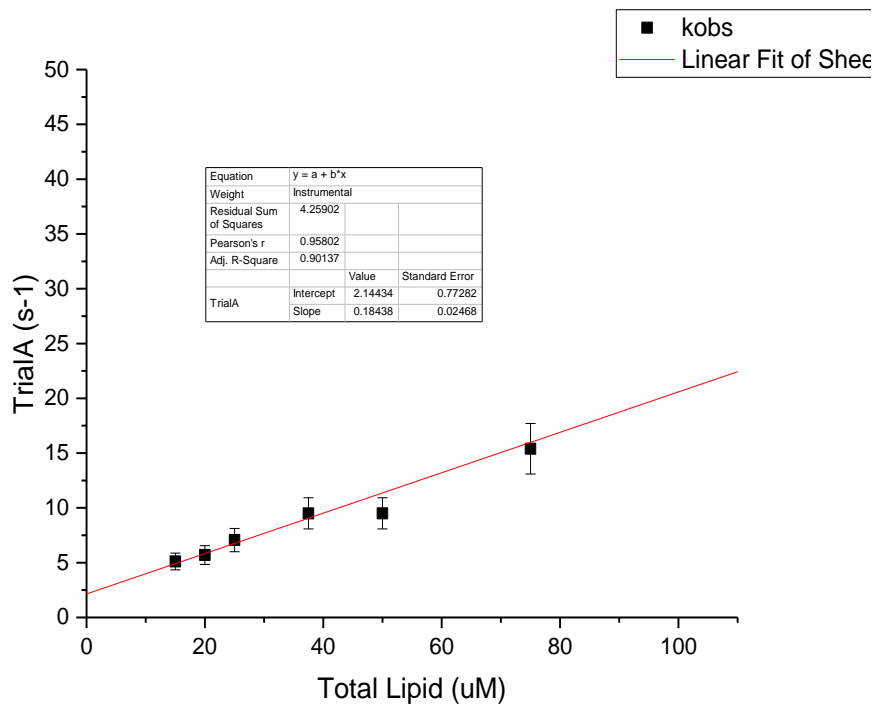
- (1) HPLC water 30 mL.
- (2) Dialysis Buffer 30 mL.
- (3) Cap the bottom of the column, add protein solution, cap top of the column and mix for 30min.
- (4) Collect flow through from Chitin column.
- (5) Add three mL of dialysis buffer and collect with protein sample.
- (6) HPLC water 30 mL.
- (7) 0.3M NaOH 10 mL. Cap bottom and top and mix overnight.
- (8) HPLC water 30 mL.
- (9) 20% ethanol solution 30 mL and store at 4 °C.

The final purification step occurs with the 1 mL HiTrap Q HP column (GE) on the FPLC.

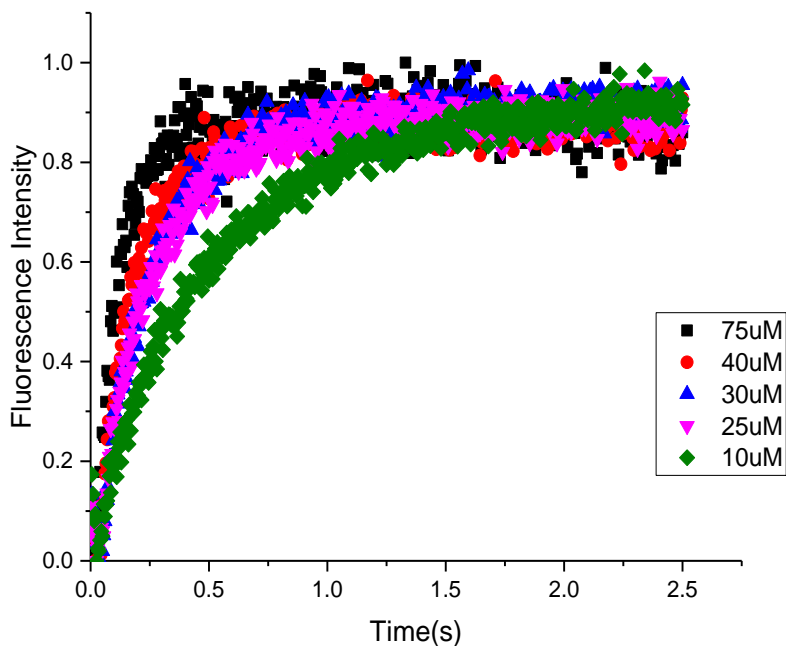
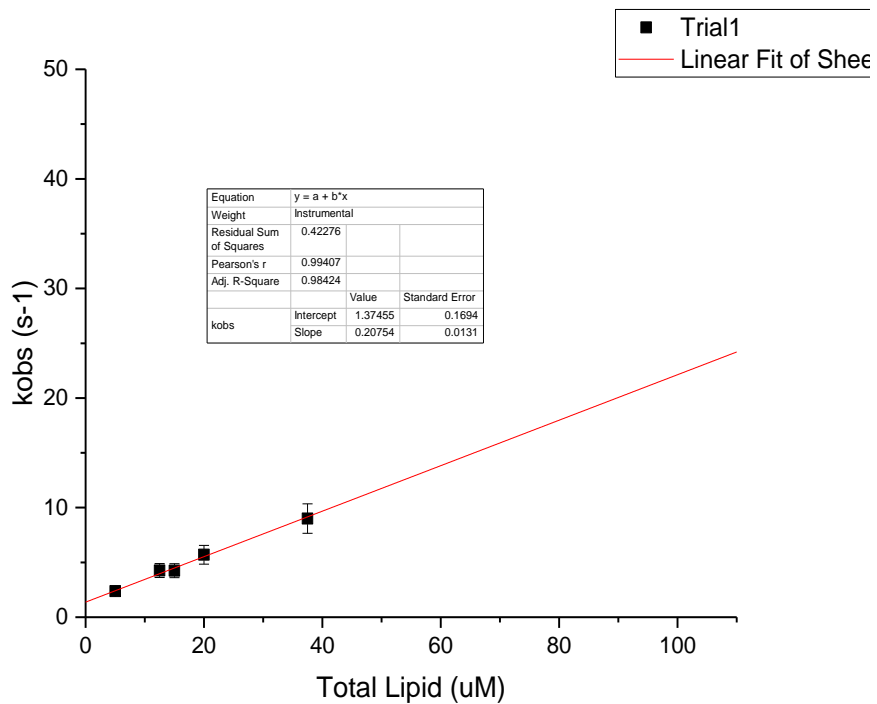
The procedure is as follows:

- (1) HPLC water 20 mL at 2mL/min.
- (2) High Salt (1 M NaCl, 20 mM HEPES pH 7.5, 10 mM B-ME) 20 mL at 2mL/min.
- (3) Low Salt (150 mM NaCl, 20 mM HEPES pH 7.5, 10 mM B-ME) 20 mL at 2mL/min.
- (4) Pass flow through from Chitin column (protein) at 0.5mL/min.
- (5) Low Salt 20 mL at 1mL/min.

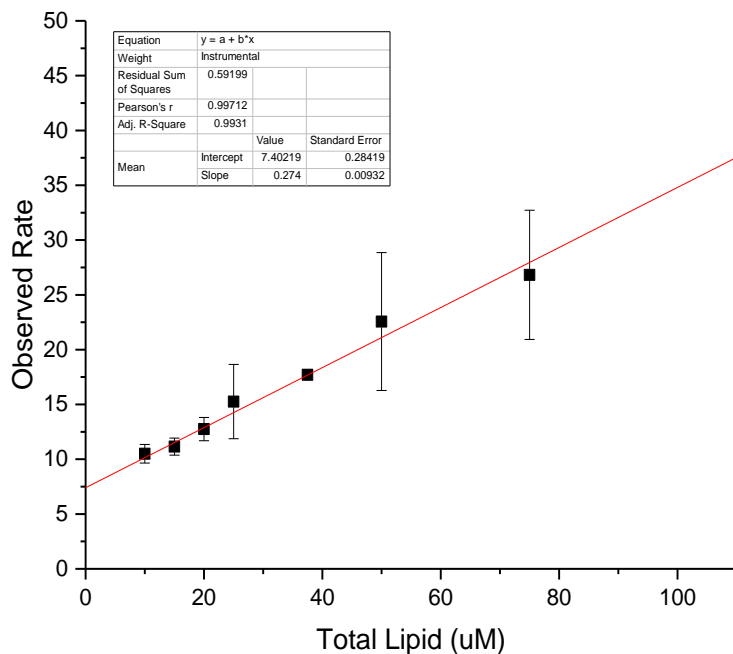
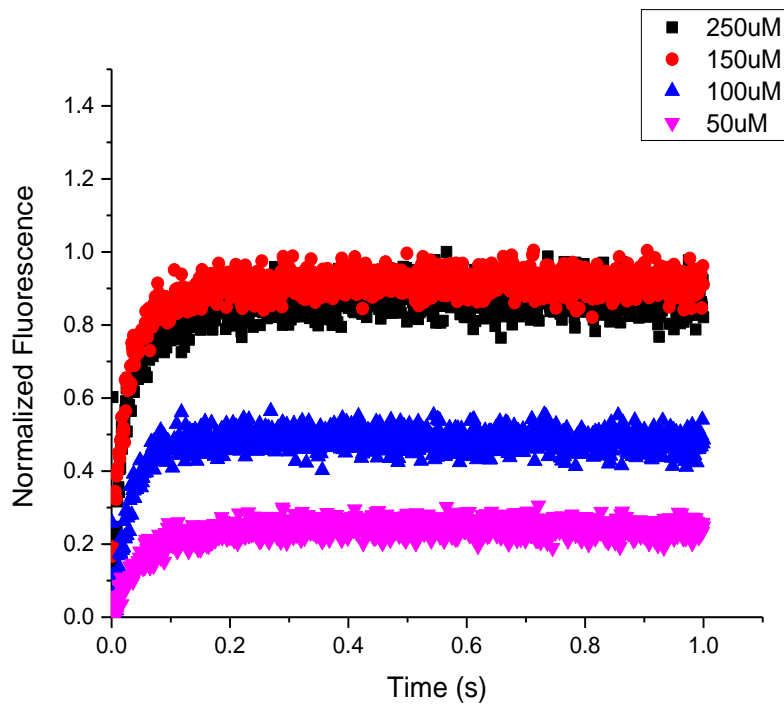
- (6) Gradient Low Salt to High Salt 60mL at 1mL/min. PTEN elutes 17mS-27mS.
Collect 12X 1mL fractions and run a SDS PAGE gel to determine the purest, highest concentration fractions.

Stopped-flow

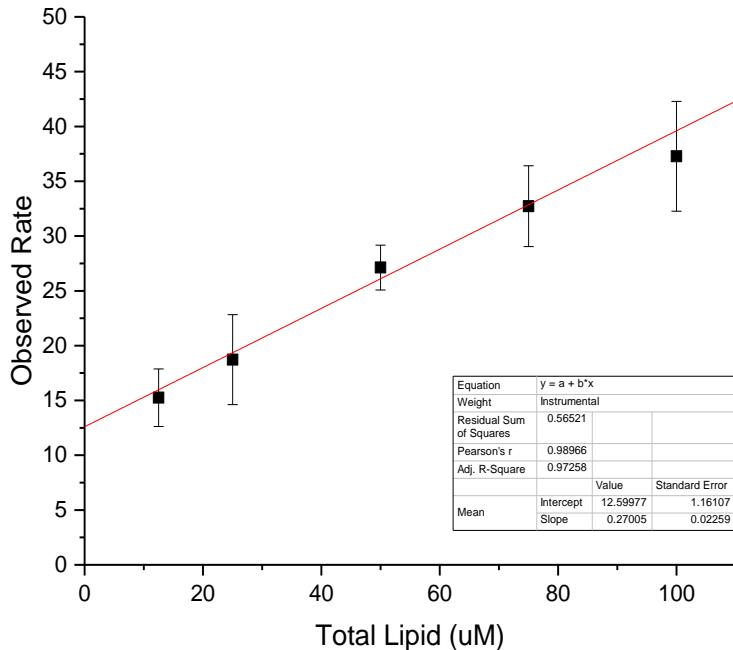
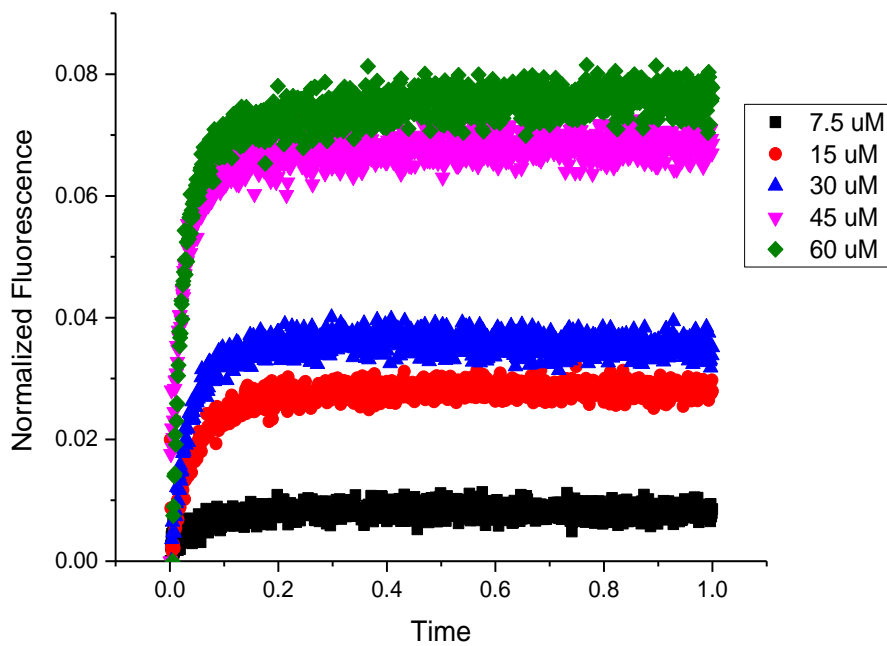
98% PS stopped-flow raw data. Top graph is the analytical graph used to determine on and off rates of PTEN binding to mixed vesicles. Bottom graph is an example of the raw data used in the graph above and the global fit.



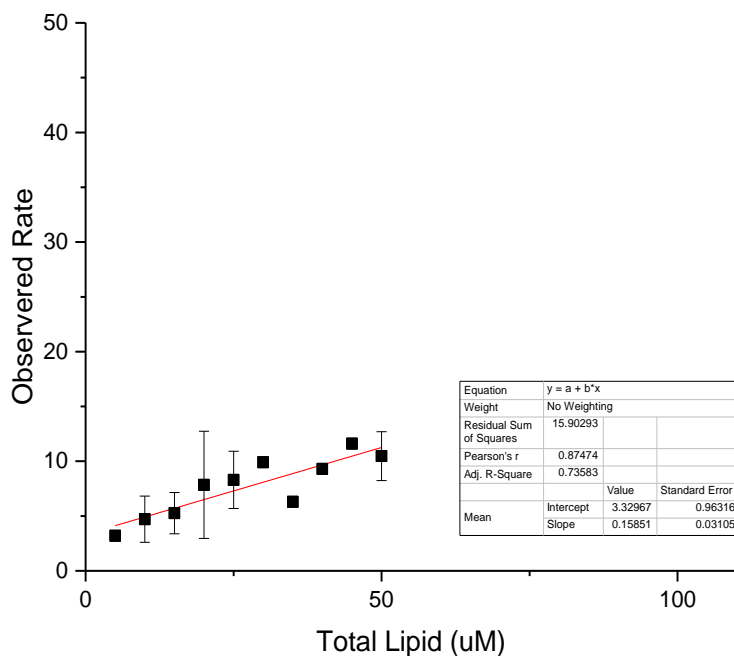
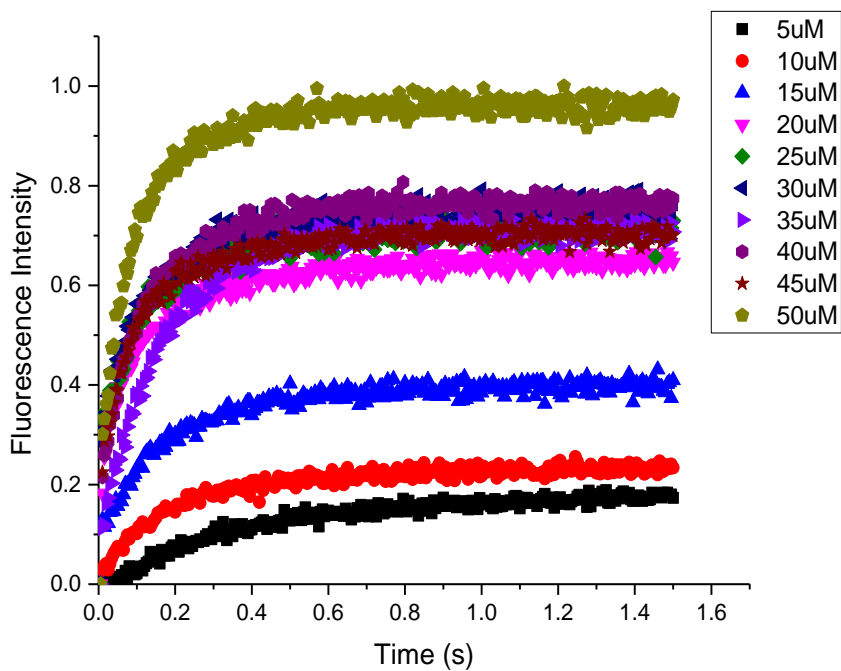
98% PI stopped-flow raw data. Top graph is the analytical graph used to determine on and off rates of PTEN binding to mixed vesicles. Bottom graph is an example of the raw data used in the graph above and the global fit.



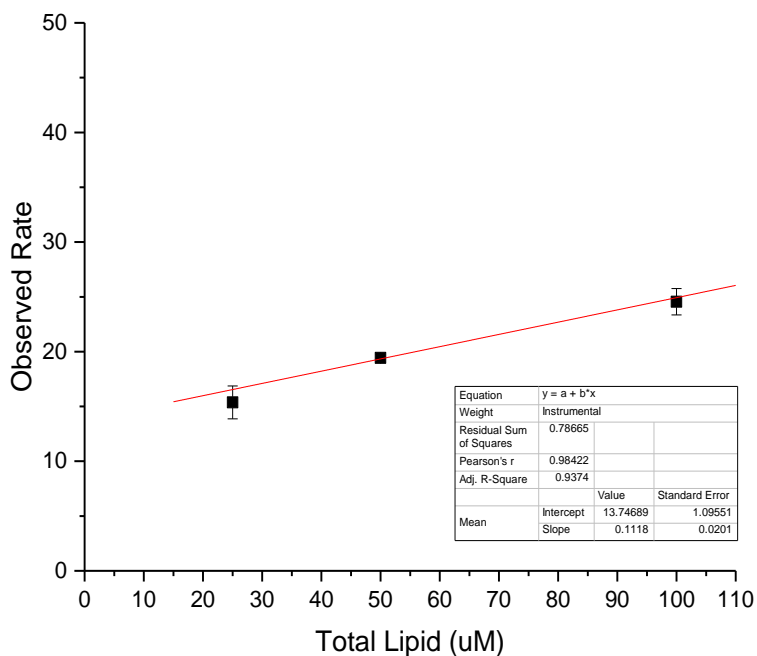
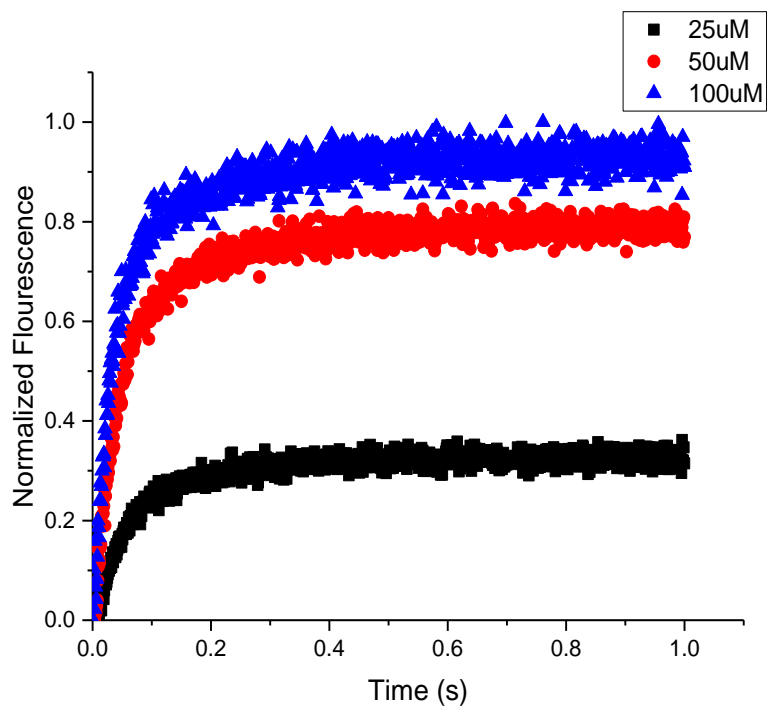
30% PS stopped-flow raw data. Top graph is the analytical graph used to determine on and off rates of PTEN binding to mixed vesicles. Bottom graph is an example of the raw data used in the graph above and the global fit.



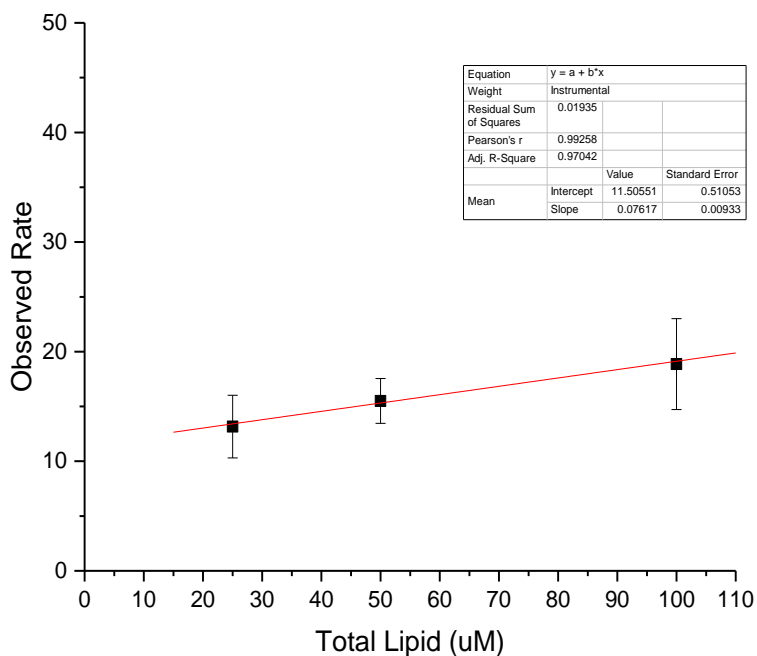
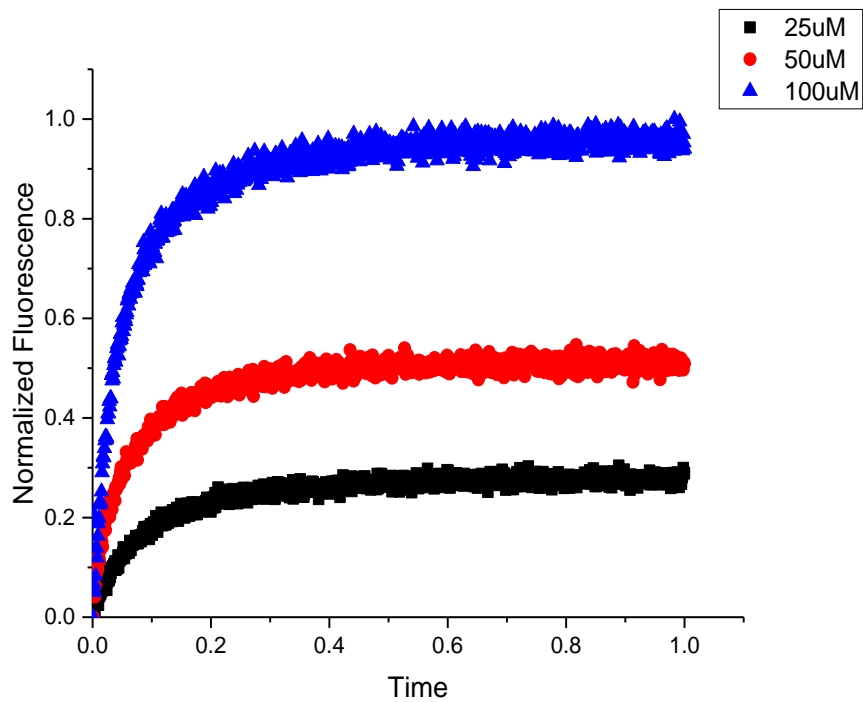
30% PI stopped-flow raw data. Top graph is the analytical graph used to determine on and off rates of PTEN binding to mixed vesicles. Bottom graph is an example of the raw data used in the graph above and the global fit.



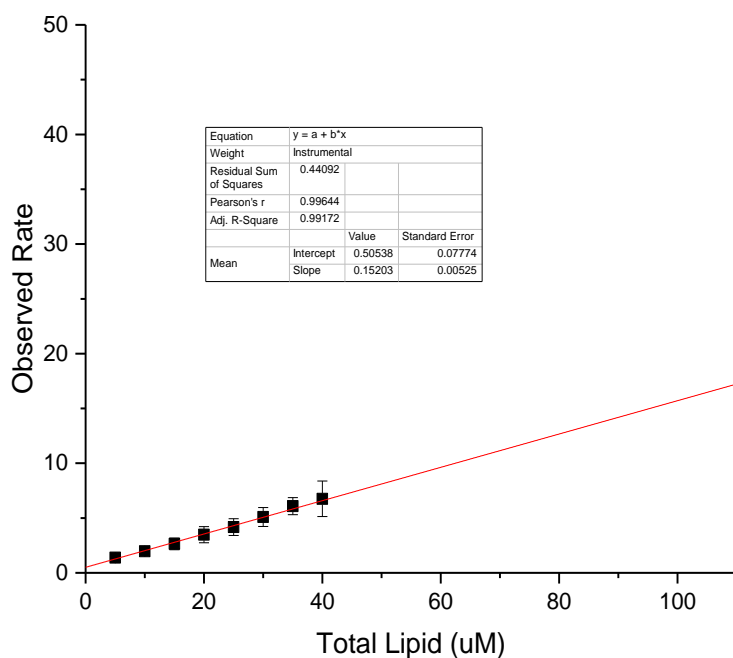
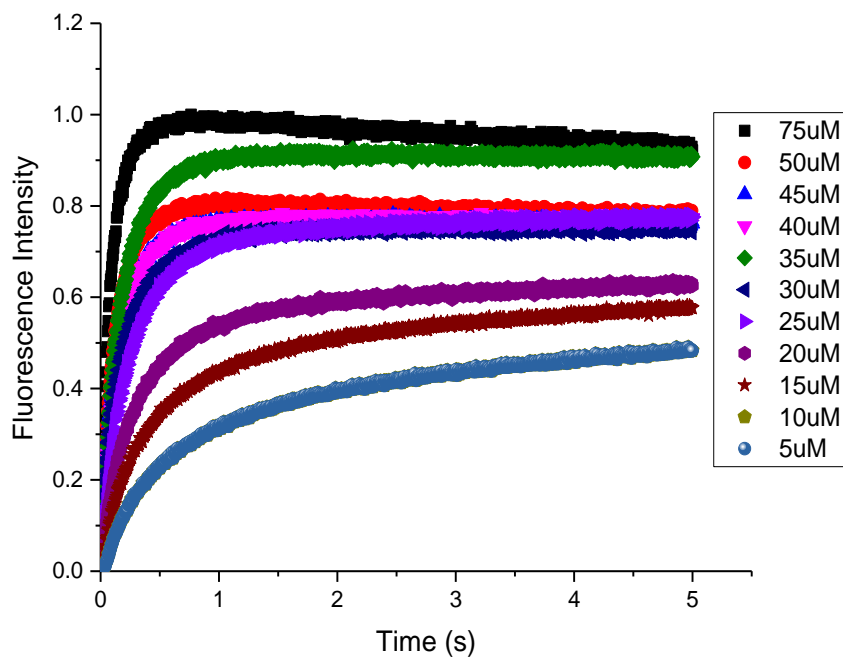
5%PI(4,5)P₂ stopped-flow raw data. Top graph is the analytical graph used to determine on and off rates of PTEN binding to mixed vesicles. Bottom graph is an example of the raw data used in the graph above and the global fit.



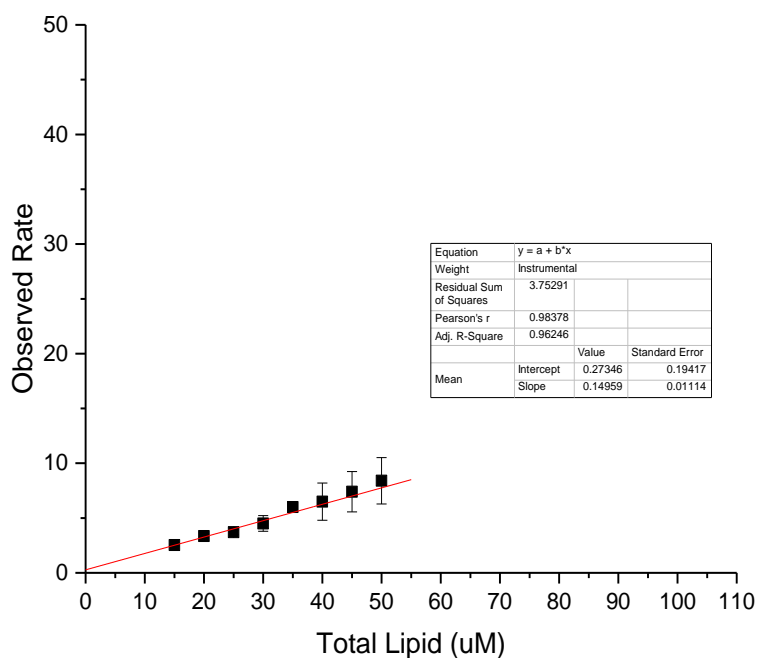
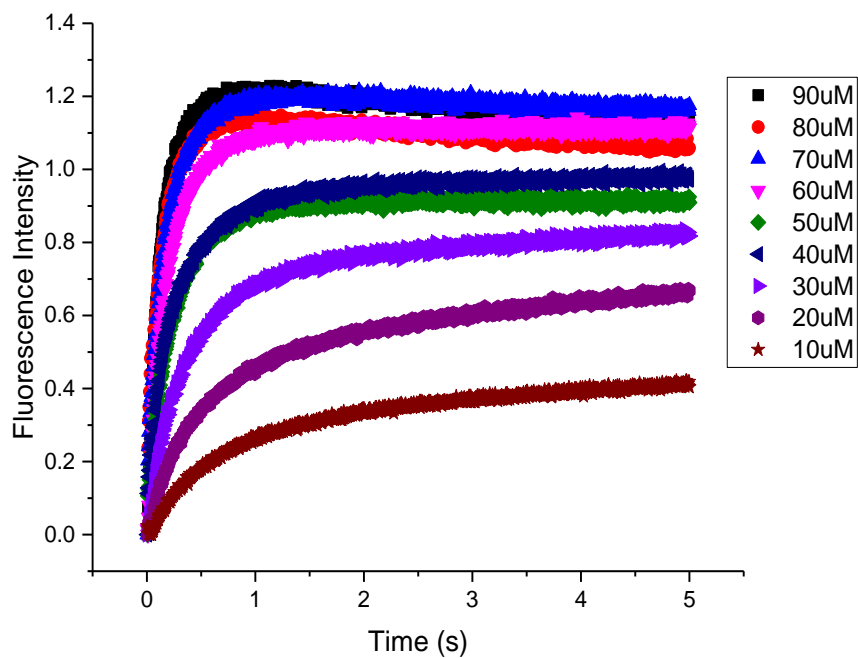
1%PI(4,5)P₂ 10%PS stopped-flow raw data. Top graph is the analytical graph used to determine on and off rates of PTEN binding to mixed vesicles. Bottom graph is an example of the raw data used in the graph above and the global fit.



1%PI(4,5)P₂ 10%PI stopped-flow raw data. Top graph is the analytical graph used to determine on and off rates of PTEN binding to mixed vesicles. Bottom graph is an example of the raw data used in the graph above and the global fit.

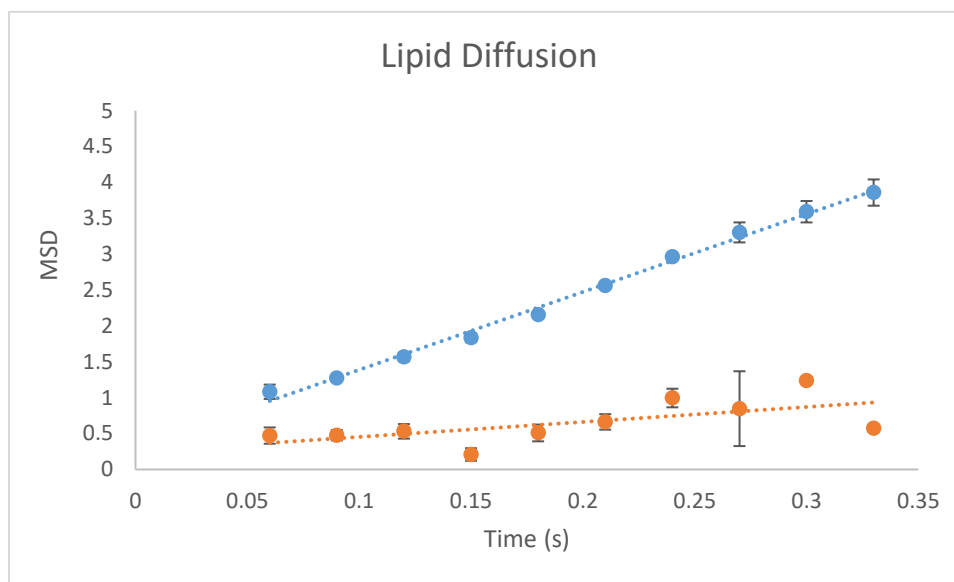


5%PI(4,5)P₂ 30%PS stopped-flow raw data. Top graph is the analytical graph used to determine on and off rates of PTEN binding to mixed vesicles. Bottom graph is an example of the raw data used in the graph above and the global fit.

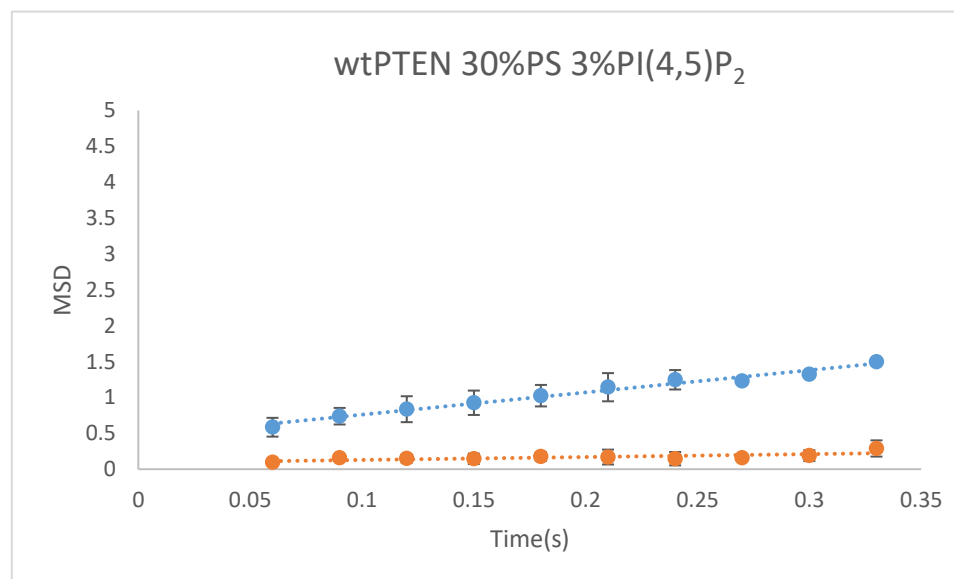


5%PI(4,5)P₂ 30%PS stopped-flow raw data. Top graph is the analytical graph used to determine on and off rates of PTEN binding to mixed vesicles. Bottom graph is an example of the raw data used in the graph above and the global fit.

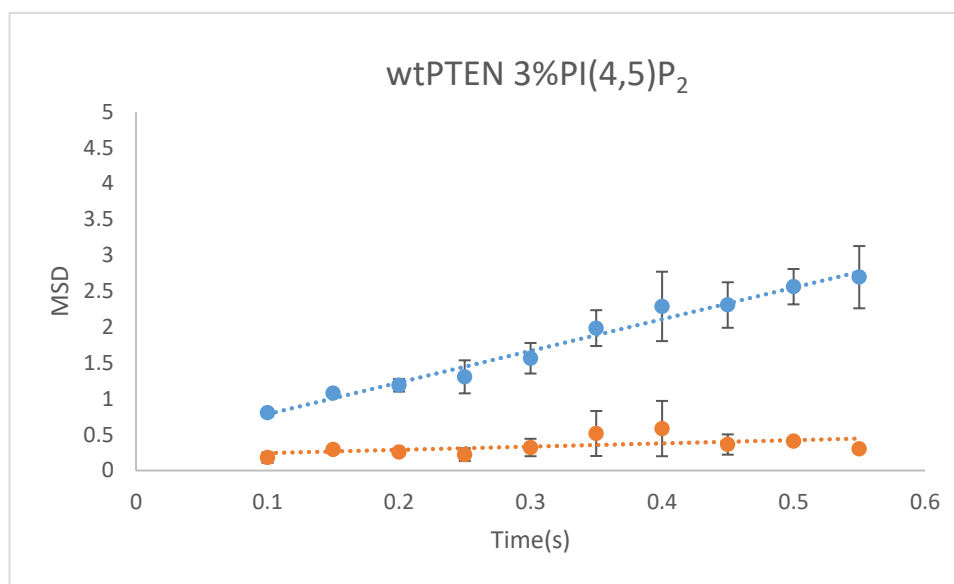
Single-Molecule



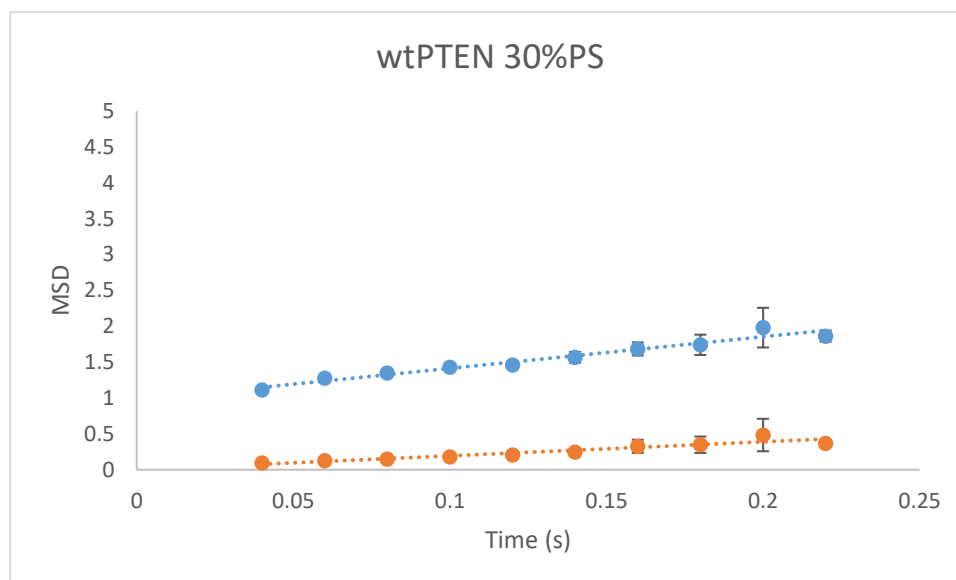
Single-molecule velocity graphs of lipid diffusion. The data is at least 2N for the matching exposure times. From these data the diffusion coefficient is determined from the line.



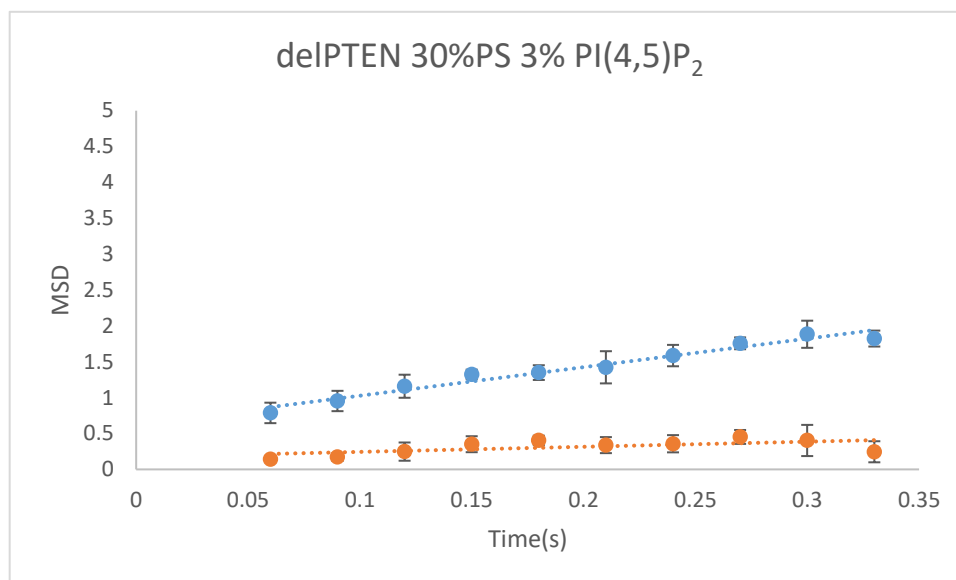
Single-molecule velocity graphs of wtPTEN on 30%PS 3%PI(4,5)P₂ SLB. The data is at least 2N for the matching exposure times. From these data the diffusion coefficient is determined from the line.



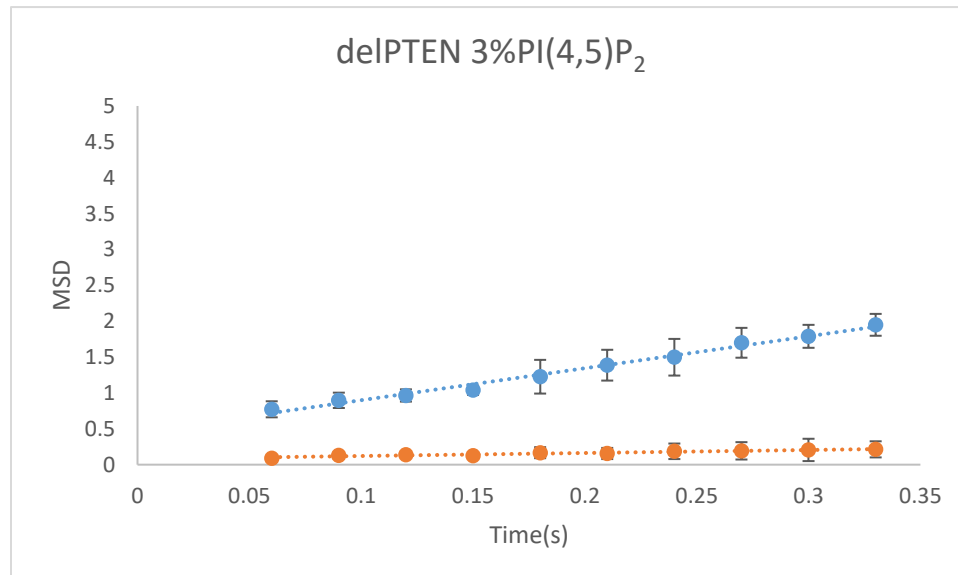
Single-molecule velocity graphs of wtPTEN on 3%PI(4,5)P₂ SLB. The data is at least 2N for the matching exposure times. From these data the diffusion coefficient is determined from the line.



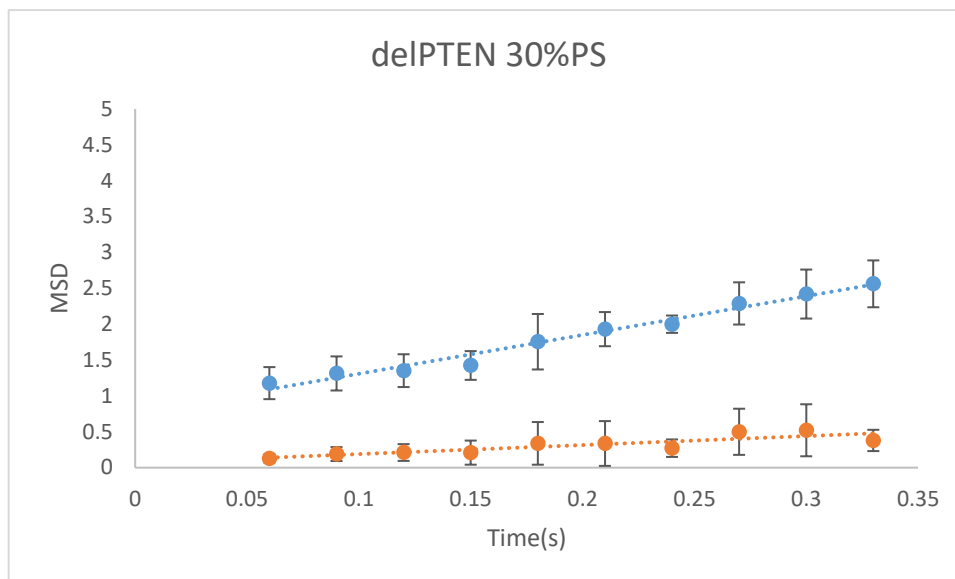
Single-molecule velocity graphs of wtPTEN on 30% PS SLB. The data is at least 2N for the matching exposure times. From these data the diffusion coefficient is determined from the line.



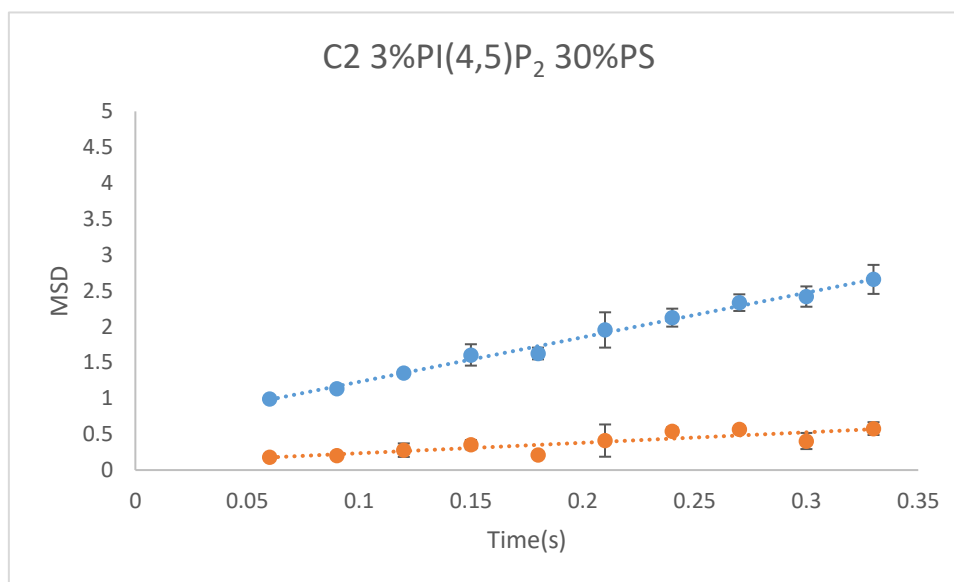
Single-molecule velocity graphs of delIPTEN on 30% PS 3%PI(4,5)P₂ SLB. The data is at least 2N for the matching exposure times. From these data the diffusion coefficient is determined from the line.



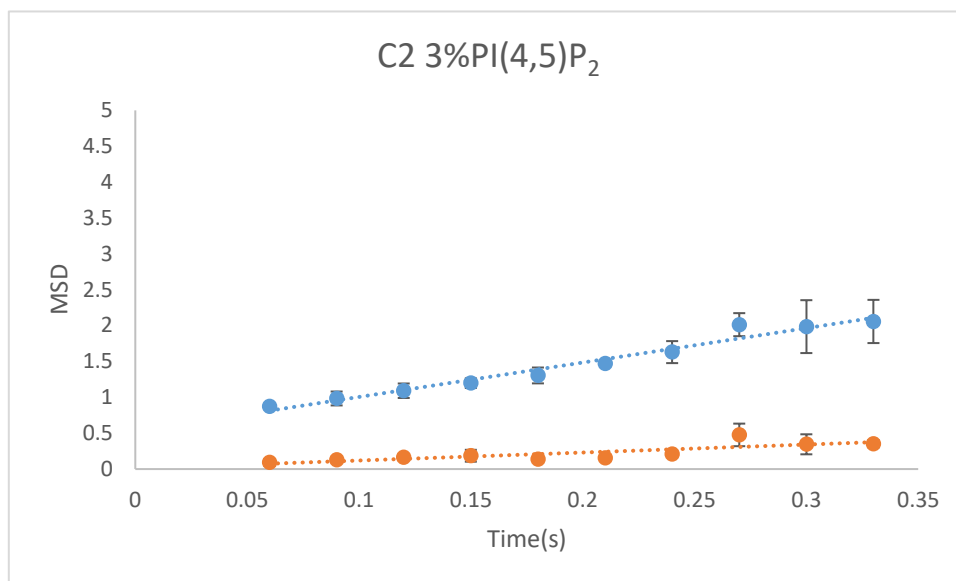
Single-molecule velocity graphs of delIPTEN on 3%PI(4,5)P₂ SLB. The data is at least 2N for the matching exposure times. From these data the diffusion coefficient is determined from the line.



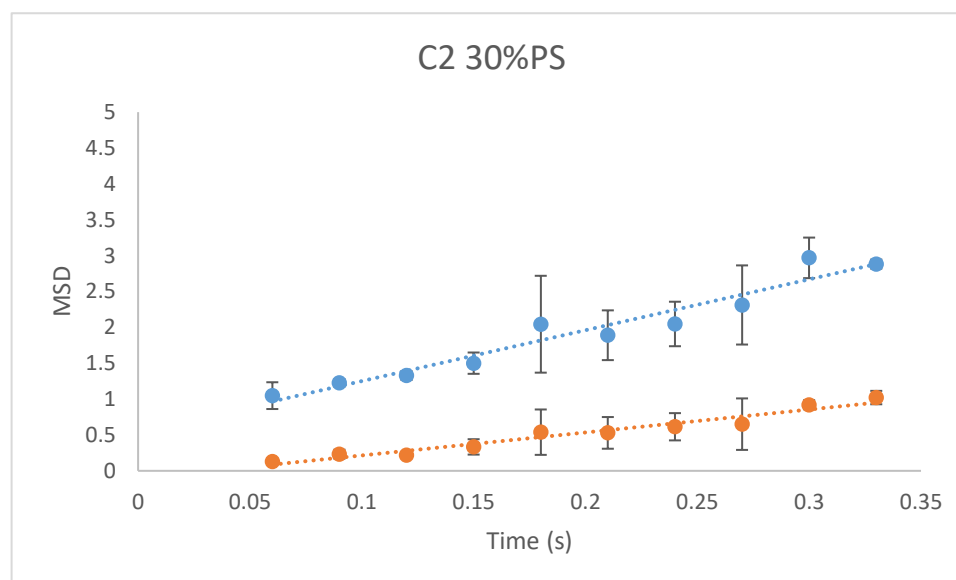
Single-molecule velocity graphs of delIPTEN on 30% PS SLB. The data is at least 2N for the matching exposure times. From these data the diffusion coefficient is determined from the line.



Single-molecule velocity graphs of C2 on 30% PS 3%PI(4,5)P₂ SLB. The data is at least 2N for the matching exposure times. From these data the diffusion coefficient is determined from the line.



Single-molecule velocity graphs of C2 on 3%PI(4,5)P₂ SLB. The data is at least 2N for the matching exposure times. From these data the diffusion coefficient is determined from the line.



Single-molecule velocity graphs of C2 on 30% PS SLB. The data is at least 2N for the matching exposure times. From these data the diffusion coefficient is determined from the line.

Bibliography

- [1] Singer, S. J., and Nicolson, G. L. (1972) The Fluid Mosaic Model of the Structure of Cell Membranes, *Science* 175, 720-731.
- [2] Goñi, F. M. (2014) The basic structure and dynamics of cell membranes: An update of the Singer–Nicolson model, *Biochimica et Biophysica Acta (BBA) - Biomembranes* 1838, 1467-1476.
- [3] Sud M., F. E., Cotter D., Brown A., Dennis E., Glass C., Murohy R., Raetz C., Russell D., and Subramaniam S. (2006) LMSD: LIPID MAPS structure database, *Nucleic Acids Research* 35, D527-532.
- [4] van Meer, G., Voelker, D. R., and Feigenson, G. W. (2008) Membrane lipids: where they are and how they behave, *Nature Reviews Molecular Cell Biology* 9, 112-124.
- [5] Coskun, Ü., and Simons, K. (2011) Cell Membranes: The Lipid Perspective, *Structure* 19, 1543-1548.
- [6] Luckey, M. (2014) *Membrane Structural Biology*, 2 ed., Cambridge University Press, University Printing House, Cambridge, United Kingdom.
- [7] Stahelin, R. V., Scott, J. L., and Frick, C. T. (2014) Cellular and molecular interactions of phosphoinositides and peripheral proteins, *Chemistry and Physics of Lipids* 182, 3-18.
- [8] Harishchandra, R. K., Neumann, B. M., Gericke, A., and Ross, A. H. (2015) Biophysical methods for the characterization of PTEN/lipid bilayer interactions, *Methods* 77-78, 125-135.

- [9] Jiang, Z. P., Redfern, R. E., Isler, Y., Ross, A. H., and Gericke, A. (2014) Cholesterol stabilizes fluid phosphoinositide domains, *Chemistry and Physics of Lipids* 182, 52-61.
- [10] Lemmon, M. A. (2008) Membrane recognition by phospholipid-binding domains, *Nature Reviews Molecular Cell Biology* 9, 99-111.
- [11] Gericke, A., Munson, M., and Ross, A. H. (2006) Regulation of the PTEN phosphatase, *Gene* 374, 1-9.
- [12] Letunic, I., and Bork, P. (2017) 20 years of the SMART protein domain annotation resource, *Nucleic Acids Res.*
- [13] Cantley, L. C., and Neel, B. G. (1999) New insights into tumor suppression: PTEN suppresses tumor formation by restraining the phosphoinositide 3-kinase AKT pathway, *Proc. Natl. Acad. Sci. U. S. A.* 96, 4240-4245.
- [14] Li, J., Yen, C., Liaw, D., Podsypanina, K., Bose, S., Wang, S. I., Puc, J., Miliareis, C., Rodgers, L., McCombie, R., Bigner, S. H., Giovanella, B. C., Ittmann, M., Tycko, B., Hibshoosh, H., Wigler, M. H., and Parsons, R. (1997) PTEN, a putative protein tyrosine phosphatase gene mutated in human brain, breast, and prostate cancer, *Science* 275, 1943-1947.
- [15] Maehama, T., and Dixon, J. E. (1999) PTEN: a tumour suppressor that functions as a phospholipid phosphatase, *Trends in Cell Biology* 9, 125-128.
- [16] Li, D. M., and Sun, H. (1997) TEP1, encoded by a candidate tumor suppressor locus, is a novel protein tyrosine phosphatase regulated by transforming growth factor beta, *Cancer Res.* 57, 2124-2129.

- [17] Risinger, J. I., Hayes, A. K., Berchuck, A., and Barrett, J. C. (1997) PTEN/MMAC1 mutations in endometrial cancers, *Cancer Res.* 57, 4736-4738.
- [18] Gustin, J. A., Maehama, T., Dixon, J. E., and Donner, D. B. (2001) The PTEN tumor suppressor protein inhibits tumor necrosis factor-induced nuclear factor kappa B activity, *Journal of Biological Chemistry* 276, 27740-27744.
- [19] Maehama, T., Taylor, G. S., and Dixon, J. E. (2001) PTEN and myotubularin: Novel phosphoinositide phosphatases, *Annual Review of Biochemistry* 70, 247-279.
- [20] Cairns, P., Evron, E., Okami, K., Halachmi, N., Esteller, M., Herman, J. G., Bose, S., Wang, S. I., Parsons, R., and Sidransky, D. (1998) Point mutation and homozygous deletion of PTEN/MMAC1 in primary bladder cancers, *Oncogene* 16, 3215-3218.
- [21] Duerr, E. M., Rollbrocker, B., Hayashi, Y., Peters, N., Meyer-Puttlitz, B., Louis, D. N., Schramm, J., Wiestler, O. D., Parsons, R., Eng, C., and von Deimling, A. (1998) PTEN mutations in gliomas and glioneuronal tumors, *Oncogene* 16, 2259-2264.
- [22] Li, D. M., and Sun, H. (1998) PTEN/MMAC1/TEP1 suppresses the tumorigenicity and induces G(1) cell cycle arrest in human glioblastoma cells, *Proceedings of the National Academy of Sciences of the United States of America* 95, 15406-15411.
- [23] Chalhoub, N., and Baker, S. J. (2009) PTEN and the PI3-Kinase Pathway in Cancer, *Annual review of pathology* 4, 127-150.
- [24] Liaw, D., Marsh, D. J., Li, J., Dahia, P. L. M., Wang, S. I., Zheng, Z. M., Bose, S., Call, K. M., Tsou, H. C., Peacocke, M., Eng, C., and Parsons, R. (1997) Germline

mutations of the PTEN gene in Cowden disease, an inherited breast and thyroid cancer syndrome, *Nature Genetics* 16, 64-67.

- [25] Nelen, M. R., vanStaveren, W. C. G., Peeters, E. A. J., BenHassel, M., Gorlin, R. J., Hamm, H., Lindboe, C. F., Fryns, J. P., Sijmons, R. H., Woods, D. G., Mariman, E. C. M., Padberg, G. W., and Kremer, H. (1997) Germline mutations in the PTEN/MMAC1 gene in patients with Cowden disease, *Human Molecular Genetics* 6, 1383-1387.
- [26] Marsh, D. J., Coulon, V., Lunetta, K. L., Rocca-Serra, P., Dahia, P. L. M., Zheng, Z. M., Liaw, D., Caron, S., Duboue, B., Lin, A. Y., Richardson, A. L., Bonnetblanc, J. M., Bressieux, J. M., Cabarrot-Moreau, A., Chompret, A., Demange, L., Eeles, R. A., Yahanda, A. M., Fearon, E. R., Fricker, J. P., Gorlin, R. J., Hodgson, S. V., Huson, S., Lacombe, D., LePrat, F., Odent, S., Toulouse, C., Olopade, O. I., Sobol, H., Tishler, S., Woods, C. G., Robinson, B. G., Weber, H. C., Parsons, R., Peacocke, M., Longy, M., and Eng, C. (1998) Mutation spectrum and genotype-phenotype analyses in Cowden disease and Bannayan-Zonana syndrome, two hamartoma syndromes with germline PTEN mutation, *Human Molecular Genetics* 7, 507-515.
- [27] Leslie, N. R., and Longy, M. (2016) Inherited PTEN mutations and the prediction of phenotype, *Seminars in Cell & Developmental Biology* 52, 30-38.
- [28] Suzuki, A., de la Pompa, J. L., Stambolic, V., Elia, A. J., Sasaki, T., Barrantes, I. D., Ho, A., Wakeham, A., Itie, A., Khoo, W., Fukumoto, M., and Mak, T. W. (1998) High cancer susceptibility and embryonic lethality associated with mutation of the PTEN tumor suppressor gene in mice, *Current Biology* 8, 1169-1178.

- [29] Cairns, P., Okami, K., Halachmi, S., Halachmi, N., Esteller, M., Herman, J. G., Isaacs, W. B., Bova, G. S., and Sidransky, D. (1997) Frequent inactivation of PTEN/MMAC1 in primary prostate cancer, *Cancer Res.* 57, 4997-5000.
- [30] Maehama, T., and Dixon, J. E. (1998) The tumor suppressor, PTEN/MMAC1, dephosphorylates the lipid second messenger, phosphatidylinositol 3,4,5-trisphosphate, *Journal of Biological Chemistry* 273, 13375-13378.
- [31] Hou, S. Q., Ouyang, M., Brandmaier, A., Hao, H. B., and Shen, W. H. (2017) PTEN in the maintenance of genome integrity: From DNA replication to chromosome segregation, *Bioessays* 39, 9.
- [32] Stambolic, V., Suzuki, A., de la Pompa, J. L., Brothers, G. M., Mirtsos, C., Sasaki, T., Ruland, J., Penninger, J. M., Siderovski, D. P., and Mak, T. W. (1998) Negative regulation of PKB/Akt-dependent cell survival by the tumor suppressor PTEN, *Cell* 95, 29-39.
- [33] Carnero, A., and Paramio, J. M. (2014) The PTEN/PI3K/AKT Pathway in vivo, Cancer Mouse Models, *Frontiers in Oncology* 4.
- [34] Lee, J. O., Yang, H. J., Georgescu, M. M., Di Cristofano, A., Maehama, T., Shi, Y. G., Dixon, J. E., Pandolfi, P., and Pavletich, N. P. (1999) Crystal structure of the PTEN tumor suppressor: Implications for its phosphoinositide phosphatase activity and membrane association, *Cell* 99, 323-334.
- [35] Furnari, F. B., Lin, H., Huang, H. J. S., and Cavenee, W. K. (1997) Growth suppression of glioma cells by PTEN requires a functional phosphatase catalytic domain, *Proceedings of the National Academy of Sciences of the United States of America* 94, 12479-12484.

- [36] Redfern, R. E., Redfern, D., Furgason, M. L. M., Munson, M., Ross, A. H., and Gericke, A. (2008) PTEN phosphatase selectively binds phosphoinositides and undergoes structural changes, *Biochemistry* 47, 2162-2171.
- [37] Campbell, R. B., Liu, F. H., and Ross, A. H. (2003) Allosteric activation of PTEN phosphatase by phosphatidylinositol 4,5-bisphosphate, *Journal of Biological Chemistry* 278, 33617-33620.
- [38] Matsuoka, S., Ueda, M., Kuwayama, H., Devreotes, P., and Yanagida, T. (2004) Phosphatase activity of PTEN enhanced by PI(4,5)P-2-binding, *Cell Structure and Function* 29, 60-60.
- [39] He, H., Watanabe, T., Zhan, X., Huang, C., Schuurin, E., Fukami, K., Takenawa, T., Kumar, C. C., Simpson, R. J., and Maruta, H. (1998) Role of phosphatidylinositol 4,5-bisphosphate in Ras/Rac-induced disruption of the cortactin-actomyosin II complex and malignant transformation, *Molecular and Cellular Biology* 18, 3829-3837.
- [40] Janmey, P. A., Lamb, J., Allen, P. G., and Matsudaira, P. T. (1992) Phosphoinositide binding peptides derived from the sequences of gelsolin and villin, *Journal of Biological Chemistry* 267, 11818-11823.
- [41] Yu, F. X., Sun, H. Q., Janmey, P. A., and Yin, H. L. (1992) Identification of a polyphosphoinositide binding sequence in an actin monomer binding domain of gelsolin, *Journal of Biological Chemistry* 267, 14616-14621.
- [42] Yu, F. X., Sun, H. Q., Janmey, P. A., and Yin, H. L. (1992) IDENTIFICATION OF A POLYPHOSPHOINOSITIDE-BINDING SEQUENCE IN AN ACTIN MONOMER-

- BINDING DOMAIN OF GELSOLIN, *Journal of Biological Chemistry* 267, 14616-14621.
- [43] Stock, A., Steinmetz, M. O., Janmey, P. A., Aebi, U., Gerisch, G., Kammerer, R. A., Weber, I., and Faix, J. (1999) Domain analysis of cortexillin I: actin-bundling, PIP2-binding and the rescue of cytokinesis, *Embo Journal* 18, 5274-5284.
- [44] Ross, A. H., and Gericke, A. (2009) Phosphorylation keeps PTEN phosphatase closed for business, *Proc. Natl. Acad. Sci. U. S. A.* 106, 1297-1298.
- [45] Chen, T., and Warner (1956) *Anal. Chem.*, 1756-1758.
- [46] Subbarow, F. (1925) *J. Biol. Chem.*, 374-389.
- [47] Johnson, K. A., Simpson, Z. B., and Blom, T. (2009) Global Kinetic Explorer: A new computer program for dynamic simulation and fitting of kinetic data, *Analytical Biochemistry* 387, 20-29.
- [48] Lakowicz, J. R. (2006) *Principles of Fluorescence Spectroscopy*, 3rd ed., Springer.
- [49] Claessens, M. M. A. E., van Oort, B. F., Leermakers, F. A. M., Hoekstra, F. A., and Cohen Stuart, M. A. (2004) Charged Lipid Vesicles: Effects of Salts on Bending Rigidity, Stability, and Size, *Biophysical Journal* 87, 3882-3893.
- [50] Goodrich, J. A., and Kugel, J. F. (2007) *Binding and Kinetics for Molecular Biologists*, John Inglis, Cold Spring Harbor, New York.
- [51] Nalefski, E. A., Slazas, M. M., and Falke, J. J. (1997) Ca²⁺-Signaling Cycle of a Membrane-Docking C2 Domain†, *Biochemistry* 36, 12011-12018.
- [52] McKenna, J. M., and Ostap, E. M. (2009) Kinetics of the interaction of myo1c with phosphoinositides, *J Biol Chem* 284, 28650-28659.

- [53] Redfern, R. E., Daou, M. C., Li, L., Munson, M., Gericke, A., and Ross, A. H. (2010) A mutant form of PTEN linked to autism, *Protein Science* 19, 1948-1956.
- [54] Shenoy, S., Gericke, A., Ross, A., and Losche, M. (2011) Binding Affinities of WT and H93R PTEN to Lipid Membranes Containing PS and PI(4,5)P-2, *Biophysical Journal* 100, 525-525.
- [55] Shenoy, S., Shekhar, P., Heinrich, F., Daou, M. C., Gericke, A., Ross, A. H., and Losche, M. (2012) Membrane Association of the PTEN Tumor Suppressor: Molecular Details of the Protein-Membrane Complex from SPR Binding Studies and Neutron Reflection, *PLoS One* 7.
- [56] Heimburg, T., and Marsh, D. (1995) Protein surface-distribution and protein-protein interactions in the binding of peripheral proteins to charged lipid membranes, *Biophysical Journal* 68, 536-546.
- [57] McLaughlin, S., and Murray, D. (2005) Plasma membrane phosphoinositide organization by protein electrostatics, *Nature* 438, 605-611.
- [58] Marsh, D. (2008) Protein modulation of lipids, and vice-versa, in membranes, *Biochimica et Biophysica Acta - Biomembranes* 1778, 1545-1575.
- [59] Knight, J. D., Lerner, M. G., Marcano-Velázquez, J. G., Pastor, R. W., and Falke, Joseph J. (2010) Single Molecule Diffusion of Membrane-Bound Proteins: Window into Lipid Contacts and Bilayer Dynamics, *Biophysical Journal* 99, 2879-2887.
- [60] Knight, J. D., and Falke, J. J. (2009) Single-Molecule Fluorescence Studies of a PH Domain: New Insights into the Membrane Docking Reaction, *Biophysical Journal* 96, 566-582.

- [61] Paul R. Selvin, T. H. (2008) *Single-Molecule Techniques*, John Inglis, Cold Spring Harbor, New York.
- [62] Walter, N. G., Huang, C.-Y., Manzo, A. J., and Sobhy, M. A. (2008) Do-it-yourself guide: how to use the modern single-molecule toolkit, *Nature Methods* 5, 475.
- [63] Ho, B., Baryshnikova, A., and Brown, G. W. (2018) Unification of Protein Abundance Datasets Yields a Quantitative *Saccharomyces cerevisiae* Proteome, *Cell Syst* 6, 192-205 e193.
- [64] Ziemba, B. P., and Falke, J. J. (2013) Lateral diffusion of peripheral membrane proteins on supported lipid bilayers is controlled by the additive frictional drags of (1) bound lipids and (2) protein domains penetrating into the bilayer hydrocarbon core, *Chemistry and Physics of Lipids* 172, 67-77.
- [65] Yin, J., Lin, A. J., Golan, D. E., and Walsh, C. T. (2006) Site-specific protein labeling by Sfp phosphopantetheinyl transferase, *Nat Protoc* 1, 280-285.
- [66] Schindelin, J., Arganda-Carreras, I., Frise, E., Kaynig, V., Longair, M., Pietzsch, T., Preibisch, S., Rueden, C., Saalfeld, S., Schmid, B., Tinevez, J. Y., White, D. J., Hartenstein, V., Eliceiri, K., Tomancak, P., and Cardona, A. (2012) Fiji: an open-source platform for biological-image analysis, *Nat Methods* 9, 676-682.
- [67] Schindelin, J., Rueden, C. T., Hiner, M. C., and Eliceiri, K. W. (2015) The ImageJ ecosystem: An open platform for biomedical image analysis, *Molecular Reproduction and Development* 82, 518-529.
- [68] Schindelin, J., Arganda-Carreras, I., Frise, E., Kaynig, V., Longair, M., Pietzsch, T., Preibisch, S., Rueden, C., Saalfeld, S., Schmid, B., Tinevez, J.-Y., White, D. J.,

- Hartenstein, V., Eliceiri, K., Tomancak, P., and Cardona, A. (2012) Fiji: an open-source platform for biological-image analysis, *Nat Meth* 9, 676-682.
- [69] Sbalzarini, I. F., and Koumoutsakos, P. (2005) Feature point tracking and trajectory analysis for video imaging in cell biology, *J. Struct. Biol.* 151, 182-195.
- [70] Schütz, G. J., Schindler, H., and Schmidt, T. (1997) Single-molecule microscopy on model membranes reveals anomalous diffusion, *Biophysical Journal* 73, 1073-1080.
- [71] Vazquez, F., Matsuoka, S., Sellers, W. R., Yanagida, T., Ueda, M., and Devreotes, P. N. (2006) Tumor suppressor PTEN acts through dynamic interaction with the plasma membrane, *Proc. Natl. Acad. Sci. U. S. A.* 103, 3633-3638.
- [72] Yasui, M., Matsuoka, S., and Ueda, M. (2014) PTEN Hopping on the Cell Membrane Is Regulated via a Positively-Charged C2 Domain, *PLOS Computational Biology* 10, e1003817.
- [73] Qiu, Y., and Myong, S. (2016) Chapter Two - Single-Molecule Imaging With One Color Fluorescence, In *Methods in Enzymology* (Spies, M., and Chemla, Y. R., Eds.), pp 33-51, Academic Press.
- [74] Gassama-Diagne, A., and Payrastre, B. (2009) Phosphoinositide Signaling Pathways: Promising Role as Builders of Epithelial Cell Polarity, In *International Review of Cell and Molecular Biology*, Vol 273 (Jeon, K. W., Ed.), pp 313-343.
- [75] Echard, A. (2008) Membrane traffic and polarization of lipid domains during cytokinesis, *Biochemical Society Transactions* 36, 395-399.

- [76] Saarikangas, J., Zhao, H., and Lappalainen, P. (2010) Regulation of the Actin Cytoskeleton-Plasma Membrane Interplay by Phosphoinositides, *Physiological Reviews* 90, 259-289.
- [77] Viaud, J., Mansour, R., Antkowiak, A., Mujalli, A., Valet, C., Chicanne, G., Xuereb, J.-M., Terrisse, A.-D., Séverin, S., Gratacap, M.-P., Gaits-Iacovoni, F., and Payrastre, B. (2016) Phosphoinositides: Important lipids in the coordination of cell dynamics, *Biochimie* 125, 250-258.
- [78] Cauvin, C., and Echard, A. (2015) Phosphoinositides: Lipids with informative heads and mastermind functions in cell division, *Biochimica et Biophysica Acta (BBA) - Molecular and Cell Biology of Lipids* 1851, 832-843.
- [79] Tsujita, K., and Itoh, T. (2015) Phosphoinositides in the regulation of actin cortex and cell migration, *Biochimica et biophysica acta* 1851, 824-831.
- [80] Devreotes, P., and Horwitz, A. R. (2015) Signaling Networks that Regulate Cell Migration, *Cold Spring Harbor perspectives in biology* 7.
- [81] Krahn, M. P., and Wodarz, A. (2012) Phosphoinositide lipids and cell polarity: linking the plasma membrane to the cytocortex, *Essays in biochemistry* 53, 15-27.
- [82] De Craene, J. O., Bertazzi, D. L., Bar, S., and Friant, S. (2017) Phosphoinositides, Major Actors in Membrane Trafficking and Lipid Signaling Pathways, *International journal of molecular sciences* 18.
- [83] Kalb, E., Frey, S., and Tamm, L. K. (1992) Formation of supported planar bilayers by fusion of vesicles to supported phospholipid monolayers, *Biochimica et biophysica acta* 1103, 307-316.

- [84] Castellana, E. T., and Cremer, P. S. (2006) Solid supported lipid bilayers: From biophysical studies to sensor design, *Surface Science Reports* 61, 429-444.
- [85] Hardy, G. J., Nayak, R., and Zauscher, S. (2013) Model cell membranes: Techniques to form complex biomimetic supported lipid bilayers via vesicle fusion, *Current Opinion in Colloid & Interface Science* 18, 448-458.
- [86] Shekhar, P., Nanda, H., Losche, M., and Heinrich, F. (2011) Continuous distribution model for the investigation of complex molecular architectures near interfaces with scattering techniques, *Journal of Applied Physics* 110, 12.
- [87] Liu, K. N., Hung, C. M. S., Swift, M. A., Munoz, K. A., Cortez, J. L., and Sanii, B. (2015) Configurable lipid membrane gradients quantify diffusion, phase separations and binding densities, *Soft Matter* 11, 8217-8220.
- [88] Krabbenborg, S. O., van Weerd, J., Karperien, M., Jonkheijm, P., and Huskens, J. (2014) Locked-in Biomimetic Surface Gradients that are Tunable in Size, Density and Functionalization, *Chemphyschem* 15, 3460-3465.
- [89] Byfield, F. J., Wen, Q., Levental, I., Nordstrom, K., Arratia, P. E., Miller, R. T., and Janmey, P. A. (2009) Absence of filamin A prevents cells from responding to stiffness gradients on gels coated with collagen but not fibronectin, *Biophys J* 96, 5095-5102.
- [90] Dertinger, S. K. W., Chiu, D. T., Jeon, N. L., and Whitesides, G. M. (2001) Generation of gradients having complex shapes using microfluidic networks, *Analytical Chemistry* 73, 1240-1246.

- [91] Jeon, N. L., Dertinger, S. K. W., Chiu, D. T., Choi, I. S., Stroock, A. D., and Whitesides, G. M. (2000) Generation of solution and surface gradients using microfluidic systems, *Langmuir* 16, 8311-8316.
- [92] Toh, A. G. G., Wang, Z. P., Yang, C., and Nguyen, N. T. (2014) Engineering microfluidic concentration gradient generators for biological applications, *Microfluid. Nanofluid.* 16, 1-18.
- [93] Sackmann, E. K., Fulton, A. L., and Beebe, D. J. (2014) The present and future role of microfluidics in biomedical research, *Nature* 507, 181-189.
- [94] Moens, P. D., Bagatolli, L.A. (2007) Profilin Binding to Sub-micellar Concentrations of Phosphatidylinositol(4,5)bisphosphate and Phosphatidylinositol (3,4,5) trisphosphate, *Biochim. Biophys. Acta* 1768, 439-449.
- [95] Slochower, D. R., Wang, Y. H., Tourdot, R. W., Radhakrishnan, R., and Janmey, P. A. (2014) Counterion-mediated pattern formation in membranes containing anionic lipids, *Advances in Colloid and Interface Science* 208, 177-188.
- [96] Vernier, P. T., Ziegler, M. J., and Dimova, R. (2009) Calcium Binding and Head Group Dipole Angle in Phosphatidylserine-Phosphatidylcholine Bilayers, *Langmuir* 25, 1020-1027.
- [97] Sinn, C. G., Antonietti, M., and Dimova, R. (2006) Binding of calcium to phosphatidylcholine-phosphatidylserine membranes, *Colloids and Surfaces a- Physicochemical and Engineering Aspects* 282, 410-419.
- [98] Roux, M., and Bloom, M. (1991) Calcium-binding by phosphatidylserine headgroups - deuterium NMR study, *Biophysical Journal* 60, 38-44.

- [99] Feigenson, G. W. (1989) Calcium-ion binding between lipid bilayers. The 4-component system of phosphatidylserine, phosphatidylcholine, calcium chloride, and water, *Biochemistry* 28, 1270-1278.
- [100] Florine, K. I., and Feigenson, G. W. (1987) Influence of the calcium-induced gel phase on the behavior of small molecules in phosphatidylserine and phosphatidylserine phosphatidylcholine multilamellar vesicles, *Biochemistry* 26, 1757-1768.
- [101] Feigenson, G. W. (1986) On the nature of calcium-ion binding between phosphatidylserine lamellae, *Biochemistry* 25, 5819-5825.
- [102] Marsh, D. (2013) Handbook of Lipid Bilayers 2nd edition.
- [103] Luna, C., Stroka, K. M., Bermudez, H., and Aranda-Espinoza, H. (2011) Thermodynamics of monolayers formed by mixtures of phosphatidylcholine/phosphatidylserine, *Colloids and Surfaces B-Biointerfaces* 85, 293-300.
- [104] Hauser, H., Chapman, D., Dawson, R.M. (1969) Physical Studies of Phospholipids. XI. Ca²⁺ Binding to Monolayers of Phosphatidylserine and Phosphatidylinositol, *Biochim. Biophys. Acta* 183, 320-333.
- [105] Wang, Y. H., Slochower, D. R., and Janmey, P. A. (2014) Counterion-mediated cluster formation by polyphosphoinositides, *Chemistry and Physics of Lipids* 182, 38-51.
- [106] Braunger, J. A., Kramer, C., Morick, D., and Steinem, C. (2013) Solid Supported Membranes Doped with PIP: Influence of Ionic Strength and pH on Bilayer Formation and Membrane Organization, *Langmuir*.

- [107] Wang, Y. H., Bucki, R., and Janmey, P. A. (2016) Cholesterol-Dependent Phase-Demixing in Lipid Bilayers as a Switch for the Activity of the Phosphoinositide-Binding Cytoskeletal Protein Gelsolin, *Biochemistry* 55, 3361-3369.
- [108] Taglieri, D. M., Delfín, D. A., and Monasky, M. M. (2012) Cholesterol regulation of PIP(2): why cell type is so important, *Frontiers in Physiology* 3, 492.
- [109] Ilya, L., Christian, D. A., Wang, Y.-H., Madara, J. J., Discher, D. E., and Janmey, P. A. (2009) Calcium-dependent lateral organization in phosphatidylinositol (4,5) bisphosphate (PIP₂)- and cholesterol-containing monolayers, *Biochemistry* 48, 8241-8248.
- [110] Jonsson, P., Beech, J. P., Tegenfeldt, J. O., and Hook, F. (2009) Shear-Driven Motion of Supported Lipid Bilayers in Microfluidic Channels, *J. Am. Chem. Soc.* 131, 5294-5297.